



UNIVERSITÀ DEGLI STUDI DI MILANO
DIPARTIMENTO DI FISICA
DOTTORATO DI RICERCA IN FISICA – XI CICLO

Data taking and analysis
of
the Counting Test Facility of Borexino

Tesi di Dottorato di
Cristiano Galbiati

Tutore :
Ch.^{mo} Prof. Gianpaolo Bellini

Coordinatore dottorato:
Ch.^{mo} Prof. Antonio Pullia

Anno accademico 1997/98

Contents

Contents	ii
List of Figures	iv
List of Tables	vii
Introduction	1
I So tiny and vanishing	2
I-A Open questions on neutrinos	2
I-B Neutrino oscillation experiments	2
I-C Solar neutrinos	5
I-C.1 The experiments on solar neutrinos	6
I-C.2 The solar neutrino problem	10
II Borexino . . .	18
II-A An overview of the BX design: the clue idea and the basic concepts	18
II-B The structure of the detector	20
II-B.1 The outer water tank.	21
II-B.2 The Water Buffer.	22
II-B.3 The Water Purification Plant	22
II-B.4 The Stainless Steel Sphere	22
II-B.5 The Buffer Liquid	23
II-B.6 The nylon scintillator vessel or Inner Vessel	23
II-B.7 The Scintillator	23
II-B.8 The Scintillator Purification System	24
II-B.9 The detection of light	26
II-B.10 The electronics and the data acquisition	27
II-C The performance of BX	27
II-C.1 The signal	27
II-C.2 The background	28
II-C.3 The Muon Detector	33
II-D The Physics potential of BX	37
III . . . and its Counting Test Facility	41
III-A The CTF project	41
III-B The structure of the CTF detector	42
III-B.1 The water tank	44
III-B.2 The Water Buffer	44
III-B.3 The Open Structure	44
III-B.4 The nylon scintillator vessel or Inner Vessel	44
III-B.5 The Scintillator	44
III-B.6 The Scintillator Purification System	44
III-B.7 The detection of light	45
III-B.8 The electronics and the data acquisition	45
III-C The CTF data taking	46
III-DA detailed review of the data acquisition phases	46
III-EA review of the data acquisition phases relevant for the discussion of the data analysis	48

IV Measurements performed using the delayed coincidence method	50
IV-A The initial ^{222}Rn contamination: a powerful monitoring tool	50
IV-A.1 The Munich measurement on α quenching	51
IV-A.2 The energy calibration	51
IV-B The ^{232}Th contamination	52
IV-B.1 The sensitivity	52
IV-B.2 The toron	54
IV-B.3 The Maximum Likelihood method	58
IV-B.4 The measurements	60
IV-C The ^{238}U contamination	68
IV-C.1 The sensitivity	68
IV-C.2 Background from ^{222}Rn	71
IV-C.3 The measurement of ^{238}U contamination	76
IV-D The ^{85}Kr contamination	81
IV-D.1 The sensitivity	81
IV-D.2 The measurement	82
IV-E The neutrons produced by cosmic rays	82
V Measurements performed without using the delayed coincidences method	94
V-A α/β discrimination	94
V-B Discrimination of the Čerenkov from the scintillation events	96
V-C Spatial reconstruction	96
V-D Decay mechanism of the scintillator and light propagation	100
V-E ^{14}C contamination	100
V-F The results of the NAA measurements	102
V-G The total counting rate	104
V-G.1 The sources	104
VI Conclusions	112
VI-A ^{14}C contamination	112
VI-B Natural radioactive chains contamination	113
VI-C Gaseous fall-out products contamination	114
VI-D Total counting rate	114
Bibliography	114

List of Figures

I.1	Prediction of the Bahcall, Basu and Pinsonneault 98 SSM [BBP98]: sound speed in the sun. This figure shows the excellent agreement between the calculated and the measured sound speeds, a fractional difference of 10^{-3} rms for all speeds measured between 0.05 and 0.95 of the solar radius. The vertical scale is chosen so as to emphasize that the fractional error is much smaller than generic changes in the model, from 0.03 to 0.08, that might significantly affect the solar neutrino prediction.	8
I.2	Prediction of the Bahcall-Basu-Pinsonneault 98 SSM [BBP98]: solar neutrinos spectrum. . .	10
I.3	Comparison of the results from experiments on solar neutrinos with the predictions of the Bahcall, Basu and Pinsonneault 98 SSM.	11
I.4	Predictions of SSMs since 1991. The figure taken from ref. [BKS98] shows the predictions from 19 SSMs in the plane defined by the ^7Be and ^8B neutrino fluxes and normalized to the predictions of the Bahcall, Basu and Pinsonneault 98 SSM. The rectangular box defines the 3σ error range of the flux predicted by the Bahcall, Basu and Pinsonneault model. The best fit ^7Be neutrino flux is negative. At 99 % C.L. there is no solution for all positive neutrino fluxes. All of the SSMs solutions lie far from the best fit solution, event far from the 3σ contour.	13
I.5	From [BKS98], MSW solution.	14
I.6	From [BKS98], MSW oscillation into sterile neutrinos solution.	15
I.7	From [BKS98], vacuum oscillation solution: the parameter region consistent with the total rates measured in the four experiments and with the electron recoil spectrum and the day-night asymmetry measured in SuperKamiokaNDE. Contours are drawn at 99 % C.L..	16
I.8	From [BKS98], MSW LMA and LOW solutions: the parameter region consistent with the only total rates measured in the four experiments. Contours are drawn at 99 % C.L..	17
II.1	A schematic view of Borexino.	20
II.2	Time decay distribution of the scintillator for emission excited by α or β - γ radiation (from laboratory measurements, see reference [RGL98]).	25
II.3	Emission spectrum of the BX scintillator (from laboratory measurements, see reference [RGL98]).	25
II.4	Quantum efficiency of the PMTs.	26
II.5	The expected rates in BX for several solution to the Solar Neutrino Problem in terms of neutrino oscillations.	28
II.6	Energy spectrum of external background. The spectrum is compared with the neutrino signal spectrum, in the case of the SSM and MSW scenarios.	29
II.7	Radial distribution of the external background events in the neutrino window. The distribution is compared with that of neutrino signal. Infinite spatial resolution is assumed.	30
II.8	Energy spectrum of the internal background. The spectrum is compared with the neutrino spectrum in the case of the flux predicted by the BBP 98 SSM.	34
II.9	Energy spectrum of the internal background. The spectrum is compared with the neutrino spectrum in the case of the flux predicted by the BBP 98 SSM in the energy region above the software energy threshold.	35
II.10	Expected variation of the ^7Be signal as a function of the absolute time difference from the perihelion.	38
II.11	Deviation from the no-oscillation values for the first three harmonics of the neutrino real time distribution in the experiments SNO, SuperKamiokande and BX.	39
II.12	Survival probability for MSW solutions.	40
III.1	A drawing of CTF.	42
III.2	A picture of the internal part of CTF, showing the Inner Vessel surrounded by PMTs. . . .	43

IV.1 Phase Foxtrot, Runs # 82–85 only. Energy spectrum of ^{214}Po candidates.	52
IV.2 Phase Golf. Delay time distribution for the sample of sequences selected by means of the Th cuts.	55
IV.3 Phase Golf. Energy distribution for the candidate ^{212}Po in the sample of sequences selected by means of the Th cuts.	56
IV.4 Phase Golf. Distribution of delay time versus energy for the candidate ^{212}Po for in the sample of sequences selected by means of the wider Th cuts.	57
IV.5 Phase Foxtrot. Real time distribution for the sample of sequences selected by means of the MI cuts.	61
IV.6 Phase Foxtrot. Energy distribution for candidates ^{212}Bi in the sample of sequences selected by means of the MI cuts.	62
IV.7 Phase Foxtrot. Energy distribution for candidates ^{212}Po in the sample of sequences selected by means of the MI cuts.	63
IV.8 Phase Foxtrot. Delay time distribution for the sample of sequences selected by means of the MI cuts.	64
IV.9 Phase Foxtrot. Distribution of delay time versus energy for the candidates ^{212}Po in the sample of sequences selected by means of the MI cuts.	65
IV.10Phase Lima. Distribution of delay time versus energy for the candidate ^{212}Po in the sample of sequences selected by means of the MI cuts.	66
IV.11Phase Oscar. Distribution of delay time versus energy for the candidates ^{212}Po in the sample of the sequences selected by means of the MI cuts.	69
IV.12Phase Quebec. Count rate in the external Rn window (1.5–2.7 MeV).	74
IV.13Phase Quebec. Count rate for mass 214 sequences selected by means of the U cuts.	75
IV.14Phase Foxtrot. Rate of mass 214 sequences selected by means of the U cuts. The rate is corrected for dead time in data acquisition.	77
IV.15The ^{232}Th radioactive chain.	78
IV.16The ^{235}U radioactive chain.	79
IV.17The ^{238}U radioactive chain.	80
IV.18Phase Foxtrot. Real time distribution for the sample of sequences selected by means of the Kr cuts.	83
IV.19Phase Foxtrot. Energy distribution for the candidate first events in the sample of the sequences selected by means of the Kr cuts.	84
IV.20Phase Foxtrot. Energy distribution for the candidate $^{85\text{m}}\text{Rb}$ in the sample of the sequences selected by means of the Kr cuts.	85
IV.21Phase Foxtrot. Delay time distribution for the sample of sequences selected by means of the Kr cuts.	86
IV.22Simulation. Expected energy spectrum for γ -rays from capture of neutrons thermalized in the scintillator.	89
IV.23Simulation. Expected energy spectrum for γ -rays from capture of neutrons thermalized in the water buffer.	90
IV.24160 d of data taking, from phase Lima to phase Oscar. Delay distribution for the sample of sequences selected by means of the neutron cuts.	91
IV.25160 d of data taking, from phase Lima to phase Oscar. Energy distribution for the candidate second events in the sample of sequences selected by means of the neutron cuts.	92
IV.26Simulation. Expected energy spectrum for γ -rays from capture of neutrons thermalized both in the scintillator and in the water buffer.	93
V.1 Phase Foxtrot. Distribution of the charge ratio R32 versus energy.	95
V.2 Phase Bravo. Spectrum of the Čerenkov radiation.	97
V.3 Phase Bravo. Photon arrival time distribution for the two components of Čerenkov radiation.	98
V.4 Phase Foxtrot. Photon arrival time distribution for the scintillation events.	99
V.5 Phase Rubatto. Comparison between the nominal positions of the ^{222}Rn source (empty circles) and the reconstructed positions (small crosses).	101
V.6 Phase Oscar. Energy spectrum of CTF in the energy interval below 350 KeV. The spectrum is fitted with the β spectrum of ^{14}C plus a slowly varying background to derive the ^{14}C contamination.	103
V.7 Radial distributions of internal and external contaminations.	106
V.8 Phase Foxtrot. Fit of the radial distribution before any purification.	107
V.9 Phase Oscar. Fit of the radial distribution before any purification.	108

V.10 Phase Oscar. Energy spectrum of the sample of events selected by means of the scintillation cuts, in the energy region above the lower limit of the neutrino window.	110
V.11 Energy spectra in CTF before and after the scintillator purification.	111

List of Tables

I.1	Values of R/E and Δm^2 accessible in experiments looking to neutrinos from several sources (from [Bah89, BV87]).	3
I.2	The pp cycle reactions	7
I.3	The CNO cycle reactions	7
I.4	Prediction of the Bahcall, Basu and Pinsonneault 98 SSM [BBP98]: solar neutrino fluxes and neutrino capture rates, with 1σ uncertainties from all sources (combined quadratically). The neutrinos capture rates are measured in Solar Neutrino Unit (SNU) equivalent to 10^{-36} captures per target atom per second.	9
II.1	Local γ background in the LNGS underground Halls.	21
II.2	Local neutron background in the LNGS underground Halls (From ref. [B ⁺ 89]).	21
II.3	Radiopurity requests for water in Borexino and in the Counting Test Facility compared to the output of the Water Purification Plant.	22
II.4	Decay times and probabilities for the different scintillation component in case of emission excited by α or $\beta+\gamma$ radiation, as a result of laboratory measurement [RGL98].	26
II.5	Radioactive impurity levels in the Borexino materials	31
II.6	Expected external γ background rates (events/day in a 100 tons fiducial volume) in the neutrino window according to the different sources. Infinite energy resolution assumed.	31
II.7	Internal background estimate (events/day in a 100 tons fiducial volume) after successive cut analysis. The following contaminations are assumed: ^{238}U : 10^{-16} g/g at the chain equilibrium; ^{232}Th : 10^{-16} g/g at the chain equilibrium; $^{\text{nat}}\text{K}$: 10^{-14} g/g. Infinite spatial and energy resolution are also assumed.	32
II.8	Cosmogenic radionuclides in the scintillator.	36
II.9	Cosmic ray background rates in the energy range 0.25–1.50 MeV in units of events/day after the application in series of the cuts. For delayed events, the delay time cut is included. . . .	37
IV.1	Results of the measurements of quenching factors and electron equivalent energies for α particles performed in the Munich experiment.	51
IV.2	Decay products, Q values, electron equivalent energies and meanlives for mass 212 sequence nuclides.	53
IV.3	Efficiencies of the Th cuts for the selection of mass 212 sequences.	53
IV.4	Efficiencies of the Th cuts for the selection of mass 212 and of mass 214 sequences.	58
IV.5	Phase Foxtrot. Summary of the results on ^{232}Th contamination.	67
IV.6	Phase Lima. Summary of the results on ^{232}Th contamination.	67
IV.7	Phase Oscar. Summary of the results on ^{232}Th contamination.	68
IV.8	Decay products, Q values, electron equivalent energies and meanlives for the mass 214 sequence nuclides.	70
IV.9	Efficiencies of the U cuts for the selection of the mass 214 sequences.	70
IV.10	Physical and chemical characteristics of Rn.	71
IV.11	Efficiencies of the Kr cuts for the selection of the mass 85 sequences.	82
IV.12	Physical quantities determining the mean capture time of thermal neutrons in water and in PC.	87
IV.13	Efficiencies of the neutron cuts for the selection of the neutron sequences.	88
V.1	Results of the radial analysis disentangling the contribution of the various classes of background to the total counting rate in the neutrino window.	105

Introduction

Since the beginning of the last two decades, the study of neutrinos plays a very prominent role in astrophysics and elementary particle physics.

Presently the question is open whether neutrinos have finite masses or not. An answer to this question would reveal the structure of the possible neutrinos mass term of the Lagrangian and fix the last Yukawa couplings in the Glashow-Salam-Weinberg theory; it would shed a light on the grand unification schemes; likely, it would give a contribution to the “Universe’s missing mass” problem.

Nowadays, a variety of research projects aimed to observe neutrinos coming from different sources are under development. Amongst these, the studies on solar neutrinos have achieved a big relevance: the characteristics and the singleness of the beam (distance between source and target ~ 1 AU) allow to examine the mass spectrum down to lowest values today reachable.

Up to date four different experiments have been measuring solar neutrino fluxes. The main result of their observations is the record of a solar neutrinos flux from two to three times lower than expected by the Standard Models of Stellar evolution. The discrepancy between the measured and the expected fluxes is known as the “Solar Neutrino Problem” (SNP).

The four experiments in run up to date can be considered as “first generation experiments” and are characterized either by the accumulation technique (which does not permit to keep track of the energy of the neutrino and of the interaction time) or by high energy thresholds. To solve the SNP it is invoked a second generation of detectors characterized by real time and high statistics data taking, low energy thresholds and possibly the ability to distinguish the charged from the neutral current contributions to the interaction amplitudes.

The Borexino (BX) experiment, located in the Laboratori Nazionali del Gran Sasso (LNGS) of the Istituto Nazionale di Fisica Nucleare (INFN), is a real time and high statistics detector for ${}^7\text{Be}$ neutrinos. BX is a 300 tons unsegmented liquid scintillation detector designed to detect recoil electrons from ν -e scattering.

The shielding of the environmental radioactivity and the achievement of a low intrinsic radiopurity of the construction materials constitute essential requirements for the feasibility of the experiment. The key of the experiment is the achievement of a radiopurity of the scintillator at the levels of 10^{-18} for the ratio ${}^{14}\text{C}/{}^{12}\text{C}$ and of 10^{-16} g/g for the isotopes ${}^{238}\text{U}$ and ${}^{232}\text{Th}$.

The first phase of the experiment consisted in a smaller scale prototype, the Counting Test Facility of BX (CTF). The CTF has been built in the Hall C of the LNGS with the aim of verifying the possibility to achieve the project’s values of radiopurity of the scintillator on a large mass scale.

The candidate has been involved in the implementation of the CTF experiment. His main research area has been the analysis of the data recorded by the CTF. The candidate presently is participating in the construction of the BX experiment.

Chapter I

So tiny and vanishing

I-A Open questions on neutrinos

Neutrinos are the most elusive between the known particles. They have a very low masses, if any. They interact only exchanging ultra-massive (80–90 GeV) electroweak bosons. Therefore at energies lower than the electroweak unification scale they have very low cross section for the interaction with the components of the ordinary matter (electrons, protons and neutrons). Hence no surprise in remembering that a quarter of a century lasted from the theoretical prediction of neutrinos (Pauli 1930 [Pau30]) up to their experimental observation (Reines and Cowan 1953 [RC53]).

Still three fundamental questions on neutrinos are unanswered:

- are neutrinos massive or not?
- are neutrinos Majorana or Fermi particles?
- which is the reason for the large mass difference between the charged and neutral sector of the leptons?

An answer to these questions would give a relevant contribution to the “Universe’s missing mass” problem and it would shed a light on the great unification theories.

New experiments to explore the neutrinos world are under development. In the context, the next section will describe a particular class of neutrino experiments which seems today to be very promising.

I-B Neutrino oscillation experiments

The neutrinos mass matrix may be non-diagonal when expressed in the flavour eigenstates basis, or, equivalently, the weak lepton current may be non-diagonal when expressed in the mass eigenstates basis. In the case, since neutrinos are emitted from the sources as flavour eigenstates, the wave function describing freely propagating particles in the vacuum will have several free components. The relative phases of these components will vary in time and space as a function of masses. Therefore the probability that neutrinos conserve the original flavour will vary periodically with the distance from the detector, hence the name of “neutrino oscillations”. Thus, the primary motivation for exploring neutrino oscillations is the determination of the neutrino mass matrix.

Let us indicate with ν_a ($a = 1, 3$) a basis of neutrino mass eigenstates and with ν_α ($\alpha = 1, 3$) a basis of neutrino flavour eigenstates. The two basis are connected by a linear transformation:

$$\nu_\alpha = U_{\alpha a} \nu_a \quad (\text{I.1})$$

Neutrinos can oscillate only if the matrix U is not diagonal: it is necessary that neutrinos are massive and that their masses are not degenerate.

Let us consider a beam of neutrinos emitted in a flavour definite state α with equal momentum p . The corresponding wave function at the emission point is:

$$\Psi(x = 0, t = 0) = \nu_\alpha = \sum_{a=1}^3 U_{\alpha a} \nu_a \quad (\text{I.2})$$

Table I.1: Values of R/E and Δm^2 accessible in experiments looking to neutrinos from several sources (from [Bah89, BV87]).

Neutrino Source	R/E [m/MeV]	Δm^2 [eV ²]
Accelerator	$10^{-2}-10^1$	$10^{-2}-10^1$
Reactor	10^0-10^2	$10^{-3}-10^{-1}$
Atmospheric	10^2-10^4	$10^{-5}-10^{-3}$
Solar	$10^{10}-10^{11}$	$10^{-12}-10^{-11}$
Supernova	$10^{19}-10^{20}$	$10^{-20}-10^{-21}$

the wave function propagated at the point x and at the time t is:

$$\Psi(x, t) = \sum_{a=1}^3 U_{\alpha a} \nu_a e^{-i(E_a t - p x)} \quad (I.3)$$

assuming that the masses m_a are much lower than the momentum p , the energies of the components can be approximated by:

$$E_a = \sqrt{m_a^2 + p^2} \simeq p + \frac{m_a^2}{2p} \quad (I.4)$$

hence the propagated wave function becomes:

$$\Psi(x, t) = U_{\alpha a} \nu_a e^{-i(p(t-x) + t m_a^2 / 2p)} \quad (I.5)$$

and the energy splitting of the mass eigenstates is:

$$\Delta E_{V(ab)} = \frac{|m_a^2 - m_b^2|}{2p} \quad (I.6)$$

The probability to detect neutrinos with the original flavour α at the distance x from the detector ($t \simeq x$) is:

$$P_{\alpha\alpha} = \left| \sum_{a=1}^3 \sum_{b=1}^3 U_{\alpha a}^* U_{\alpha b} e^{-i x m_a^2 / 2p} \right|^2 \quad (I.7)$$

$$= \sum_{a=1}^3 |U_{\alpha a}|^4 + \sum_{a=1}^3 \sum_{b \neq a} |U_{\alpha a} U_{\alpha b}|^2 \cos \left(\frac{x (m_a^2 - m_b^2)}{2E} \right) \quad (I.8)$$

the above probability varies with the distance. Neutrinos oscillate between the mass states a and b with the oscillation length:

$$L_{V(ab)} = \frac{4\pi E}{|m_a^2 - m_b^2|} \quad (I.9)$$

$$= \frac{2\pi}{\Delta E_{V(ab)}} \quad (I.10)$$

$$L_{V(ab)} [\text{m}] \simeq \frac{2.48 \times E [\text{MeV}]}{|m_a^2 - m_b^2| [\text{eV}^2]} \quad (I.11)$$

therefore the sensitivity of an experiment to the neutrino masses is:

$$\Delta m^2 [\text{eV}^2] \sim \frac{E [\text{MeV}]}{R [\text{m}]} \quad (I.12)$$

table I.1 reports the values of R/E and of the mass sensitivity for various classes of neutrino oscillation experiments.

Let us now suppose that the relevant oscillation involves only two mass eigenstates. The matrix U can be expressed in form of a rotation matrix characterized by the vacuum mixing angle Θ_v :

$$\begin{pmatrix} \cos \Theta_v & \sin \Theta_v \\ -\sin \Theta_v & \cos \Theta_v \end{pmatrix} \quad (\text{I.13})$$

equation I.7 reduces to:

$$P_{\alpha\alpha} = \cos^4 \Theta_v + \sin^4 \Theta_v + \cos^2 \Theta_v \sin^2 \Theta_v \cos \left(\frac{2\pi x}{L_v} \right) \quad (\text{I.14})$$

$$= 1 - \sin^2 2\Theta_v \sin^2 \left(\frac{\pi x}{L_v} \right) \quad (\text{I.15})$$

therefore the space of the mixing angles is explorable down to the range of the tenths of radiant.

So far we discussed the neutrino oscillations in vacuum. The phenomenon of oscillations obeys to different laws when neutrinos are propagating in matter. Neutrino oscillations in matter are also called MSW oscillations, from the names of the pioneer investigators Mikeyev, Smirnov and Wolfenstein (see references [Wol78] and [MS85]). The interaction of neutrinos with the matter fields is accounted for in the propagated wave function by the refraction index n :

$$\Psi(x, t) = \sum_{a=1}^3 U_{\alpha a} \nu_a e^{-i(E_a t - p_n x)} \quad (\text{I.16})$$

the refraction index depends on the product (averaged over the various matter fields) of the density N and of the forward elastic scattering amplitude for neutrinos $f(0)$:

$$n = 1 + \frac{2\pi N f(0)}{p^2} \quad (\text{I.17})$$

Matter is composed by quarks and electrons. The amplitudes for neutrinos scattering on the quarks are flavour independent since interactions are mediated by the Z_0 boson. The amplitudes for neutrinos scattering on electrons are flavour dependent: the contribution corresponding to the interaction mediated by the W^+ and W^- bosons is present only for electron neutrinos, whereas the contribution corresponding to the interaction mediated by the Z_0 boson is flavour independent. From reference [L⁺83]:

$$f_e(0) - f_x(0) = \Delta f(0) = -\frac{\sqrt{2}G_F p}{2\pi} \quad (\text{I.18})$$

Therefore the electron neutrino wave function phase varies in space with respect to the other neutrinos phases according to:

$$\nu_e(x) \propto e^{-i\sqrt{2}xN_eG_F} \quad (\text{I.19})$$

in the literature it is defined the electron-neutrino interaction length $L_{e\nu}$ as the length at which the above phase difference equals 2π . The oscillation length $L_{e\nu}$ depends on the electron density:

$$L_{e\nu} = \frac{2\pi}{\sqrt{2}N_eG_F} \quad (\text{I.20})$$

$$L_{e\nu}[\text{m}] \simeq \frac{1.7 \times 10^7}{\rho[\text{g}/\text{cm}^{-3}] \langle Z/A \rangle} \quad (\text{I.21})$$

and it amounts to roughly 200 Km in the sun's core and to is 10^4 Km in the earth.

In the flavour eigenstate basis the time development equation can be reduced to the following expression, with the effective hamiltonian already in traceless form:

$$i \frac{d}{dt} \begin{pmatrix} \nu_e \\ \nu_\mu \end{pmatrix} = \begin{pmatrix} A & B \\ B & -A \end{pmatrix} \begin{pmatrix} \nu_e \\ \nu_\mu \end{pmatrix} \quad (\text{I.22})$$

$$A = -\frac{\Delta m^2}{4E} (\cos^2 \Theta_v - \sin^2 \Theta_v) + \frac{\sqrt{2}}{2} G_F N_e \quad (\text{I.23})$$

$$= -\frac{\Delta E_V}{2} \cos 2\Theta_v + \frac{\sqrt{2}}{2} G_F N_e \quad (\text{I.24})$$

$$B = -\frac{\Delta m^2}{4E} \cos \Theta_v \sin \Theta_v \quad (\text{I.25})$$

$$= -\frac{\Delta E_V}{2} \sin 2\Theta_v \quad (\text{I.26})$$

The mixing angle in matter is the angle characterizing the rotation matrix which diagonalizes the hamiltonian:

$$\tan 2\Theta_m = -\frac{B}{A} = \frac{\tan 2\Theta_v}{1 - \frac{L_V}{L_{e\nu}} \sec 2\Theta_v} \quad (\text{I.27})$$

the eigenvalues of the above matrix are:

$$\pm \sqrt{A^2 + B^2} = \frac{1}{2} \sqrt{(\Delta E_V \cos 2\Theta_v - \sqrt{2} G_F N_e)^2 + (\Delta E_V \sin 2\Theta_v)^2} = \pm \frac{\Delta E_M}{2} \quad (\text{I.28})$$

and matter oscillation length can be expressed as a function of the energy splitting of the two neutrino plane waves in matter:

$$L_M = \frac{2\pi}{\Delta E_M} = L_V \frac{\sin 2\Theta_m}{\sin 2\Theta_v} \quad (\text{I.29})$$

Equation I.27 shows the resonant character of matter oscillations. Also in case of a very small vacuum mixing angle Θ_v a great matter mixing angle is reached at the resonance condition:

$$\cos 2\Theta_v = \left(\frac{L_V}{L_{e\nu}} \right) \quad (\text{I.30})$$

The matter resonant density is:

$$N_e = \frac{|\Delta m^2| \cos 2\Theta_v}{2\sqrt{2} G_F E} \quad (\text{I.31})$$

in the case of solar neutrinos propagating into the sun, the minimal mass that can be explored is fixed by the scale of nuclear energies and by the electron density in the sun's core ($(N_e)_{\max} \sim 150 \text{ g/cm}^{-3}$):

$$\Delta m^2 \sim G_F E (N_e)_{\max} \simeq 10^{-5} [\text{eV}^2] \quad (\text{I.32})$$

In a variable density medium like the sun, the lowest explorable angles are those for which the matter oscillation length equals the linear dimensions of the resonance width Δr (r indicates the solar radius):

$$\frac{\Delta r}{L_M} = \frac{\Delta E_V \sin 2\Theta_v \frac{dr}{dE}}{\frac{L_V}{\sin 2\Theta_v}} \quad (\text{I.33})$$

$$= \frac{\Delta m^2 \sin 2\Theta_v \tan 2\Theta_v}{2\pi E |N_e^{-1} dN_e/dr|} \quad (\text{I.34})$$

and according to reference [Bah89]:

$$\sin 2\Theta_v \tan 2\Theta_v = 4 \times 10^{-9} \left(\frac{E [\text{MeV}]}{\Delta m^2 [\text{eV}^2]} \right) \quad (\text{I.35})$$

therefore the minimum explorable angle is 10^{-2} rad.

I-C Solar neutrinos

The sun is a powerful source of neutrinos. Due to the long distance between sun and earth, the search for vacuum oscillations in the frame of solar neutrinos allows to explore differences in the squared masses much lower than it is possible with any terrestrial source. Solar neutrinos allow also to study resonant oscillation in matter by means of the phenomena of flavour conversion in the sun's core and regeneration in the earth.

Solar neutrinos are produced in nuclear fusion processes producing the energy irradiated by the sun. Two fusion cycles are burning hydrogen in the sun's core:

- The proton-proton (pp) cycle consists of several reactions resulting in the net transformations:

$$4p \rightarrow \alpha + 2e^+ + 2\nu_e \quad (\text{I.36})$$

or

$$4p + e^- \rightarrow \alpha + e^+ + 2\nu_e \quad (\text{I.37})$$

Each possible series of reaction giving rise to this transformation is called a termination of the cycle. Table I.2 describes the reactions and the terminations of the pp cycle.

- The Carbon-Nitrogen-Oxygen (CNO) cycle consists of two possible terminations. The first termination results in the same net transformation as the pp cycle, but it involves the presence of CNO nuclides as collaborating spectators:

$$4p \rightarrow \alpha + 2e^+ + 2\nu_e \quad (\text{I.38})$$

the second termination results in the net transformation:

$$6p + {}^{12}\text{C} \rightarrow \alpha + 3e^+ + 3\nu_e + {}^{14}\text{N} \quad (\text{I.39})$$

Table I.3 describes the reactions and the terminations of the CNO cycle.

A stellar model is a solution to the evolutionary equation of the star. The boundary conditions are given by mass, radius, luminosity and age of the star.

The Standard Solar Model (SSM) is a stellar model tailored on the closest and best known star. The SSM gives a quantitative description of the sun. It is based upon results of sun observation, laboratory measurements of nuclear reactions cross sections and theoretical predictions. The main inputs of the model are:

- solar luminosity;
- solar age;
- equation of state;
- initial elemental abundances;
- radiative opacity
- nuclear parameters.

The SSM allows to reconstruct the present values for the distributions of temperatures, density, energy production and elemental abundances (of light elements in the sun's core).

Several Standard Solar Models have been developed by different authors. The results of all the models are essentially in agreement (see reference [BKS98]). In the following it will be often cited as a representative for the SSMs the model of Bahcall, Basu and Pinsonneault 1998 (BBP 98, see reference [BBP98]).

The accuracy of the SSM predictions can be checked directly against experimental data. In the last few years observations on helioseismic activity from five different experiments [LBB⁺97, GTC⁺97, GMB⁺] determined the distribution of the sound speed in the sun's interior. The sound speed c depends essentially upon the local temperature and mean molecular weight: $c^2 \propto T/\mu$. In the SSM, T and μ vary respectively by a factor 50 and 1.5 over the entire range for which c has been measured (to say from 0.05 to 0.95 of the solar radius). They vary respectively by a factor 1.9 and 1.4 in the inner energy production region. Hence the comparison of the sound speed deduced from the SSM with the experimental values allows a narrow check of the SSM.

The BBP 98 SSM provides an excellent agreement of the predicted radial distribution of the sound speed with the experimental values. Figure I.1 shows that the fractional difference between the two distributions is much smaller than generic changes in the model that could significantly affect the prediction of the solar neutrinos fluxes.

The SSM allows to deduce the present values of the solar neutrino fluxes. Table I.4 reports the fluxes calculated in BBP 98 SSM and figure I.2 reports the corresponding energy spectrum.

I-C.1 The experiments on solar neutrinos

Up to day four different experiments measured neutrino fluxes from the sun. We will give a short introduction to each of these experiments and a summary of their results.

the Chlorine experiment [CDD⁺98]

The experiment of Davis and collaborators started in 1968. It was for almost two decades the only operating solar neutrino detector.

The reaction that is used to detect solar neutrinos is the inverse of ${}^{37}\text{Ar}$ decay. The neutrino absorption reaction is:

$$\nu_e + {}^{37}\text{Cl} \rightarrow e^- + {}^{37}\text{Ar} \quad (\text{I.40})$$

Table I.2: The pp cycle reactions

Reaction		Q [MeV]	E_{ν_e} [MeV]	$\langle q_{\nu_e} \rangle$ [MeV]
$p + p \rightarrow {}^2\text{H} + e^+ + \nu_e$	(pp)	1.442	≤ 0.420	0.265
or				
$p + e^- + p \rightarrow {}^2\text{H} + \nu_e$	(pep)	1.442	1.442	1.442
${}^2\text{H} + p \rightarrow {}^3\text{He} + \gamma$		5.494		
${}^3\text{He} + {}^3\text{He} \rightarrow \alpha + 2p$		12.860		
or				
${}^3\text{He} + {}^4\text{He} \rightarrow {}^7\text{Be} + \gamma$		1.586		
${}^7\text{Be} + e^- \rightarrow {}^7\text{Li} + \nu_e$	(${}^7\text{Be}$)	0.862 (90%) 0.383 (10%)	0.862 0.383	0.862 0.383
${}^7\text{Li} + p \rightarrow 2\alpha$		17.347		
or				
${}^7\text{Be} + p \rightarrow {}^8\text{B} + \gamma$		0.137		
${}^8\text{B} \rightarrow {}^8\text{Be}^* + e^+ + \nu_e$	(${}^8\text{B}$)	17.980	≤ 15.0	6.71
or				
${}^3\text{He} + p \rightarrow {}^4\text{He} + e^+ + \nu_e$	(hep)	19.795	≤ 18.8	9.27

Table I.3: The CNO cycle reactions

Reaction		Q [MeV]	E_{ν_e} [MeV]	$\langle q_{\nu_e} \rangle$ [MeV]
${}^{12}\text{C} + p \rightarrow {}^{13}\text{N} + \gamma$		1.943		
${}^{13}\text{N} \rightarrow {}^{13}\text{C} + e^+ + \nu_e$	(${}^{13}\text{N}$)	2.221	≤ 1.199	0.7067
${}^{13}\text{C} + p \rightarrow {}^{14}\text{N} + \gamma$		7.551		
${}^{14}\text{N} + p \rightarrow {}^{15}\text{O} + \gamma$		7.297		
${}^{15}\text{O} \rightarrow {}^{15}\text{N} + e^+ + \nu_e$	(${}^{15}\text{O}$)	2.754	≤ 1.732	0.9965
${}^{15}\text{N} + p \rightarrow {}^{12}\text{C} + \alpha$		4.966		
or				
${}^{15}\text{N} + p \rightarrow {}^{16}\text{O} + \gamma$		12.128		
${}^{16}\text{O} + p \rightarrow {}^{17}\text{F} + \gamma$		0.600		
${}^{17}\text{F} \rightarrow {}^{17}\text{O} + e^+ + \nu_e$	(${}^{17}\text{F}$)	2.762	≤ 1.740	0.9994
${}^{17}\text{O} + p \rightarrow {}^{14}\text{N} + \alpha$				

the reaction threshold of 814 KeV permits the detection of all of the major solar neutrinos sources except the basic pp reactions. As it is shown in table I.4 the main contributions to the expected capture rate of $7.7^{+1.2}_{-1.0}$ Solar Neutrino Units come from the ^8B and ^7Be neutrinos. One Solar Neutrino Unit (SNU) is equivalent to 10^{-36} captures per target atom per second.

The experiment located in a mine close to Homestake, South Dakota at the depth of 4100 meters of water equivalent (mwe). The neutrino target is 2.2×10^{30} nuclides of ^{37}Cl in the form of 615 tons of perchloroethylene (C_2Cl_4 , chlorine).

The ^{37}Ar nuclides produced by solar neutrinos have a meanlife of 51 d. They are accumulated for a couple of months in the bulk chlorine. Then they are separated and concentrated in low background detectors where their decays are measured.

The measured counting rate is roughly one third of the predicted value: 2.56 ± 0.23 SNU.

GALLEX and SAGE [GcH⁺96, ScG⁺98]

GALLEX and SAGE are two similar radiochemical experiments.

The reaction that is used to detect solar neutrinos is the inverse of ^{71}Ge decay:

$$\nu_e + ^{71}\text{Ga} \rightarrow e^- + ^{71}\text{Ge} \quad (\text{I.41})$$

the reaction has a low threshold of 233 KeV which made possible the first observation of the basic pp neutrinos. The radioactive ^{71}Ge decay by electron capture with a meanlife of 17 d. As reported in table I.4, the predicted capture rate is 129^{+8}_{-6} SNU and it is contributed mainly by pp, ^7Be and ^8B neutrinos.

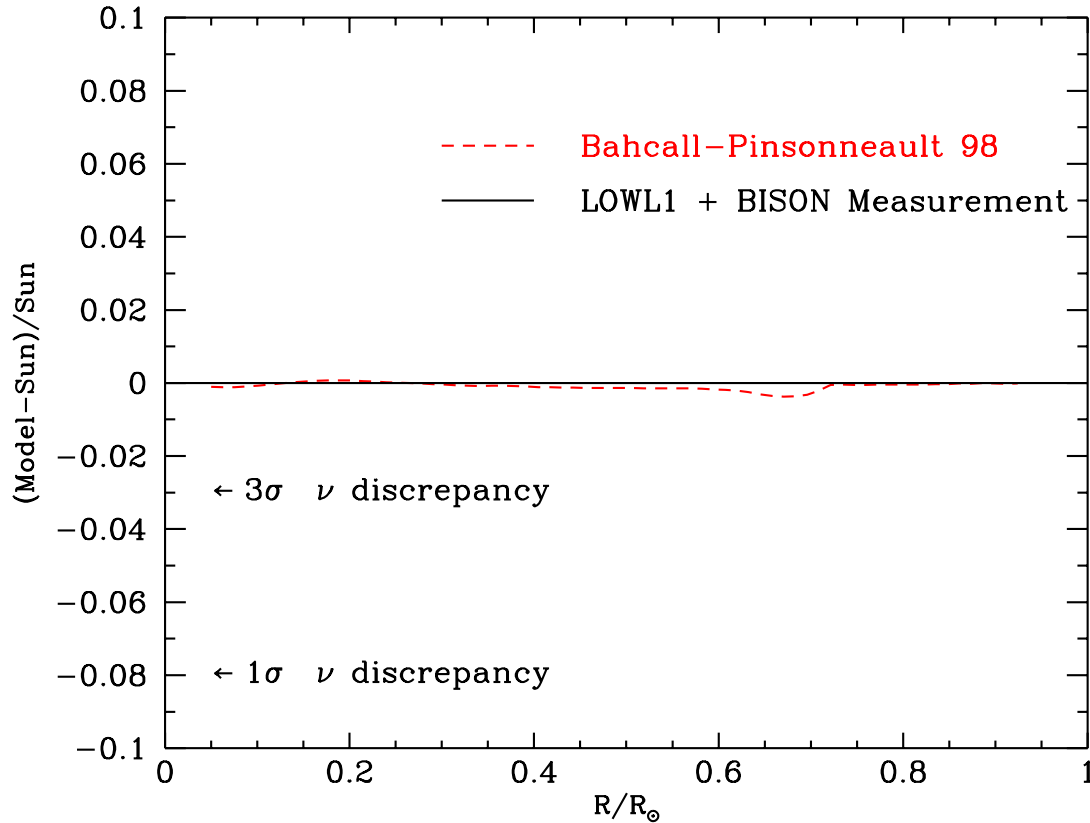


Figure I.1: Prediction of the Bahcall, Basu and Pinsonneault 98 SSM [BBP98]: sound speed in the sun. This figure shows the excellent agreement between the calculated and the measured sound speeds, a fractional difference of 10^{-3} rms for all speeds measured between 0.05 and 0.95 of the solar radius. The vertical scale is chosen so as to emphasize that the fractional error is much smaller than generic changes in the model, from 0.03 to 0.08, that might significantly affect the solar neutrino prediction.

Table I.4: Prediction of the Bahcall, Basu and Pinsonneault 98 SSM [BBP98]: solar neutrino fluxes and neutrino capture rates, with 1σ uncertainties from all sources (combined quadratically). The neutrinos capture rates are measured in Solar Neutrino Unit (SNU) equivalent to 10^{-36} captures per target atom per second.

Source	Flux [$10^{10} \text{ cm}^{-2}\text{s}^{-1}$]	Uncertainty	Cl [SNU]	Ga [SNU]
pp	5.94	$1.00^{+0.01}_{-0.01}$	0.0	69.6
pep	1.39×10^{-2}	$1.00^{+0.01}_{-0.01}$	0.2	2.8
hep	2.10×10^{-7}	1.00	0.0	0.0
^7Be	4.80×10^{-1}	$1.00^{+0.09}_{-0.09}$	1.15	34.4
^8B	5.15×10^{-4}	$1.00^{+0.19}_{-0.14}$	5.9	12.4
^{13}N	6.05×10^{-2}	$1.00^{+0.19}_{-0.13}$	0.1	3.7
^{15}O	5.32×10^{-2}	$1.00^{+0.22}_{-0.15}$	0.4	6.0
^{17}F	6.33×10^{-2}	$1.00^{+0.12}_{-0.11}$	0.0	0.1
Total			$7.7^{+1.2}_{-1.0}$	129^{+8}_{-6}

The GALLEX experiment is located in the Hall A of the LNGS at 4000 mwe depth. Its target is 30 tons of Gallium in 60 m³ of GaCl₃ solution. The SAGE experiment is located in the Baksan Laboratory at 4300 mwe depth. Its target is 60 tons of metallic Gallium. The two experiments use different chemical methods to separate the ^{71}Ge nuclides from the bulk material after the accumulation period. The ^{71}Ge nuclides are then concentrated in low background proportional counters where their decays are measured.

The rate expected for both the experiments is 129^{+8}_{-6} SNU, as it is shown in table I.4. The rates detected are roughly one half of the expected values: 78 ± 6 SNU for GALLEX and 67 ± 8 SNU for SAGE.

KamiokaNDE and SuperKamiokaNDE [F⁺98, KcF⁺96]

KamiokaNDE and SuperKamiokaNDE are two twin experiments looking for proton decay (NDE is the acronym of Nucleon Decay Experiment). The active part of the detectors is ultrapure water. Ultrarelativistic charged particles crossing the water produce Čerenkov light observed by photomultiplier tubes. The two experiments are located in the Kamioka mine, Japan, at 2700 mwe depth.

KamiokaNDE started in 1986. The fiducial mass amounted to 680 tons of water which were observed by 948 photomultiplier tubes. In 1994 KamiokaNDE was shutdown and replaced by SuperKamiokaNDE, a larger scale clone detector. The fiducial mass of SuperKamiokaNDE amounts to 22.5 kilotons of water which are observed by 11000 photomultiplier tubes.

KamiokaNDE and SuperKamiokaNDE performed excellent measurements on atmospheric and solar neutrinos.

The two experiments use the following reaction to measure neutrinos:

$$\nu_x + e^- \rightarrow \nu_x + e^- \quad (\text{I.42})$$

the reaction is sensitive also to non electronic flavour neutrinos. The cross section for muonic neutrinos is 6 times lower than the corresponding value for electronic neutrinos at the energy of 10 MeV.

Recently (see [F⁺98]) the SuperKamiokaNDE collaboration notified that evidence for neutrino oscillation in the channel ($\nu_\mu \rightarrow \nu_\tau$, $\Delta m^2 \sim 10^{-3} \text{ eV}^2$, $\sin 2\Theta_\nu \sim 1$) emerged from the zenith angle dependence of the measured flux of atmospheric neutrinos.

As far as solar neutrinos are concerned, the abovementioned reaction is studied with a software threshold of 7.5 MeV in KamiokaNDE and of 6.5 MeV in SuperKamiokaNDE. Therefore the detectors are sensitive only to the ^8B neutrinos.

Once the candidate Čerenkov cone has been reconstructed, software cuts on the position of the interaction point and on the direction of the cone allow to increase the signal/noise ratio. The flux is deduced by fitting the angular distribution of the candidate events with a function composed by a flat background plus a signal peaked around the sun-earth direction.

The flux measured by KamiokaNDE amounts to:

$$\Phi(^8\text{B})_{\text{exp}} = (2.8 \pm 0.4) \text{ cm}^{-2}\text{s}^{-1} \quad (\text{I.43})$$

and it compares with the predicted value as:

$$\frac{\Phi(^8\text{B})_{\text{exp}}}{\Phi(^8\text{B})_{\text{theor}}} = 0.54 \pm 0.07 \quad (\text{I.44})$$

SuperKamiokaNDE measured the flux with a higher accuracy mainly due to higher statistics:

$$\Phi(^8\text{B})_{\text{exp}} = (2.4 \pm 0.1) \text{ cm}^{-2}\text{s}^{-1} \quad (\text{I.45})$$

or equivalently:

$$\frac{\Phi(^8\text{B})_{\text{exp}}}{\Phi(^8\text{B})_{\text{theor}}} = 0.47 \pm 0.02 \quad (\text{I.46})$$

I-C.2 The solar neutrino problem

Figure I.3 reports the comparison between the results of solar neutrino experiments and the predictions of the SSM of Bahcall, Basu and Pinsonneault. The measured solar neutrino fluxes are from two to three times lower than the predicted values, and this discrepancy is known as the “Solar Neutrino Problem” (SNP).

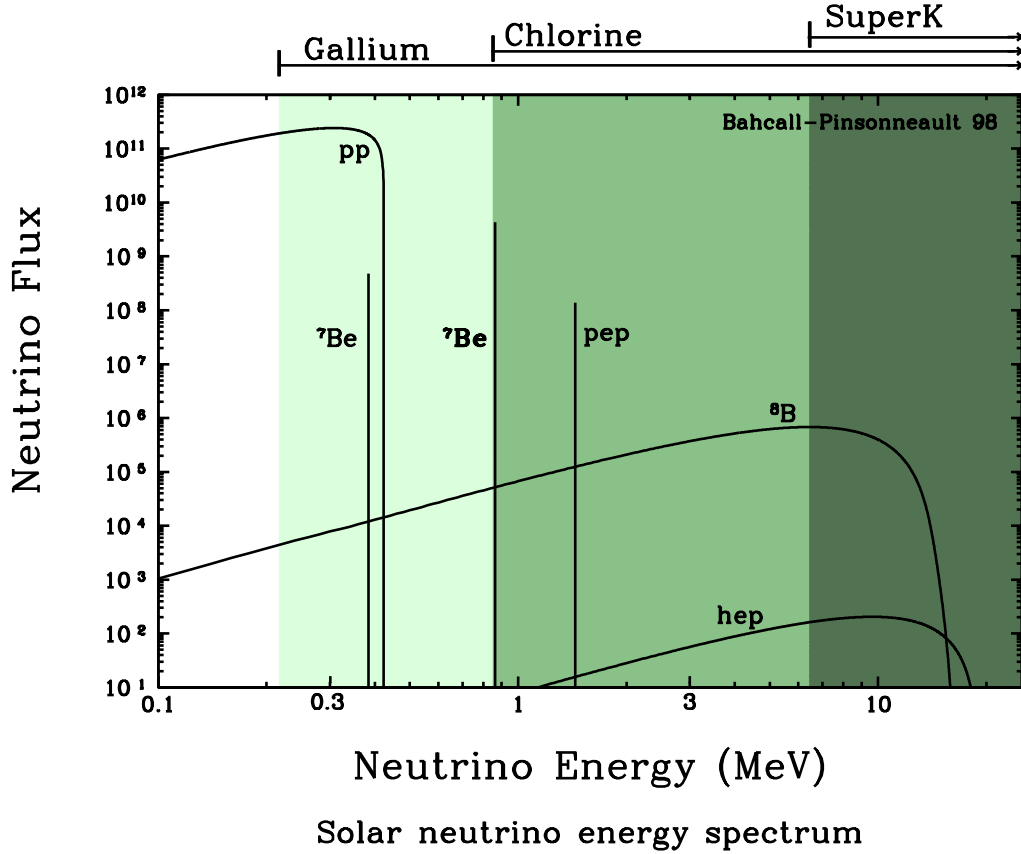


Figure I.2: Prediction of the Bahcall-Basu-Pinsonneault 98 SSM [BBP98]: solar neutrinos spectrum.

Total Rates: Standard Model vs. Experiment Bahcall–Pinsonneault 98

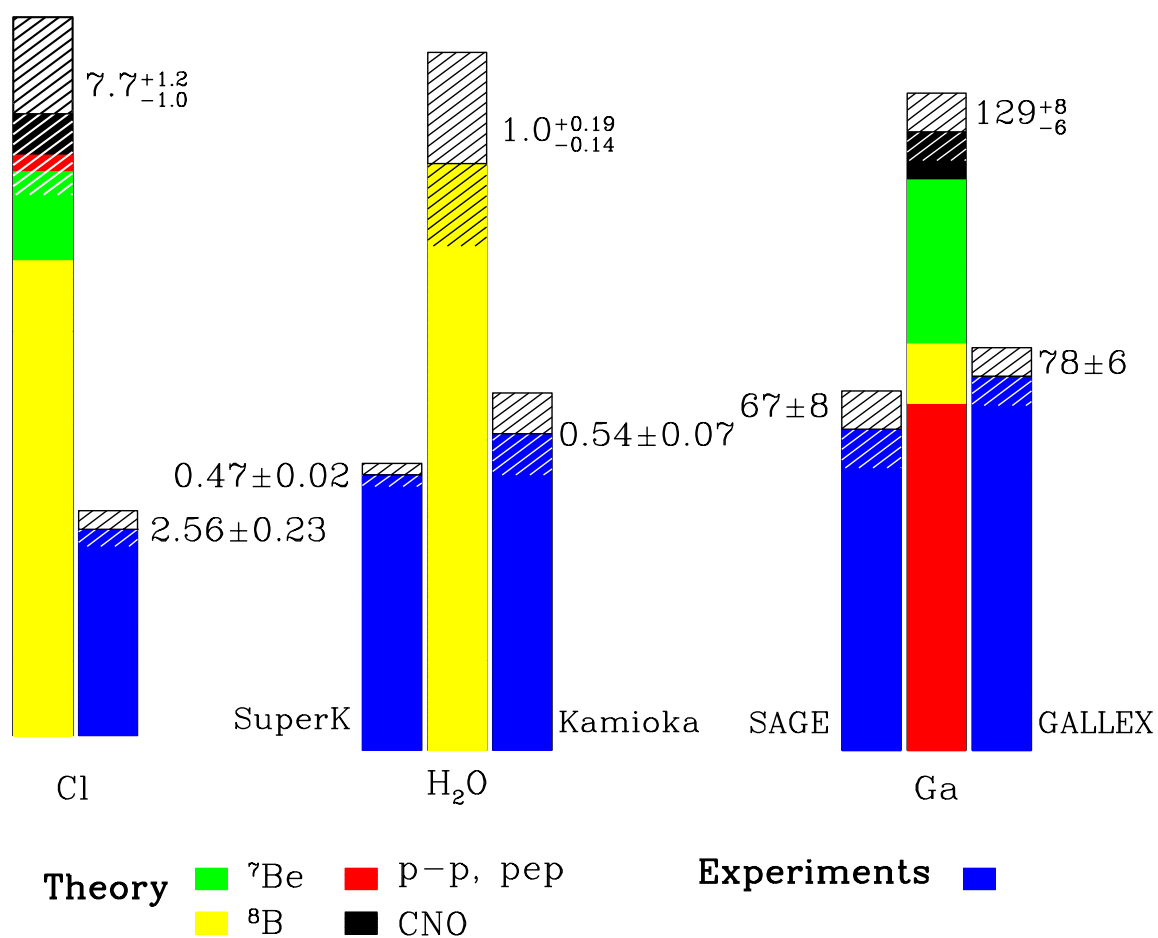


Figure I.3: Comparison of the results from experiments on solar neutrinos with the predictions of the Bahcall, Basu and Pinsonneault 98 SSM.

The disagreement between measurements and prediction does not depend on the details of standard solar model. The basics of the SSM are incompatible with the experimental results on solar neutrinos and with the assumption that non standard neutrino physics is absent, as it was underlined by several authors (see [BKS98] and references cited therein): no room would be left for ${}^7\text{Be}$ neutrinos.

Figure I.4 from reference [BKS98] reports the results of all the SSM developed since 1991 so far in the plane of the fluxes for ${}^7\text{Be}$ and ${}^8\text{B}$ neutrinos. These fluxes are normalized to the values predicted by the BBP 98 SSM. Referring to the analysis in [BKS98] which follows the original analysis of Hata, Bludman and Langacker [HBL94], the best fit values on experimental data for the fluxes of ${}^7\text{Be}$ and ${}^8\text{B}$ neutrinos are reported. The fit is obtained under the hypothesis that non standard neutrino physics is absent. Free parameters of the fit are the fluxes of neutrino sources belonging to the pp fusion cycle. Constraints are the solar luminosity and the results of the four experiments on solar neutrinos. The fluxes of the neutrinos sources belonging to the CNO fusion cycle, which enter the relation providing the constraint on solar luminosity, are arbitrarily set to reasonable values. The fit is free from assumptions on the details of the nuclear physics and astrophysics determining the branching ratios of the pp fusion cycles. The best fit point corresponds to a negative ${}^7\text{Be}$ flux and it is very far from every SSM solution. Furthermore, if the fluxes for CNO neutrinos are assumed at the level of the SSM predictions, there are no solutions for all the neutrino fluxes positive at 99.9 % C.L.. If the fluxes for CNO neutrinos are arbitrarily set equal to zero, there are no acceptable solutions at 99 % C.L..

The unphysical result of a best fit negative ${}^7\text{Be}$ neutrinos flux has become known as the problem of the missing ${}^7\text{Be}$ neutrinos. One reason that the ${}^7\text{Be}$ neutrinos appear to be missing is that the two gallium experiments have an average event rate of 72.3 ± 5.6 SNU, which is fully accounted for by the fundamental pp and pep neutrinos (72.4 SNU). In addition, the ${}^8\text{B}$ neutrinos that are observed in SuperKamiokaNDE will produce about 6 SNU in the gallium experiments, unless new particle physics changes the neutrino energy spectrum. A second reason that the ${}^7\text{Be}$ flux appears to be missing is that the SuperKamiokaNDE ${}^8\text{B}$ neutrino flux alone corresponds to 2.70 ± 0.3 SNU in the chlorine detector, which is fulfilling the capture rate observed in Homestake. There is no room in the measured chlorine rate for a significant ${}^7\text{Be}$ neutrino contribution (expected to be at 1.15 SNU).

Flavour conversion of neutrinos could explain the reduction of the detected flux, since all the experiments run so far have electron neutrinos cross sections higher than other flavour neutrinos cross sections. Both the neutrino oscillation mechanisms introduced so far - vacuum oscillation and matter resonant oscillation - could explain the SNP in terms of flavour conversion. Solutions of the SNP based on neutrino oscillations are very popular because they allow to explain the experimental results got so far on solar neutrinos on the basis of a simple and elegant mechanism.

According to reference [BKS98], three different solutions are allowed if the total rates detected by Chlorine, GALLEX, SAGE and SuperKamiokaNDE and the zenith angle and energy distributions measured by SuperKamiokaNDE are considered:

- MSW oscillation: $\Delta m^2 \simeq 5.4 \times 10^{-6} \text{ eV}^2$ and $\sin^2(2\Theta_\nu) \simeq 5.5 \times 10^{-3}$ (see figure I.5);
- MSW oscillation of electron into sterile neutrinos: $\Delta m^2 \simeq 4.0 \times 10^{-6} \text{ eV}^2$ and $\sin^2(2\Theta_\nu) \simeq 6.9 \times 10^{-3}$ (see figure I.6);
- Vacuum oscillation: $\Delta m^2 \simeq 6.5 \times 10^{-11} \text{ eV}^2$ and $\sin^2(2\Theta_\nu) \simeq 0.75$ (see figure I.7).

Disregarding the energy distribution measured by SuperKamiokaNDE and taking into account only the total rates of Chlorine, GALLEX, SAGE and SuperKamiokaNDE, two other solutions are allowed:

- MSW LMA oscillation: $\Delta m^2 \simeq 1.8 \times 10^{-5} \text{ eV}^2$ and $\sin^2(2\Theta_\nu) \simeq 0.76$ (see figure I.8);
- MSW LOW oscillation: $\Delta m^2 \simeq 7.9 \times 10^{-8} \text{ eV}^2$ and $\sin^2(2\Theta_\nu) \simeq 0.96$ (see figure I.8). The MSW LOW solution has a low probability since it is acceptable only at 99 % C.L..

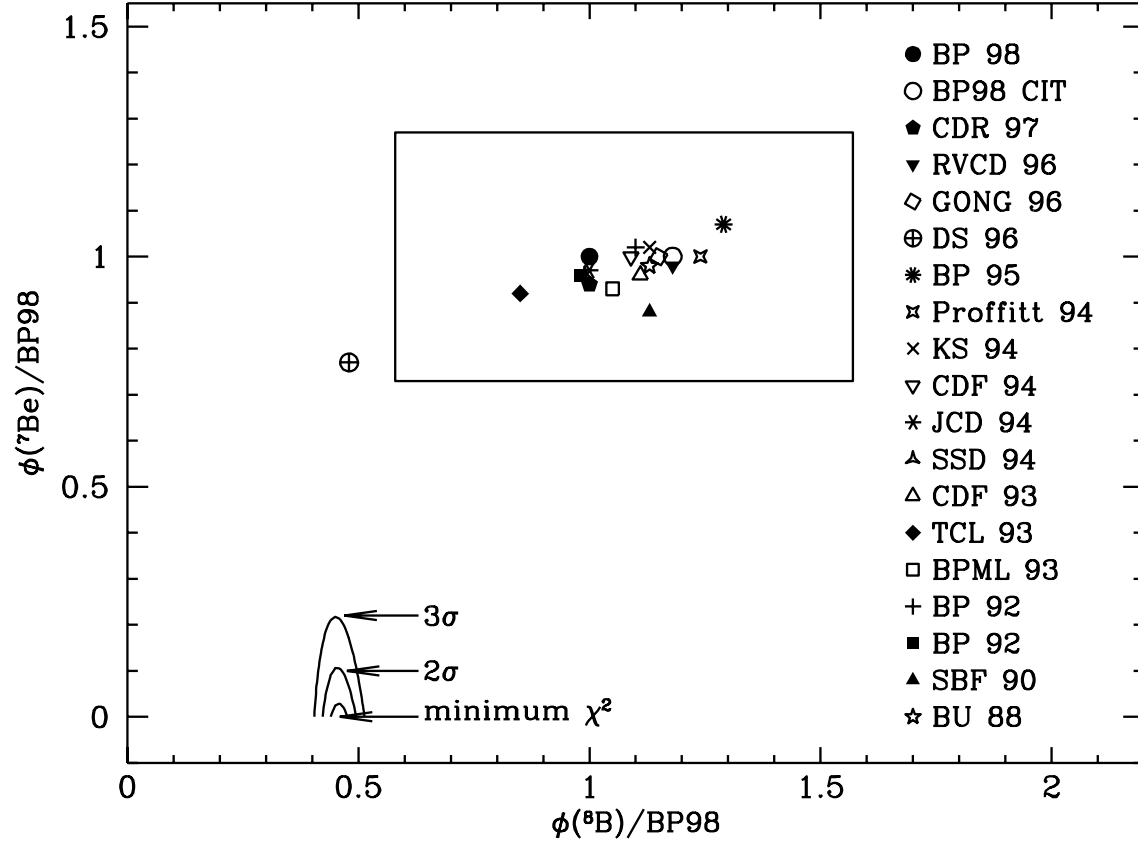


Figure I.4: Predictions of SSMs since 1991. The figure taken from ref. [BKS98] shows the predictions from 19 SSMs in the plane defined by the ${}^7\text{Be}$ and ${}^8\text{B}$ neutrino fluxes and normalized to the predictions of the Bahcall, Basu and Pinsonneault 98 SSM. The rectangular box defines the 3σ error range of the flux predicted by the Bahcall, Basu and Pinsonneault model. The best fit ${}^7\text{Be}$ neutrino flux is negative. At 99 % C.L. there is no solution for all positive neutrino fluxes. All of the SSMs solutions lie far from the best fit solution, event far from the 3σ contour.

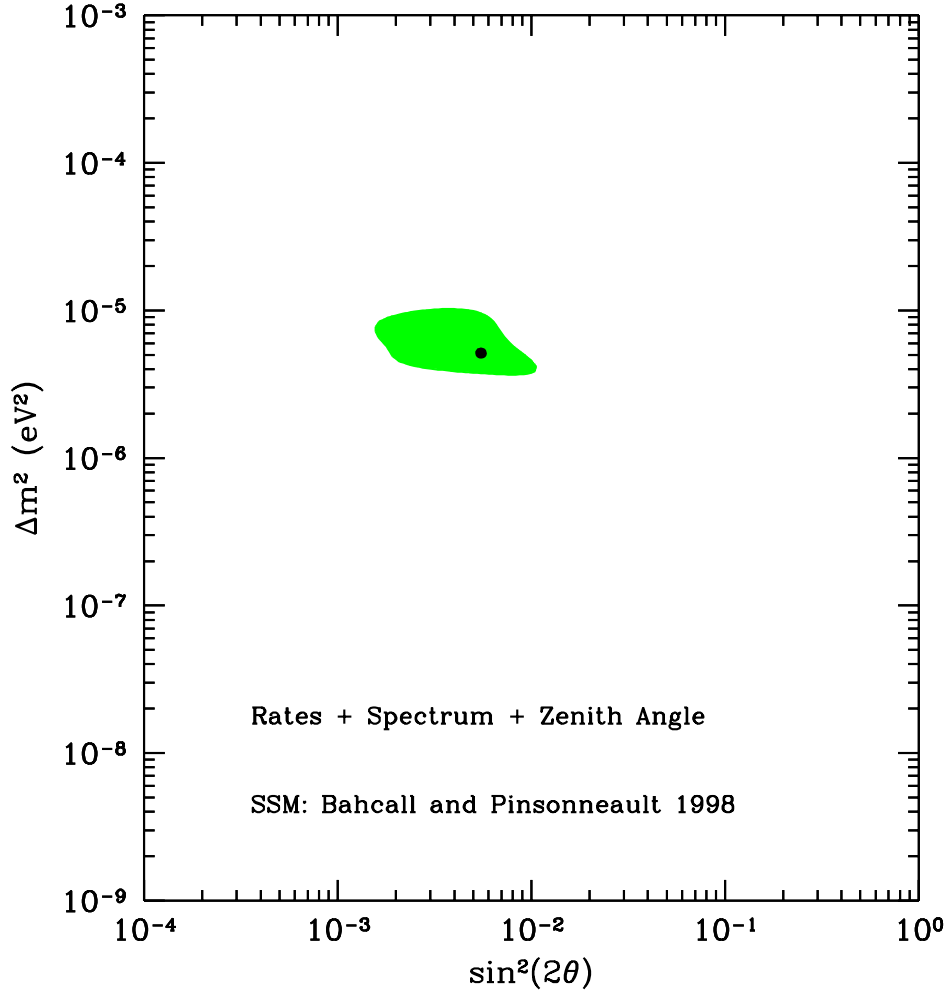


Figure I.5: From [BKS98], MSW solution: the parameter region consistent with the total rates measured in the four experiments and with the electron recoil spectrum and the zenith angle distribution measured in SuperKamiokaNDE. Contours are drawn at 99 % C.L..

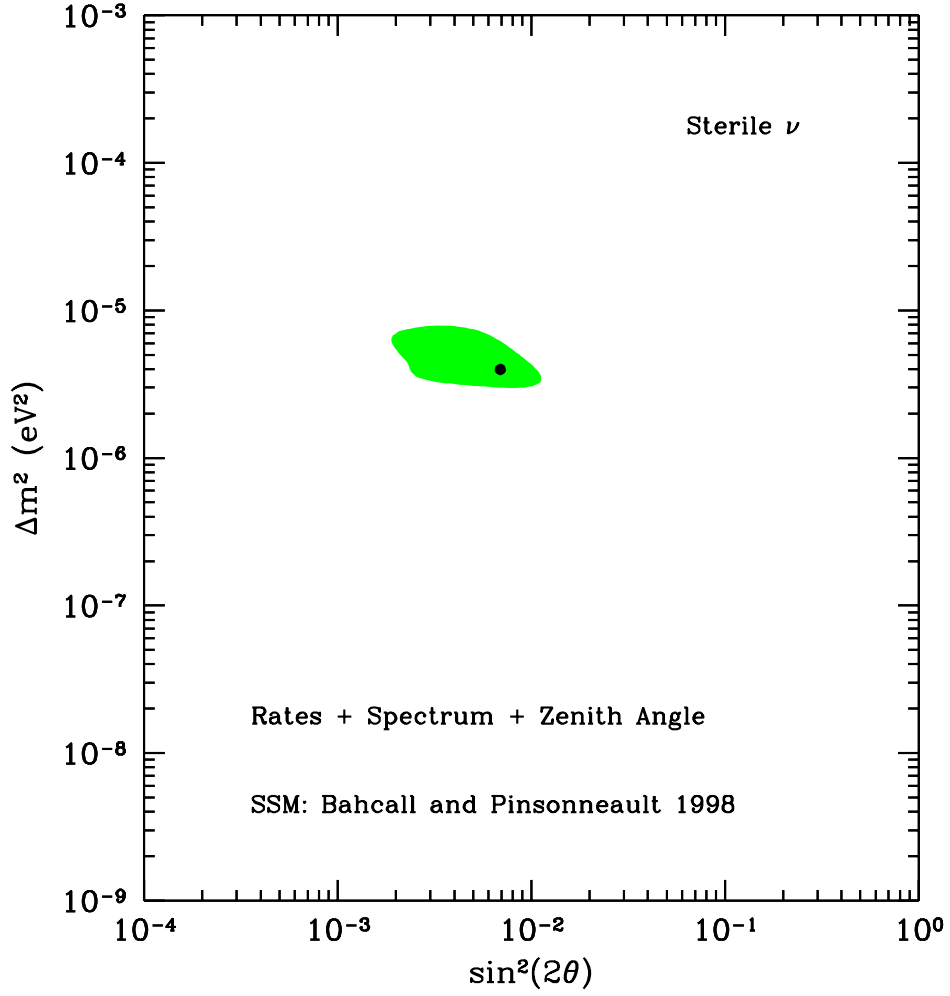


Figure I.6: From [BKS98], MSW oscillation into sterile neutrinos solution: the parameter region consistent with the total rates measured in the four experiments and with the electron recoil spectrum and the zenith angle distribution measured in SuperKamiokaNDE. Contours are drawn at 99 % C.L..

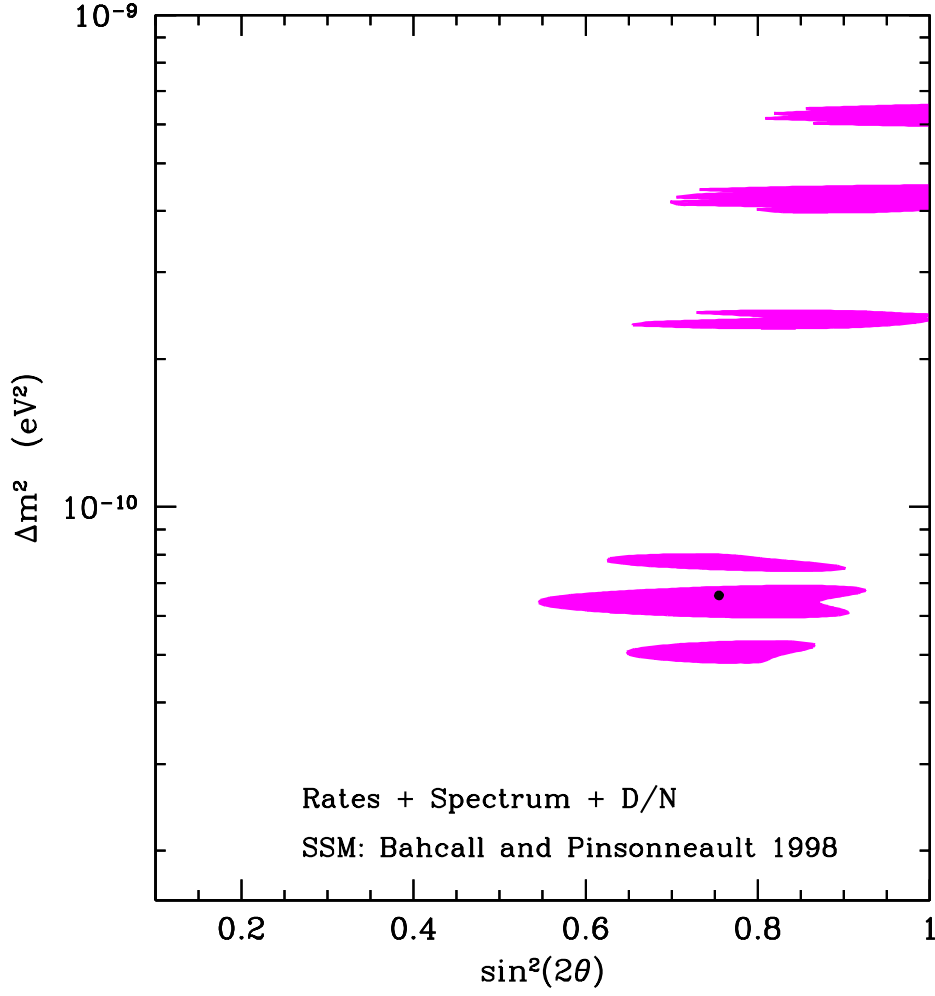


Figure I.7: From [BKS98], vacuum oscillation solution: the parameter region consistent with the total rates measured in the four experiments and with the electron recoil spectrum and the day-night asymmetry measured in SuperKamiokaNDE. Contours are drawn at 99 % C.L..

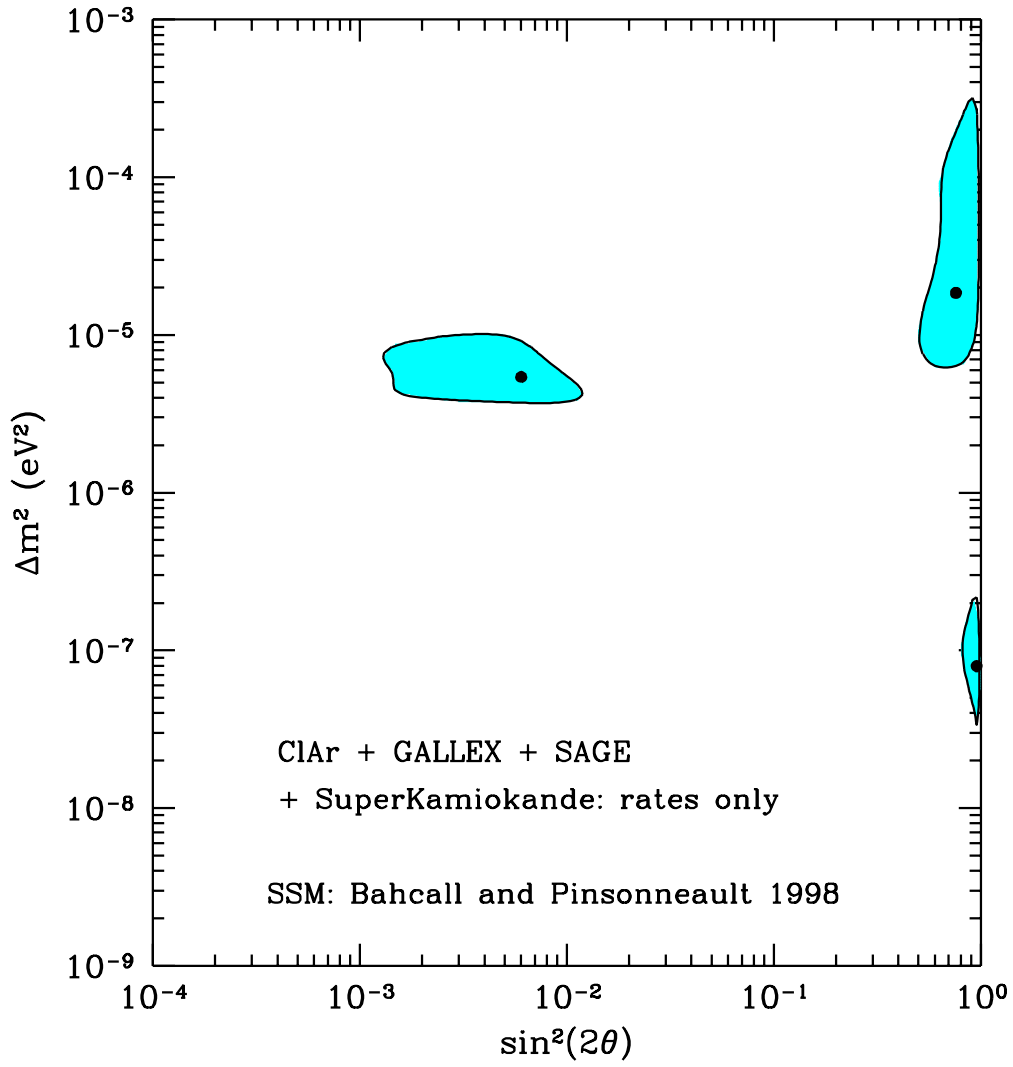


Figure I.8: From [BKS98], MSW LMA and LOW solutions: the parameter region consistent with the only total rates measured in the four experiments. Contours are drawn at 99 % C.L..

Chapter II

Borexino ...

II-A An overview of the BX design: the clue idea and the basic concepts

Borexino (BX) is a real time, high-statistics detector for low energy solar neutrinos.

The primary aim of BX is to measure the ${}^7\text{Be}$ contribution to the solar neutrino flux. BX will be the only experiment in the near future able to detect ${}^7\text{Be}$ neutrinos and to discriminate them from the other components of the solar neutrinos flux.

The Primary Aim

BX is sensitive to all leptonic flavours neutrinos but it is unable to distinguish electron from other flavours neutrinos. Indeed both charged and neutral currents contribute to the amplitude of the basic reaction: the elastic electroweak scattering $\nu_x + e^- \rightarrow \nu_x + e^-$. The cross section for the reaction is $\sim 10^{-44} \text{ cm}^2$ for 0.5 MeV ν_e (see references [tH71, Bah89]) and it is 4.5 times lower for other flavour neutrinos at the same energy. BX will measure directly the recoil energy spectrum of the electrons scattered by neutrinos.

The Basic Reaction

The active part of the detector is an unsegmented volume of 300 tons of liquid scintillator, the inner 100 tons serving as fiducial volume. The scintillation light produced by the scattered electrons is observed by means of 2200 photomultiplier tubes (PMTs). The choice of a high yield organic liquid scintillator allows a low hardware energy threshold of a few tens of KeV. On the other hand, the contamination of the scintillator in the low energy β^- emitter ${}^{14}\text{C}$ ($Q = 156 \text{ KeV}$) fixes the anticipated software energy threshold at 250 KeV.

The Basic Processes

The counting rate for neutrinos in the fiducial volume and above the software energy threshold is 58 events/day (42 from ${}^7\text{Be}$ neutrinos) at the BBP 98 SSM intensity. The counting rate per unit mass is 0.5 events/(day·ton). In BX there is no event-by-event signature for ν -e scattering events or directional information, hence the signal can be distinguished from the background only statistically. There is however a spectral signature: owing to the monochromatic nature of the ${}^7\text{Be}$ neutrino radiation, the neutrino energy spectrum features a sharp “Compton like” edge at the energy of 665 KeV. There is also a temporal signature: a $\pm 3.5 \%$ annual variation of the flux is expected owing to the variation of the earth-sun distance.

The Signal and Its Signatures

The lack of event-by-event signatures makes critically important a low background counting rate, and more, a good understanding of the energy dependence of the background. The BX project's requirement for the background in the energy range 250–800 KeV (which will be referred to as the “Neutrino Window” (NW)) is an upper limit of 0.05 events/(day·ton), or, if you prefer, $5 \times 10^{-10} \text{ Bq/Kg}$.

The Background and Its Classification

The clue of the experiment is the idea that it is possible to reach such a low background employing as active part a large ($\sim 300 \text{ m}^3$) unsegmented volume of organic liquid scintillator. The background sources have been classified into three different classes. The following paragraphs describe the background classes and the strategy to minimize the corresponding counting rates.

Internal bckgd. It is radiation from radioactive nuclides contained in the active part of the detector, the scintillator.

Internal background may consist of natural radioactivity and of long or short living cosmogenic radioactivity.

Natural radioactivity is due to the presence in nature of its very long ($10^9 \text{ y} < \tau$) living carrier nuclides, to say ${}^{238}\text{U}$, ${}^{232}\text{Th}$ and ${}^{40}\text{K}$. An organic liquid scintillator is likely to have very low levels of natural radioactivity, because the abovementioned carrier nuclides typically exist as ions and are hence insoluble in non-polar organic solvents. If they are present in form of non-organic complexes, it may be possible to separate them from the scintillator.

Since the liquid scintillator is synthesized from petroleum which has resided deep underground for million of years, the long ($10\text{ y} < \tau < 10^7\text{ y}$) living cosmogenic radioactivity initially present will have decayed away. Still, short ($1\text{ d} < \tau < 10\text{ y}$) living cosmogenic radioactivity may have been produced in the time interval since the extraction of the petroleum up to the underground storage of the scintillator. In this case it may still be possible to purify the scintillator. In the context, it is very relevant the case of the ^7Be nuclide. This radioactive nuclide is cosmogenically-produced by the reactions: $^{12}\text{C}(n,\alpha nn)^7\text{Be}$ and $^{12}\text{C}(p,\alpha pn)^7\text{Be}$. ^7Be decays by electron capture with a meanlife of 76 days feeding with 10 % branching ratio an extremely tedious 478 KeV γ -ray. A dedicated study has shown that ^7Be is efficiently removed from the scintillator by distillation [V⁺96]. In order to contend with this source of background, after the initial distillation of the scintillator in its production stage, rapid transport of it to the underground site followed by on-site distillation and underground storage is planned.

External bckgd. It is radiation from radioactive nuclides located in the detector constructing materials and in the rocks surrounding the detector.

The external background may be kept to a minimum designing the detector with a spherical geometry and an onion-like structure, where several concentric shielding layers surround a vessel filled with the scintillator. In this design, the radiopurity requirements for the constructing materials are more and more stringent as closer is their position with respect to the scintillator and larger their masses. The choice of the dimension of the shells and of the materials and the radiopurity level of the layers follows the basic concept that the background produced by each layer cannot exceed the background induced in its position by more external sources.

In the choice of the detector's constructing materials, the analysis of the intrinsic radioactive contamination of a wide spectrum of candidate materials performed with ^{76}Ge solid state detectors has played a major role [Lau93, G⁺97].

Cosmic bckgd. It is cosmic-rays and very short ($\tau < 1\text{ d}$) living radioactive nuclides produced in the detector by cosmic rays interactions.

Radiation from cosmic rays is dramatically suppressed by locating the detector underground. For this reason the detector is installed in the underground "Laboratori Nazionali del Gran Sasso", under 1400 m of rocks which provides a shielding against cosmic-rays of 4000 mwe and suppresses their flux by a factor of about 10^6 . The remaining flux of cosmic rays ($1/(\text{m}^2 \cdot \text{h})$) is composed essentially of ultrarelativistic muons with energies of the order of some hundreds of GeV.

A muon passing through the scintillator will produce a large amount of scintillation photons and can be identified unmistakably. A fraction of the muons, though, cross the detector without entering the scintillator. They could produce few enough photons (Čerenkov or weak scintillation of the buffer) to resemble a low-energy electron. To reject this source of background, a Muon Veto has been added.

The background from very short living radioactive nuclides produced by cosmic-ray inelastic interactions is not a problem for the design requirements, which concerns only the background in the NW. However, at energies higher than 1.5 MeV it constitutes one of the predominant sources (of background). In order to achieve a good understanding of the overall energy dependance of the background, it is important to keep this source under control. A dedicated study has established that a the time-space correlation between muon tracks enetring the scintillator and candidate neutrino events rejects background from short living radioactive nuclides down to the desired values.

Radon bckgd. The Rn forms a peculiar class of Background.

Rn is a noble gas and has a very high mobility. It is soluble in water and in organic liquid scintillators, and it can diffuse through plastics. The ^{222}Rn has the longest meanlife (5.51 d) between the Rn isotopes belonging to the natural radioactive chains. In case of natural radioactive contaminations contained in the detector's construction material, ^{222}Rn can emanate from the materials and it can accumulate into the buffer liquids up to relatively high concentrations. Therefore ^{222}Rn dissolved in the scintillator can give rise to internal background while γ -rays from ^{222}Rn daughter nuclides in the proximity (but outside of the scintillator) are a source of external background.

In the Counting Test Facility (CTF) of BX it was found that the dominant external γ background was due to an unexpectedly high ^{222}Rn level in the water outside the scintillator vessel (see chapter III for a discussion of CTF and section IV-C.2 for a discussion of the ^{222}Rn background in CTF). The ^{222}Rn concentration in water was found to be about 30 mBq/m^3 (the target value was of 1 mBq/m^3) and very likely it was due to emanation from the constructing materials. Although ^{222}Rn background is a

less severe problem in BX than in CTF (due to the presence in BX of a layer of scintillator acting as an active shield and enclosing a buffer defined as fiducial volume), the CTF experience has influenced the design of the BX detector inspiring the introduction of a nylon film barrier for the ^{222}Rn emanated from the constructing materials.

The remaining sections of this chapter consist of a detailed description of the experiment.

For a full introduction to the experiment, reference is made to the original proposals [BR⁺92, BC⁺93, Deu96] and their addenda [Bor95, Bor96, BC⁺96, Bor97], from where inspiration has been taken for the following description and any data reported or figure included here has been extracted, unless otherwise quoted.

II-B The structure of the detector

Borexino is composed of several concentric regions delimited by the three shells described below. The detector structure directly arises from the background requirements and it is pictured in figure II.1.

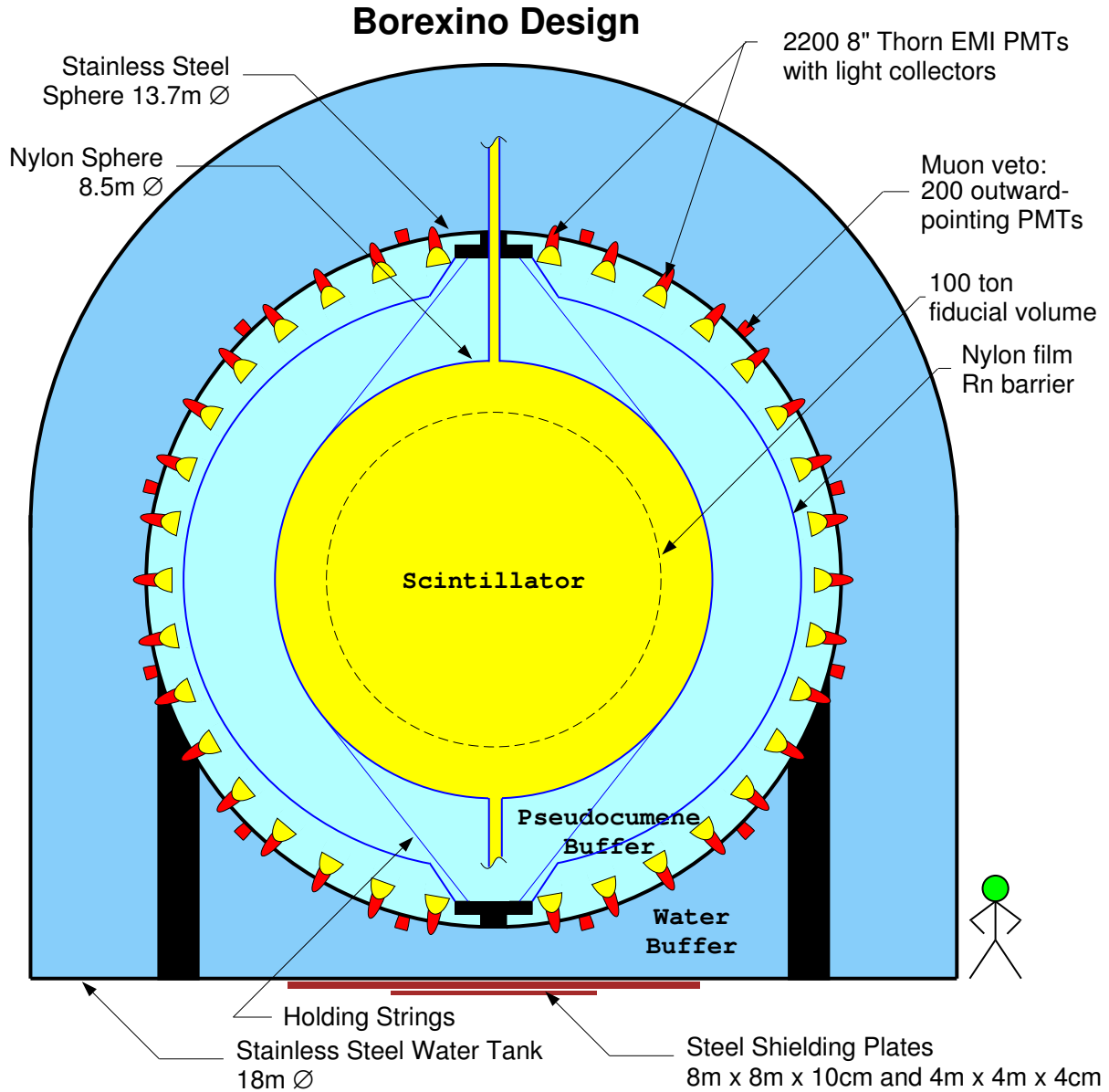


Figure II.1: A schematic view of Borexino.

Table II.1: Local γ background in the LNGS underground Halls.

Isotope	Energy (MeV)	Flux ($\text{m}^{-2} \cdot \text{d}^{-1}$)
^{228}Ac	0.911	0.5×10^7
^{214}Bi	1.120	1.4×10^7
^{40}K	1.460	3.8×10^7
^{214}Bi	1.764	1.7×10^7
^{208}Tl	2.614	1.4×10^7

Table II.2: Local neutron background in the LNGS underground Halls (From ref. [B⁺89]).

Energy (KeV)	Flux ($10^{-6} \text{ cm}^{-2}\text{s}^{-1}$)
$0-5 \times 10^{-5}$	1.08 ± 0.02
$5 \times 10^{-5}-1$	1.84 ± 0.20
$1-2.5 \times 10^3$	0.54 ± 0.01
$(2.5-5) \times 10^3$	0.27 ± 0.14
$(5-10) \times 10^3$	0.05 ± 0.01
$(10-15) \times 10^3$	$(0.6 \pm 0.2) \times 10^{-3}$
$(15-25) \times 10^3$	$(0.5 \pm 0.3) \times 10^{-6}$

The outer shell is the Water Tank (WT).

It contains ultrapure water as a shielding and a Čerenkov radiator for cosmic rays.

The intermediate shell is the Stainless Steel Sphere (SSS).

The SSS contains, as a buffer liquid, the solvent of the scintillator solution.

On the outside surface of the SSS 200 PMTs for the Muon Veto are installed. They detect Čerenkov photons produced by muons in the water. On the inside surface of the SSS 2200 PMTs are installed. They detect the scintillation light coming from the inner vessel.

Within the sphere, close to the PMTs, a nylon film Rn Barrier is installed.

The inner shell is a nylon spherical bag called also the Inner Vessel (IV).

It contains the scintillator.

The inner 100 tons of scintillator are defined as the fiducial mass.

In the following subsections the single parts of the detector will be presented in detail, with evidence on their relation to the background.

II-B.1 The outer water tank.

The external tank of Borexino is a stainless steel tank in the shape of a domed cylinder 8 m in diameter and a maximum height of 16.9 m.

The space between the outer water tank and the SSS is filled with ultra-purified water serving as a first shield against local background originating by radioactive nuclides (and cosmic rays interactions) in the Gran Sasso rocks. The composition of the local room γ and neutron fluxes are summarized respectively in tables II.1 and II.2. The reduction factor for the 2.6 MeV γ -rays from ^{208}Tl is ~ 100 per meter of water. A careful appraisal of the backgrounds has demonstrated that 2 m of water, in addition to the buffer liquid and to the scintillator buffer, are sufficient. The water shielding is at least 2 m thick except at the very bottom, where it is only 1 m. Extra shielding at the bottom is provided by steel base plates having a thickness of 0.14 m and a water equivalent thickness of 1 m, so to provide 2 m of water equivalent thickness in any direction.

In order to increase the cosmic rays detection efficiency, the water tank internal wall is covered by tyvek sheets which reflect and diffuse the Čerenkov light irradiated by the cosmic rays crossing the water.

Table II.3: Radiopurity requests for water in Borexino and in the Counting Test Facility compared to the output of the Water Purification Plant.

	$^{238}\text{U}, ^{232}\text{Th}$ [g/g]	$^{\text{nat}}\text{K}^\dagger$ [g/g]	^{222}Rn [Bq/m ³]
Borexino	10^{-10}	10^{-7}	1
CTF	10^{-13}	10^{-10}	10^{-3}
Raw Gran Sasso water	10^{-10}	10^{-7}	10^4
WPP output	3×10^{-14}	$< 5 \times 10^{-11}$	$< 3 \times 10^{-3}$

II-B.2 The Water Buffer.

Beyond its use as a shield and as a Čerenkov radiator, the ultra-purified water is employed in the scintillator purification process (water extraction, see section II-B.8) and in cleaning all the detector's equipments (cables, PMTs, etc.) before their installation in the SSS.

The radiopurity requirements for BX are less stringent than those for CTF because in CTF the water was in direct contact with the inner vessel (see section III-B). These requirements are summarized and compared to the plant's output in table II.3.

Ultra-purified is produced on-site from water coming from the Gran Sasso mountain by the Water Purification Plant (WPP) [B⁺96], described in the subsection II-B.3.

II-B.3 The Water Purification Plant

The Water Purification Plant (WPP) has already been built and it has been in use for the CTF experiment. A full description of the plant can be found in reference [B⁺96].

The WPP is composed by several units running in series. The water is processed through the following steps, listed in order from the input to the output of the plant:

- reverse osmosis unit;
- continuous deionizer unit;
- ultrafiltration unit;
- ion exchanger unit;
- two N₂ countercurrent stripping units.

the nitrogen stripping is the most critical step since the raw Gran Sasso water has a high ^{222}Rn content.

The water system is constructed principally of PVC and teflon coated steel.

The plant can purify 2 m³/h in two different modes: in the production mode it purifies the raw Gran Sasso water; in the recirculation mode, it takes water from the already filled water tank, repurifies it and refills the tank.

II-B.4 The Stainless Steel Sphere

The diameter of the SSS is 13.7 m.

The sphere serves as a part of the scintillator containment system and as support structure for the PMTs.

The space between the SSS and the IV is filled with the solvent of the scintillator solution whose density is 0.87 g/cm³. The choice of having as buffer liquid the solvent of the scintillator allows to keep both the nylon film Rn barrier and the IV free of mechanical stresses. All the stresses due to the difference in density between water and scintillator solvent are located on the SSS.

The design for the sphere was based on the requirement that it be safe in a filled, free-standing mode (full gravity load) and also be safe in the normal operating mode with water outside (buoyancy load due to the difference in density between solvent and water. Total buoyant force: 1.7×10^9 N). The sphere is made of 8 mm thick plates in the top hemisphere and 10 mm thick plates in the bottom hemisphere. Its total mass is ~ 45 tons. It is supported by 20 legs which are welded on the base plate of the water tank.

[†] $^{\text{nat}}\text{K}$ indicates natural potassium's composition. The relative abundance $^{40}\text{K}/^{\text{nat}}\text{K}$ is of about 10^{-4} . Here and in the following we will often quote the ^{40}K contamination referring to the $^{\text{nat}}\text{K}$ content because the physical quantity which is very often directly measured is the $^{\text{nat}}\text{K}$ content.

During the installation, the air within the sphere will be filtered to provide clean-room conditions. During the final installation of the nylon vessels, special synthetic Rn-free air will be pumped into the SSS to prevent build-up of Rn daughters on the nylon vessels. To assure a high level of cleanliness, especially from particulate, the inside surface of the SSS will be electropolished and then thoroughly washed during and after the installation phase.

II-B.5 The Buffer Liquid

The space between the SSS and the IV will be filled with 1000 m³ of buffer liquid. The liquid is pseudocumene (PC, 1, 2, 4-trimethylbenzene, C₆H₃(CH₃)₃) which will serve also as solvent of the scintillator solution.

The characteristics of the PC allow to meet all the requirements for the BX buffer liquid.

The density of buffer matched to the scintillator within 1 part in 10³.

The index of refraction matched to the scintillator within 1 %.

The light attenuation length and the scattering mean free path length exceed 5 m at the scintillation light wavelength (430 nm).

The limits on the radiopurity are of 10⁻¹⁵ g/g for ²³⁸U and ²³²Th (see table II.5 for a review of the radiopurity requirements for the buffer liquid. See chapters IV and V for the results of CTF on PC and scintillator radiopurity).

The pure PC (without fluors) has a scintillation light yield ~ 20 times lower than the scintillator solution. Even with this small light yield, due to the big flux of high energy γ -rays coming into the buffer liquid mainly from the glass of the PMTs (see section II-C.2), scintillation events in the buffer produce a high primary acquisition rate in the NW. The probability to misunderstand scintillation events produced in the buffer as scintillation events coming from the fiducial volume is negligible due to the possibility to reconstruct the position of the events with a good resolution. However, in order to suppress the primary acquisition rate in the NW values it is planned to add as quencher to the buffer dimethylphtalate (DMP) with a concentration of 5 g/l. The quencher offers a further suppression of the scintillation light light yield in the buffer by a factor of about 10. The light mean free path lengths and the Čerenkov light emission yield (important for the muon veto) are not affected by the presence of DMP.

II-B.6 The nylon scintillator vessel or Inner Vessel

The Inner Vessel is a spherical nylon bag 8.5 m in diameter made of a nylon film.

The material of the Inner Vessel must meet stringent requirements on cleanliness, radioactive impurities, optical clarity, chemical resistance to the solvent and to the scintillator. In particular, since it is the only material which is in direct contact with the scintillator, it must satisfy stringent limits on radiopurity (see the review of the radioimpurity requirements in table II.5). It should be noted that the ²³⁸U content (or more exactly the ²²⁶Ra content, due to possible non-equilibrium of the ²³⁸U chain) is a critical background issue. The daughter isotope ²²²Rn is a gas and can emanate from the inner vessel into the scintillator. For a concentration of ²³⁸U of 1 × 10⁻¹² g/g in the inner vessel, the ²²²Rn emanation would give rise to an equivalent intrinsic contamination of the scintillator in ²³⁸U of 1 × 10⁻¹⁷ g/g (see chapter IV for a review of the background from ²²²Rn emanation from the inner vessel).

Selection and testing of various materials led to the use of a nylon-6 film 125 μ m thick.

II-B.7 The Scintillator

The scintillator solution used in BX has been studied in laboratory experiments and it has been tested in the large scale detector CTF (see chapter V for a summary of the main results of CTF on the scintillator; see reference [A⁺98a] for a complete discussion of these results).

The scintillator consists of a solution with PC as solvent, containing as a solute the fluor PPO (2,5-diphenyloxazole, C₁₅H₁₁NO) in concentration of 1.5 g/l.

The characteristics of the scintillator solution as measured in CTF or in laboratory allow to meet all the BX requirements for the scintillator.

The solution has a high primary light yield amounting to about 10⁵ photons/MeV.

The wavelength at the peak emission is located at 430 nm, well above the sensitivity threshold of the PMTs which is about 350 nm.

At the peak emission wavelength the solution has long light mean free path length exceeding 7 m.

The scintillation decay lifetime does not exceed 4 ns as it is necessary to obtain a good spatial resolution.

The large difference on the tail of the decay time distributions for α and β excitation modes allows a very efficient α/β discrimination as it was proved in laboratory experiments and also in CTF (see section V-A for a review of the CTF results on the α/β discrimination).

The α -quenching factor exceeds 10 in the energy range 5–6 MeV, constraining the β -equivalent energies for most of the ^{238}U chain α decays below 0.5 MeV and hence out of the range of the “Compton-like” ^7Be edge. The α -quenching as a function of the energy has been measured in laboratory [Nef96] and it is $Q(E) = 20.3 - E \cdot 1.3 \text{ MeV}^{-1}$.

There are no major impediments to satisfy on the large scale mass the very stringent limits on the radiopurity of 10^{-16} g/g of ^{238}U and ^{232}Th as it was proved in CTF (see chapters IV and V for the results of CTF on PC and scintillator radiopurity).

It is worthwhile to spend here more words on the principles of the α quenching and of the α/β discrimination in organic scintillators (a very detailed discussion of this topic can be found in reference [Bir74]).

In organic scintillators the fluorescence light is emitted in radiative transitions from the first excited state for a π electron orbital singlet state S_1 to the ground state S_0 (a singlet) or to the vibrationally excited sub-levels of the ground state. The typical radiative time of the π -singlet state S_1 is of the order of 10^{-9} – 10^{-8} s .

Population of the excited triplet states provoked by a moving charged particle may result in a slow scintillation component. The slow scintillation component is due to collisional interactions of molecules in the lowest excited π -triplet state T_1 giving rise to a molecule in the first excited π -singlet state S_1 and to a molecule in the ground state S_0 . The lifetime of the delayed emission is determined by the lifetime of T_1 and the rate of collisions between T_1 excited molecules, and it is longer than the radiative time of the π -singlet state S_1 . The spectrum of the slow scintillation components does not differ from the spectrum of the main component, since in both cases the light is emitted only in the S_1 - S_0 radiative transition. But the decay time of the slow scintillation component is significantly longer and for some scintillators can reach the values of $1 \mu\text{s}$.

Scintillation light quenching may results from molecular interactions between the excited π -states and other excited or ionized molecules. Quenching depends on the density of excitons and ionized molecules, resulting in a non-linear relationships between energy deposition and scintillation light emission. Quenching is bigger for α particles than for electrons owing to the greater energy loss per unit length of α particles.

The relative intensities of the fast and the slow scintillation components depend on the energy loss per unit length, since the slow scintillation component is less effected by quenching. This dependence results in a relative intensity for the slow emission which is bigger for α than for β particles, allowing the discrimination of the two radiations on the basis of the decay time distribution.

The distribution of the scintillation decay time is usually described phenomenologically by a sum of exponentials where the exponential with the shortest meanlife corresponds to the main scintillation component:

$$\begin{aligned} \sum_i q_i &= 1 \\ f(t) &= \sum_i \frac{q_i}{\tau_i} e^{-t/\tau_i} \end{aligned} \tag{II.1}$$

Table II.4 reports the parameters for the scintillator decay time distribution in the case of β - γ or α radiation as measured in laboratory on small scale samples of the BX scintillator [RGL98]. Figure II.2 shows the scintillator decay time distribution measured in laboratory for α and β particles. The possibility to discriminate between β - γ and α radiation is based on the difference in the tail of the time distributions of scintillator decay.

II-B.8 The Scintillator Purification System

The system is composed by four different units. A complex fluid-handling system can manage the scintillator in order to purify it through one single unit as well as through several of them in series. The units are intended for pre-filling purification of the scintillator as well as online purification of the scintillator and, if needed, of the buffer.

The units are:

- N_2 counter-current stripping column;

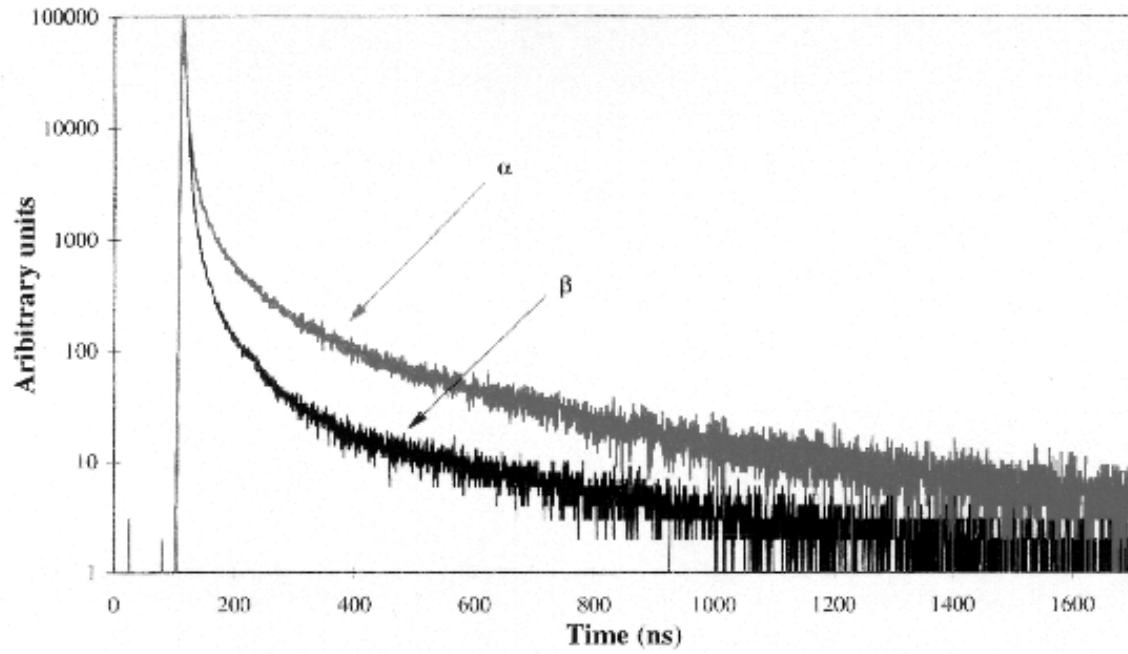


Figure II.2: Time decay distribution of the scintillator for emission excited by α or β - γ radiation (from laboratory measurements, see reference [RGL98]).

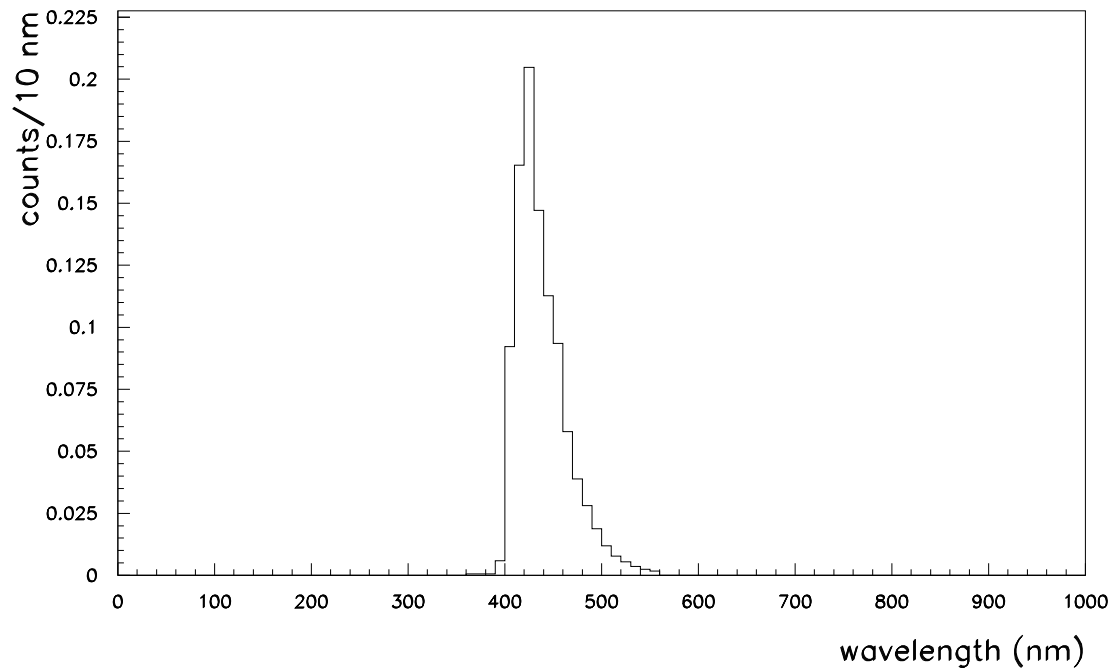


Figure II.3: Emission spectrum of the BX scintillator (from laboratory measurements, see reference [RGL98]).

Table II.4: Decay times and probabilities for the different scintillation component in case of emission excited by α or $\beta+\gamma$ radiation, as a result of laboratory measurement [RGL98].

	1st component		2nd component		3rd component	
	τ_1 [ns]	q_1 [%]	τ_2 [ns]	q_2 [%]	τ_3 [ns]	q_3 [%]
β - γ rays	1.71	88.17	10.46	10.73	83	1.10
α rays	2.30	58.36	15.15	25.84	100	15.80

- water extraction unit;
- distillation unit;
- silica gel filtration column.

Filtration removes suspended dust particles larger than $50\text{ }\mu\text{m}$. Nitrogen stripping removes dissolved gas impurities. Water extraction is effective at removing ionizable species, such as metals (U, Th, and K). Vacuum distillation removes low volatility components such as metals and dust particles.

II-B.9 The detection of light

The scintillation light from a neutrino interaction in the scintillator vessel will be detected by an array of 2200 photomultiplier tubes (PMTs) mounted on the inside surface of the SSS.

The PMTs are the 20 cm diameter Thorn-EMI 9351. The sensitivity threshold of the PMTs is at 350 nm and the peak of the quantum efficiency is at 420 nm, as it is shown in figure II.4). The transit time spread is of 1 ns, the dark noise rate is of the order of 1 KHz, the afterpulsing is roughly 2.5 % and the amplification is 10^7 at the working voltage of 1400 V.

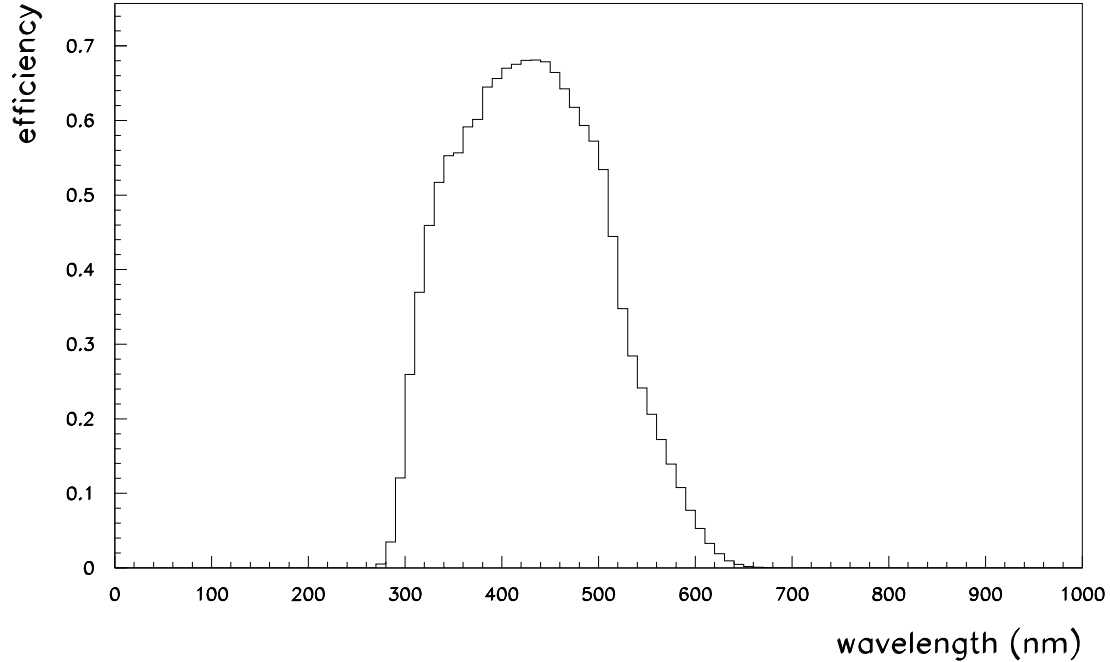


Figure II.4: Quantum efficiency of the PMTs.

Due to the radioactive contaminants contained copiously in the cathode glass, the PMTs are necessarily the only exception to the basic design concept that the background produced by each material layer cannot exceed the background induced in its position by more external sources (see section II-A). Hence they are the major source of external background in the NW (see section II-C.2). In order to minimize this background source, they are produced with the special low radioactivity glass Schott 8346.

A special directional light concentrator, similar to the “Winston cone” [WW89], is mounted on 1800 PMTs, thereby restricting the field of view to the IV and increasing the efficiency for detecting the light from the scintillator region by a factor of about three. The cones have a length of 28 cm and a maximum diameter of 35 cm.

The remaining 400 PMTs will be equipped with cylindrical light guides having the same length of the directional light concentrators and having the diameter of the PMTs cathode. These guides have a wider solid angle acceptance (2π steradians) in order to detect also Čerenkov photons produced in the buffer by the muons (see also section II-C.3). The wider solid angle acceptance is compensated by a reduced efficiency in detecting scintillation photons from the scintillator.

For scintillation light produced in the inner vessel, the effective photocathode area covered by the 2200 PMTs coupled to their light guides is of about 35 %.

Beside the 400 PMTs with the cylindrical light guides, the muon detector will use also an external detector consisting of an array of 200 PMTs mounted on the outside surface of the SSS. These PMTs are to detect the Čerenkov light produced in the 2 m of water between the outer tank and the sphere. The 200 PMTs are of the same model as the other 2200, but they are not coupled to light guides in order to obtain a wider solid angle acceptance.

II-B.10 The electronics and the data acquisition

The electronics for Borexino were designed for the following capabilities:

- To compile an energy measurement of a scintillation event by recording the pulse height for all the hit PMTs, including multiple hits on the same PMT.

- To measure the arrival times of the first photon hitting each PMT, allowing the reconstruction of the space-temporal position of the event and of the scintillation decay time distribution (important for the α/β discrimination);

- To record multiple sequences of events with delay times as short as 100 ns (these sequences are called also delayed coincidences in the forthcoming discussion of the background in section II-C.2);

- To include a fully-programmable trigger processor that allows various general PMTs hit requirements to be set.

The electronics for BX will be constructed from custom modules designed by collaborators and is fabricated by a commercial electronics manufacturer.

II-C The performance of BX

II-C.1 The signal

The counting rate for ^7Be neutrinos in the neutrino window and in the fiducial mass is of 42 events/day in the hypothesis of the flux predicted by the BBP 98 SSM. However, it is reasonable to expect a lower flux of ^7Be neutrinos than specified by the SSM. The combination of the observations on solar neutrinos and on solar luminosity impose a severe limit on the possible flux of ^7Be neutrinos (see reference [BKS98] or section I-C.2). Moreover, the solutions to the Solar Neutrino Problem in terms of neutrino oscillation would provide a substantial reduction of the flux measured by BX due to flavour conversion. Figure II.5 shows the expected rates in BX for the most interesting oscillation scenarios.

It is important that the BX experiment were able not only to measure the ^7Be flux at the SSM rate but also to set a low upper limit on its possible flux. Therefore, owing to the weak spectral signature, it is essential to achieve a low background, possibly not higher than one tenth of the signal expected in the SSM hypothesis.

II-C.2 The background

External background

By external background, we refer to any γ -ray emitting radioactivity external to the scintillator contained in the IV. The radioactivities to be considered include those originating from the rock walls of the laboratory (see tables II.1 and II.2) as well as those from radioactive impurities in the detector components themselves (see table II.5). The resulting background rates in the NW are reported in table II.6 and their energy spectrum is compared with the energy spectrum of the neutrino signal in figure II.6.

The photomultipliers contribute the most to the total external background rate.

In figure II.7 the radial distribution of the external background in the NW is plotted and compared with the same distribution for neutrino events. This figure shows the effectiveness of the fiducial volume cut in rejecting external background events. In addition to serving as the highest purity passive shielding, the outer volume of scintillator also acts as an “active veto”. Only the most energetic γ -rays can penetrate into the fiducial volume, located 1.25 m away from the surface of the nylon vessel, without interacting in the veto region first. Those that penetrate typically have more energy than the ${}^7\text{Be}$ neutrino signal. On the other hand, those that interact in the outer volume deposit energy in that region. Such an event has an energy-weighted “center-of-gravity” that is shifted to a larger radius. Thus, these backgrounds are vetoed very effectively by both the energy window and fiducial volume requirements.

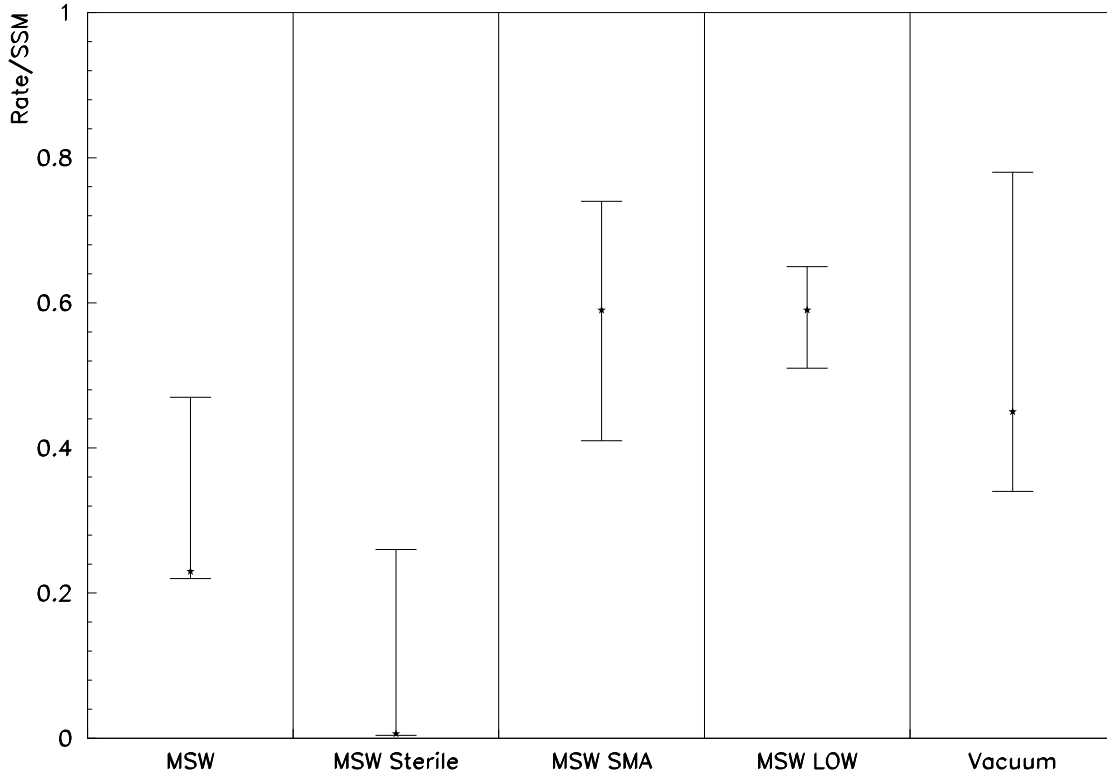


Figure II.5: The expected rates in BX for several solution to the Solar Neutrino Problem in terms of neutrino oscillations.

The rates are expressed as a fraction of the BBP 98 SSM predicted rate.

In each scenario, ranges are illustrated that represent the rates that could be observed by BX and that would be still consistent with the results of the four solar neutrino experiments. Ranges are given at 99 % C.L.. The values are taken from ref. [BKS98].

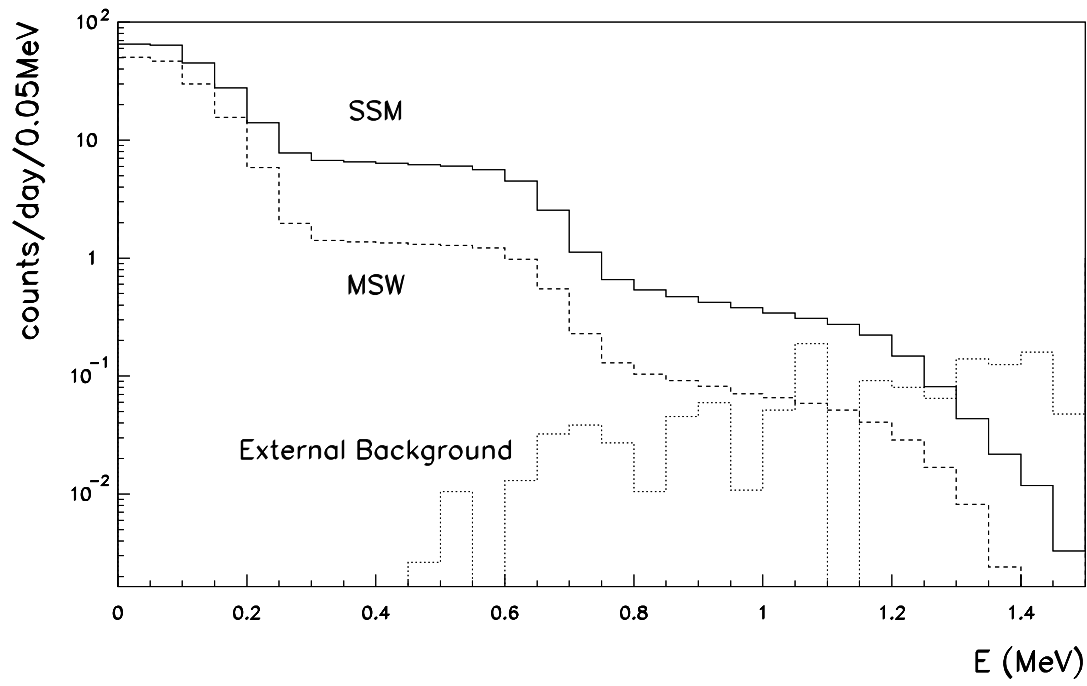


Figure II.6: Energy spectrum of external background. The spectrum is compared with the neutrino signal spectrum, in the case of the SSM and MSW scenarios.

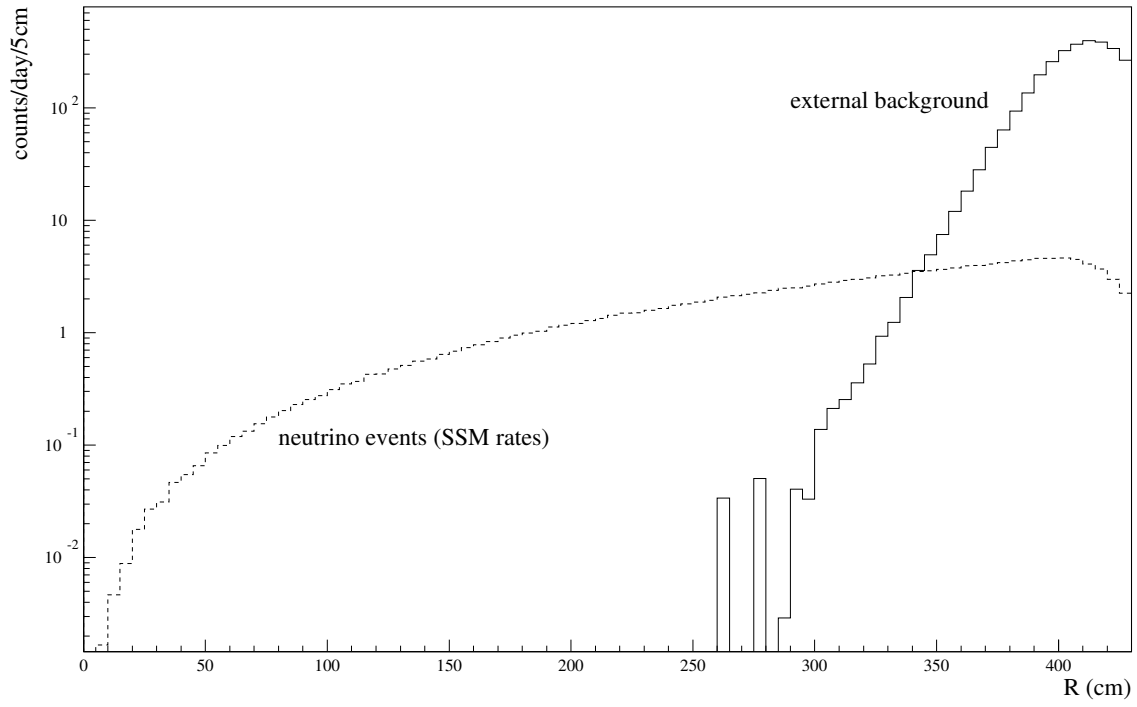


Figure II.7: Radial distribution of the external background events in the neutrino window. The distribution is compared with that of neutrino signal. Infinite spatial resolution is assumed.

Table II.5: Radioactive impurity levels in the Borexino materials

Component	^{238}U (g/g)	^{232}Th (g/g)	$^{\text{nat}}\text{K}$ (g/g)	total mass (g)
2000 PMTs	3×10^{-8}	1×10^{-8}	2×10^{-5}	8×10^6
Pseudocumene Buffer	1×10^{-15}	1×10^{-15}	5×10^{-12}	8.7×10^8
Nylon bag	2×10^{-11}	2×10^{-11}	1×10^{-8}	5×10^4
Light guides	2×10^{-10}	1×10^{-9}	3×10^{-7}	6×10^6
Stainless Steel Sphere	2×10^{-10}	1×10^{-9}	3×10^{-7}	3.7×10^7
Cables	2.1×10^{-8}	2.4×10^{-8}	7×10^{-6}	2×10^5
^{222}Rn in the Pseudocumene Buffer: dissolved at the level of 1 mBq/m ³ in 1000 m ³ of buffer				

Table II.6: Expected external γ background rates (events/day in a 100 tons fiducial volume) in the neutrino window according to the different sources. Infinite energy resolution assumed.

Component	250–800 KeV
	Rate induced [events/day]
PMTs	0.06
^{222}Rn in buffer	0.03
Pseudocumene buffer	< 0.004
Nylon	< 0.04
Light guides	0.01
Stainless Steel Sphere	< 0.007
Rock	< 0.005
Cables	< 0.003
Total	0.11
Error	± 0.05

Internal background

The internal sources of background are the most critical concern in BX. In fact, though there are some cuts in the analysis that reject some of the internal background counts, in principle the internal radioactivity can only be reduced by purification.

From the CTF measurements (see chapters IV and V), the concentration of the metal impurities is expected for ^{238}U and ^{232}Th to be at or below 10^{-16} g/g, and for $^{\text{nat}}\text{K}$ to be below 10^{-14} g/g. The concentration of ^{14}C relative to the ^{12}C is expected to be at 10^{-18} .

Estimate of the internal background rates and spectra in BX were made using the CTF values.

Since organic liquid scintillators are predominantly composed of carbon, the intrinsic concentration of the radioisotope ^{14}C can constitute the main background at low energies. ^{14}C decays emitting a β^- -ray, with a 156 KeV maximum kinetic energy and a 8266 years meanlife. At the contamination level of 10^{-18} for the ratio $^{14}\text{C}/^{12}\text{C}$ the expected number of counts due to ^{14}C in the NW is 0.1 counts/day and it is negligible.

Table II.7 lists the contribution from each source of internal background showing all the daughter isotopes in the ^{238}U and ^{232}Th chain individually. The raw background rate comes mostly from the α activity from the two chains. It must be stressed that in liquid scintillator the light output for α particles is quenched by a factor of about 10.

In the data analysis, three cuts will be used to reject some of the internal background counts.

The first is the tagging of delayed coincidences (DC) in the two chains. The decays of a father and daughter isotopes in a radioactive chain are separated by the decay time of the second isotope. If the meanlife of the second isotope is much shorter than the inverse of the random background rate (for the signal given by the decay of the daughter) the sequence can be tagged very effectively by means of the only delay time. The complementary use of energy cuts may be helpful in increasing the signal/noise ratio. A complete discussion of the delayed coincidence tag and of its role in the CTF analysis will be presented in chapter IV.

Isotopes decaying emitting an high energy α particle can have very short meanlives. The sequences taggable by the DC cut are two β - α sequences (^{238}U chain, ^{214}Bi - ^{214}Po , $\tau=236 \mu\text{s}$; ^{232}Th chain, ^{212}Bi - ^{212}Po , $\tau=432 \text{ ns}$) and one α - α sequence (^{232}Th chain, ^{220}Rn - ^{216}Po , $\tau=216\text{ms}$).

Table II.7: Internal background estimate (events/day in a 100 tons fiducial volume) after successive cut analysis. The following contaminations are assumed: ^{238}U : 10^{-16} g/g at the chain equilibrium; ^{232}Th : 10^{-16} g/g at the chain equilibrium; $^{\text{nat}}\text{K}$: 10^{-14} g/g. Infinite spatial and energy resolution are also assumed.

Chain	Isotope	250–800 KeV			
		raw	DC (95%)	PSD (90%)	SS (95%)
$\beta+\gamma$: ^{238}U	^{234}Th	0	0	0	0
	^{234}Pa	3.9	3.9	3.9	3.9
	^{214}Pb	9.3	9.3	9.3	0.5
	^{214}Bi	0.5	0.02	0.02	0.02
	^{210}Pb	0	0	0	0
	^{210}Bi	6.4	6.4	6.4	6.4
^{232}Th	^{228}Ra	0	0	0	0
	^{228}Ac	0.3	0.3	0.3	0.3
	^{212}Pb	3.1	3.1	3.1	0.2
	^{212}Bi	0.8	0.04	0.04	0.04
	^{208}Tl	0	0	0	0
	^{40}K	1.5	1.5	1.5	1.5
	total $\beta+\gamma$:	25.8	24.6	24.6	12.9
α : ^{238}U	^{238}U	10.6	10.6	1.1	1.1
	^{234}U	10.6	10.6	1.1	1.1
	^{230}Th	10.6	10.6	1.1	1.1
	^{226}Ra	10.6	10.6	1.1	1.1
	^{222}Rn	10.6	10.6	1.1	0.05
	^{218}Po	10.6	10.6	1.1	0.05
	^{214}Po	3.2	0.2	0.02	0.02
	^{210}Po	10.6	10.6	1.1	1.1
^{232}Th	^{232}Th	3.5	3.5	0.4	0.4
	^{228}Th	3.5	3.5	0.4	0.4
	^{224}Ra	3.5	3.5	0.4	0.02
	^{220}Rn	3.5	3.5	0.4	0.02
	^{216}Po	3.5	3.5	0.4	0.02
	^{212}Po	0	0	0	0
	^{212}Bi	1.3	1.3	0.1	0.01
	total α :	96.2	93.2	9.8	6.5
	total	122	118	34	19

In table II.7 it was assumed for the DC cut an efficiency of 95 % which we consider as a conservative value for the α/β discrimination.

A second cut used to identify and reject the α internal background is pulse-shape discrimination (PSD). In organic liquid scintillators, pulse shape is different between β and α scintillations: an α particle gives rise to a bigger fractional light emission in the slow scintillation component (see section II-B.7). From the laboratory and the CTF measurements (see reference [A⁺98a] and section V-A), a conservative estimate of 90 % identification probability for α events is assumed in table II.7.

The third cut in use is statistical subtraction (SS). Once tagged the sequences by DC, the number of decays in each fragment of the natural chains which is at the equilibrium on the time scale of the experiment and contains a sequence of delayed coincidences is determined with a high accuracy. The argument holds for a chain fragment that contains only short-lived isotopes and does not extends beyond very mobile isotopes. The energy spectrum resulting from the activities of these chain fragments is known and can be subtracted from the total energy spectrum. In the ^{238}U chain, tagging the ^{214}Bi - ^{214}Po sequence allows to remove the radioactivities in the chain fragment from ^{222}Rn to ^{214}Pb . In the ^{232}Th chain, tagging the ^{212}Bi - ^{212}Po sequence allows to remove the radioactivities in the chain fragment ^{224}Ra - ^{212}Pb .

The statistical subtraction can be used to remove both α and β radioactivities. However, it has not the event-by-event rejection feature of the DC and PSD cuts. It must be performed last, after sufficient statistics (total counts and tagged delayed coincidences) have been accumulated. The SS efficiency assumed in table II.7 is identical to the value assumed for the DC detection efficiency (95 %).

An estimate of the internal background spectral shape is shown in figure II.8 where all the cuts have been applied. Superimposed is the recoil-electron spectrum arising from the SSM flux of ^7Be neutrinos. Figure II.9 shows the same spectra in the energy region above the software energy threshold with a linear scale representation.

Other backgrounds

There are some other potential sources of background. They include background from muons and muon-induced spallation products, neutrons, and cosmogenic radioactivity for materials that have been exposed at the surface level. These sources of background have been evaluated and they are negligible (they contribute less than 1 events/day).

As far as the muon related background is concerned, we refer to the dedicated subsection II-C.3.

II-C.3 The Muon Detector

The design requirement for the muon detector is to reduce the muon induced background to less than 0.5 events/day in the energy range extending from the lower border of the NW (250 KeV) up to 1500 KeV. Potential background induced by cosmic rays fall into three classes:

Muons and prompt secondaries. The muon flux in the underground LNGS is $1/(\text{m}^2 \cdot \text{h})$. 4500 muons per day will cross the SSS of BX. These muons will produce scintillation light in the liquid scintillator and/or Čerenkov light in the buffer liquid. The design value of the efficiency of the Muon Detector in rejecting these events is better than 0.9998.

γ -rays from capture of cosmogenic neutrons. Energetic neutrons are produced by ultrarelativistic muons primarily in hadronic showers, occurring with a frequency of the order of a few 10^{-2} per meter of path in water or scintillator (the production rate is known from the literature and it has also been checked in CTF, see reference [A⁺89] and section IV-E). Neutrons are thermalized by inelastic and elastic collisions and then captured by protons in the reaction:



the emitted γ -rays has an energy of 2.16 MeV. Neutrons have a capture mean time of about 300 μs in the BX scintillator. In BX 100 neutrons/day are expected, one third of them in the fiducial volume.

Virtually, all of these pulses fall outside the energy range of interest in BX. In addition, they can be completely suppressed by excluding pulses preceded by another signal within 3 ms.

Radionuclides produced by muons in the scintillator. The muon-induced nuclear cascades that produce neutrons also produce radioactive nuclei in reactions involving the carbon atoms of the scintillator. A list of cosmogenic radionuclides produced in the scintillator is reported in table II.8.

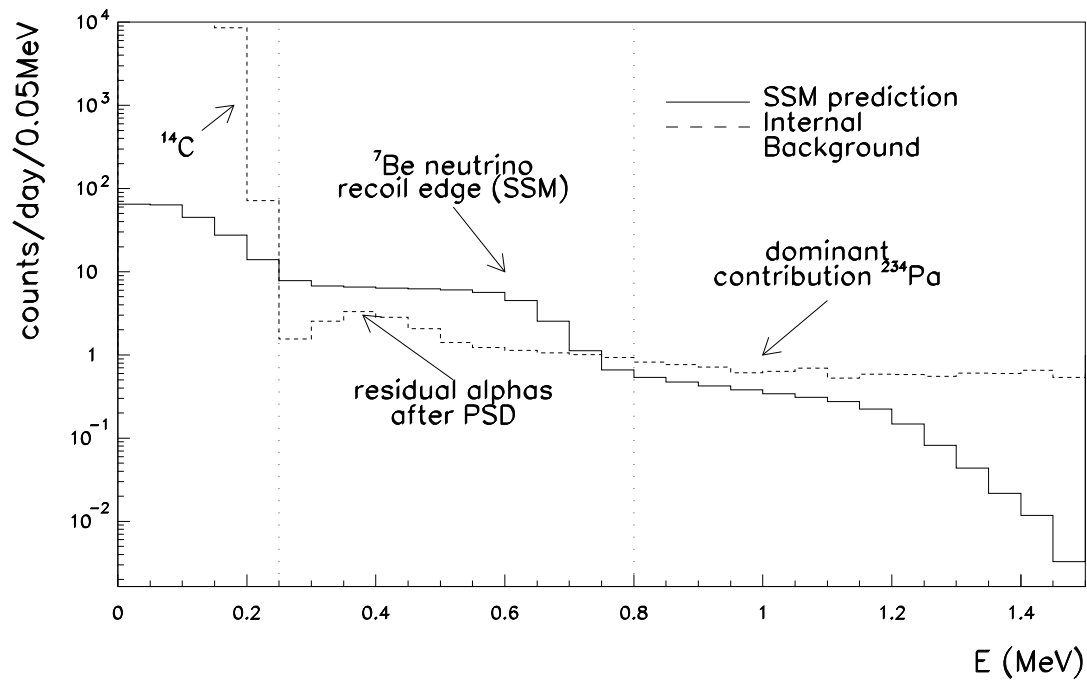


Figure II.8: Energy spectrum of the internal background. The spectrum is compared with the neutrino spectrum in the case of the flux predicted by the BBP 98 SSM.

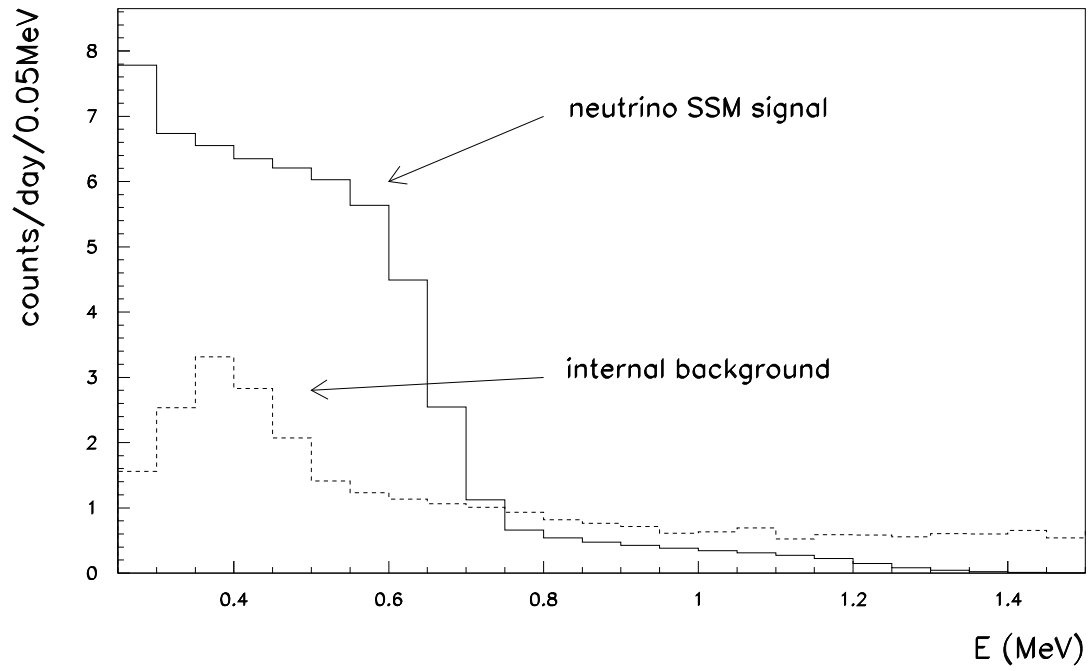


Figure II.9: Energy spectrum of the internal background. The spectrum is compared with the neutrino spectrum in the case of the flux predicted by the BBP 98 SSM in the energy region above the software energy threshold.

Table II.8: Cosmogenic radionuclides in the scintillator.

Nuclei	τ	Q [MeV]	γ -rays
β^- emitters:			
^8Li	1.21 s	13.0	
^9Li	0.26 s	13.5	
^{11}Be	19.9 s	11.4	2.0 MeV (30 %), others
^{12}B	0.03 s	13.4	4.4 MeV (1.3 %), 7.6 MeV (1.5 %)
β^+ emitters:			
^8B	1.11 s	13.7	
^9C	0.19 s	16.0	
^{11}C	29.4 m	0.96	
Electron Capture:			
^7Be	76.9 d		478 KeV (10 %)

Recently, data from an accelerator experiment [vF⁺98] gave a precise estimate of the production rate of these nuclei. The estimate for the total background rate is one third of the neutron rate, i.e. 30 events/day in the scintillator and 10 events/day in the fiducial volume.

Owing to the high endpoint energies, none of the very short lived isotopes is expected to give a background of more than 1 event/day, even without further cuts. Their contribution can still be reduced by time correlation with preceding muons.

^{11}C poses a special problem. The 30 m meanlife is too long for a time correlation with the preceding muon. Being a β^+ emitter, the decay pulses fall in the energy range 1–2 MeV (the positron-electron annihilation energy must be added to Q) and therefore outside the neutrino window. The expected rate is 6 events/day in the scintillator and 2 events/day in the fiducial volume. However, a nuclear cascade producing ^{11}C must have produced also a neutron which has been captured within 1.5 m from the place where the ^{11}C nuclide is produced and will decay later on. Restricting the search for the preceding muon to a sphere with 1.5 m radius, the rate of neutrons is 4 events/day or 0.05 events/ τ , permitting event-by-event identification.

The general objectives of the Borexino Muon Detector are:

1. to recognize each muon interaction recorded by the internal PMTs as a non point-like event interaction;
2. to detect the preceding muon event when a prompt secondary or a delayed event is recorded by the internal PMTs with an energy comparable to a relevant neutrino signal.

In order to accomplish this purpose the strategy is to use the following three cuts in series:

Borexino cut. It is the discrimination performed only by means of the internal 1800 PMTs coupled with directional light concentrators. On the basis of the CTF experience and of accurate simulations, the discrimination efficiency based on total apparent energy and spread time of photons is really high (better than 99.7 %).

Buffer cut. It is the discrimination performed only by means of the internal 400 PMTs coupled with cylindrical non-directional light guides with a wider (2π steradians) acceptance at their entrance. These PMTs detect photons coming also from the buffer region. The number of PMTs struck by the Čerenkov light produced by muons crossing only the buffer is greatly enhanced by the non-directional guides, increasing the efficiency of the discrimination.

Veto cut. It is the discrimination performed only by means of the external 200 PMTs mounted on the outside surface of the SSS. These PMTs detect the Čerenkov light produced by muons in the water. The external veto accomplishes two distinct functions: it produces a veto signal coincident with a signal recorded in BX to recognize the events as muon-induced; it produces an independent and stand-alone trigger indicating a muon event that failed in registering in the internal detector and which may have initiated a delayed event thereafter recorded by the internal detector.

The application in series of the cuts here described reduces the background under the desired value as it is shown in table II.9.

Table II.9: Cosmic ray background rates in the energy range 0.25–1.50 MeV in units of events/day after the application in series of the cuts. For delayed events, the delay time cut is included.

	Muons and prompts	Neutrons	Nuclides ($\tau < 20$ s)
Total	4500	100	30
BX cut	< 15	< 2	< 0.5
Buffer cut	< 5	< 0.1	< 0.1
Veto cut	< 0.5	< 0.05	< 0.05

II-D The Physics potential of BX

Taking into account the measurements already performed by the previous solar neutrino experiments, can BX discriminate between the most popular oscillations solutions to the solar neutrinos problem by measuring the ^7Be neutrinos flux? The answer is yes, in most of the cases.

As it was shown by Fogli et al. [FLM97] BX will be in any case able to discriminate between the VO scenario and the several allowed MSW scenarios by looking to the seasonal variations of the signals. Indeed, the parameters of the VO allowed region are such that the oscillation length is just of the order of the earth-sun distance. Once the solid angle dependence ($\propto 1/L^2$) has been exactly subtracted from the data, a yearly variation due only to oscillation as big as 25 % of the signal is expected at the best fit point as it is shown in reference [CFFL95] and in figure II.10. On the contrary, in the MSW scenario no seasonal variations other than the solid angle variation are expected. The Fourier analysis of the real time distribution of neutrino interactions (see always reference [FLM97]) has shown that in case of VO scenario BX is sensitive to the deviations in the values of the Fourier discrete transform from the no-oscillation values up to the third harmonic, as it is shown in figure II.11. Furthermore, a vanishing value for the deviation of the first harmonic corresponds to a non vanishing value for the second one, allowing BX to explore almost all of the allowed parameter region for the VO scenario. The BX sensitivity is much higher than that of other real time and high statistics experiments because it observes a neutrino source with a discrete energy spectrum. Experiments measuring the ^8B neutrino fluxes like SNO and SuperKamiokaNDE are sensitive only to the first harmonic since the average of the survival probability over the continuous energy spectrum cuts down the deviation of the Fourier coefficients from the no-oscillation values.

Moreover, as it was shown by Bahcall et al. [BKS98], BX can discriminate between the (unlikely) MSW LOW scenario and all other MSW scenarios. Indeed, in the MSW LOW scenario a big day/night asymmetry is expected for the solar neutrinos flux at energies lower than 1 MeV due to the effect of regeneration in the earth, as it is shown in figure II.12.

Finally, the MSW (small mixing angle), the MSW Sterile and the MSW LMA scenarios can be disentangled in most of the cases (but not in all of) on the only basis of the total rate detected.

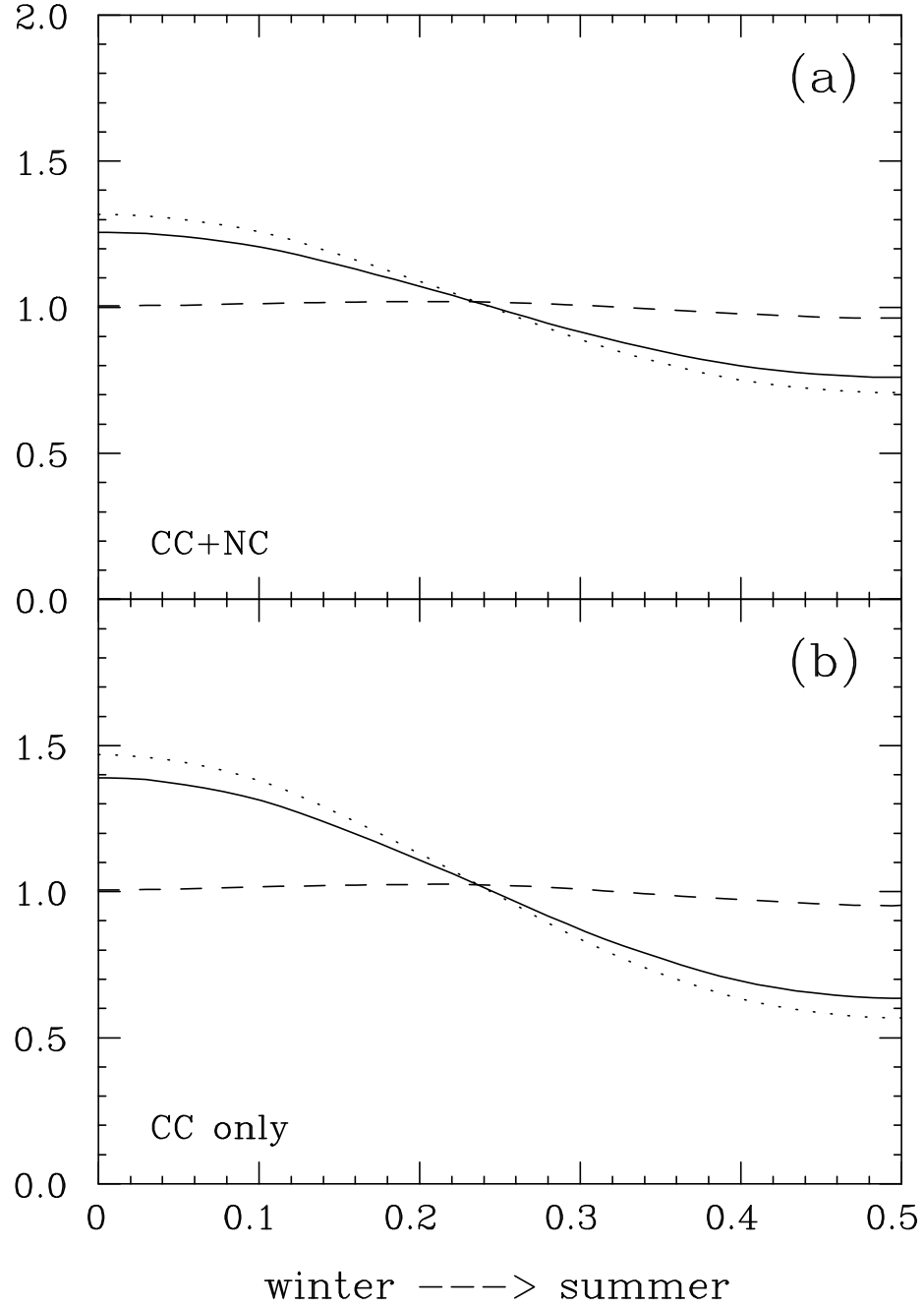


Fig.12

Figure II.10: Expected variation of the ^7Be signal as a function of the absolute time difference from the perihelion in fractions of year (0.5 is the aphelion).

The solid line is the theoretical prediction for the best fit parameters. The dashed line is the case of maximal ^7Be flux within the 90 % C.L. region, while the dotted line gives the maximal seasonal variation within the same region. Signals are normalized so that the yearly average is one.

Plot (a) refers to a detector sensitive to charged and neutral currents and to active neutrinos. Plot (b) refers to a detector sensitive only to charged currents or to sterile neutrinos.

The figure is taken from reference [CFFL95].

Deviations of Fourier coefficients from standard values

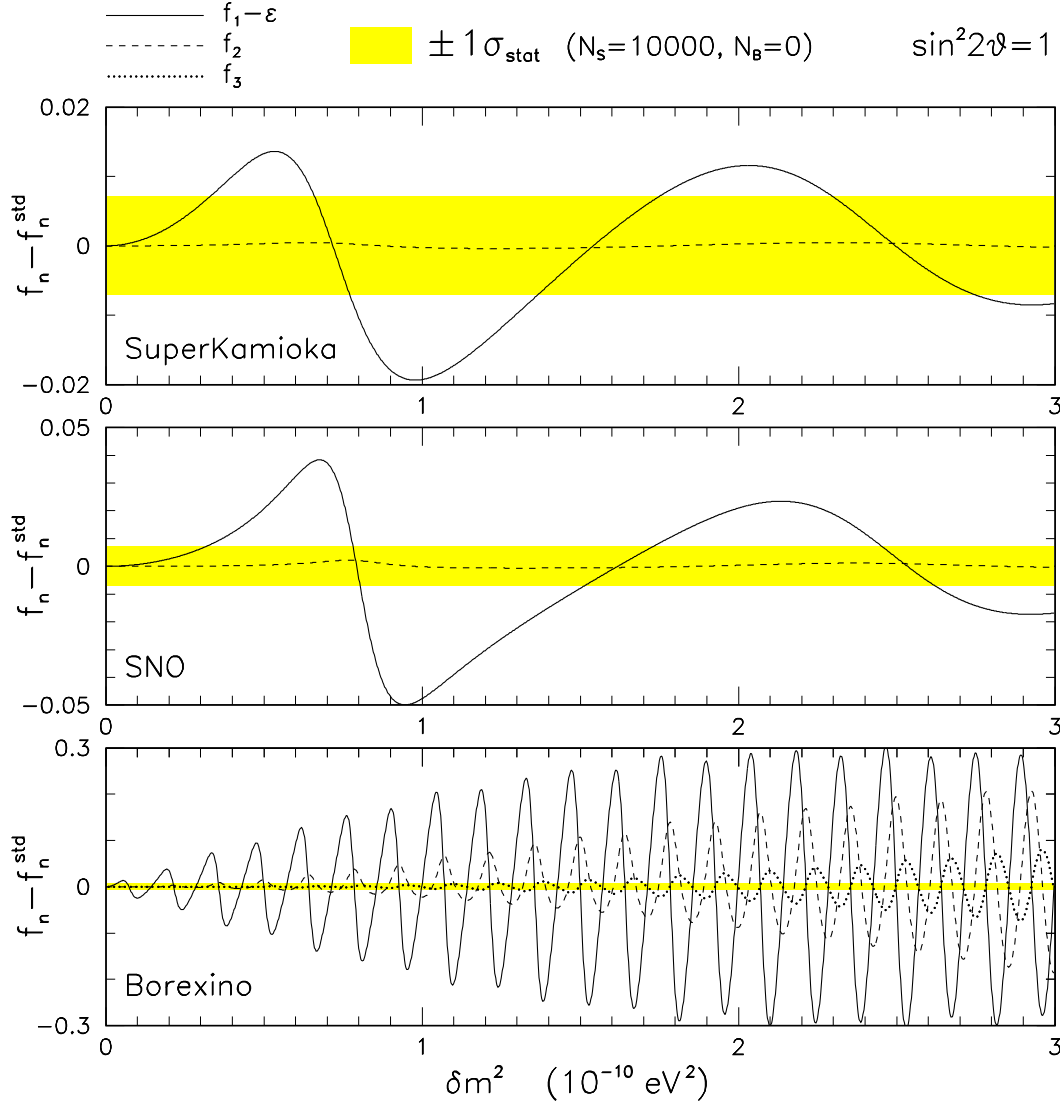


Figure II.11: Deviation from the no-oscillation values for the first three harmonics of the neutrino real time distribution in the experiments SNO, SuperKamiokande and BX. The detection of 10^5 neutrinos is assumed for all the experiments. No background is assumed.

The shadowed yellow bar represents the sensitivity due only to the statistical error. Its absolute width is equal in the three plots.

In presence of a background rate B constant in time and calling with S the signal rate and with T the data taking length, the error would scale according to the factor $\sqrt{(1 + f_{2n} + B/S)/(ST)}$ (where f_n in the n^{th} Fourier coefficient).

In BX the deviation is ten times greater because the neutrino source has a discrete energy spectrum. In SuperKamiokande and SNO the average of the survival probability over the continuous energy spectrum reduces the sensitivity.

The figure is taken from reference [FLM97].

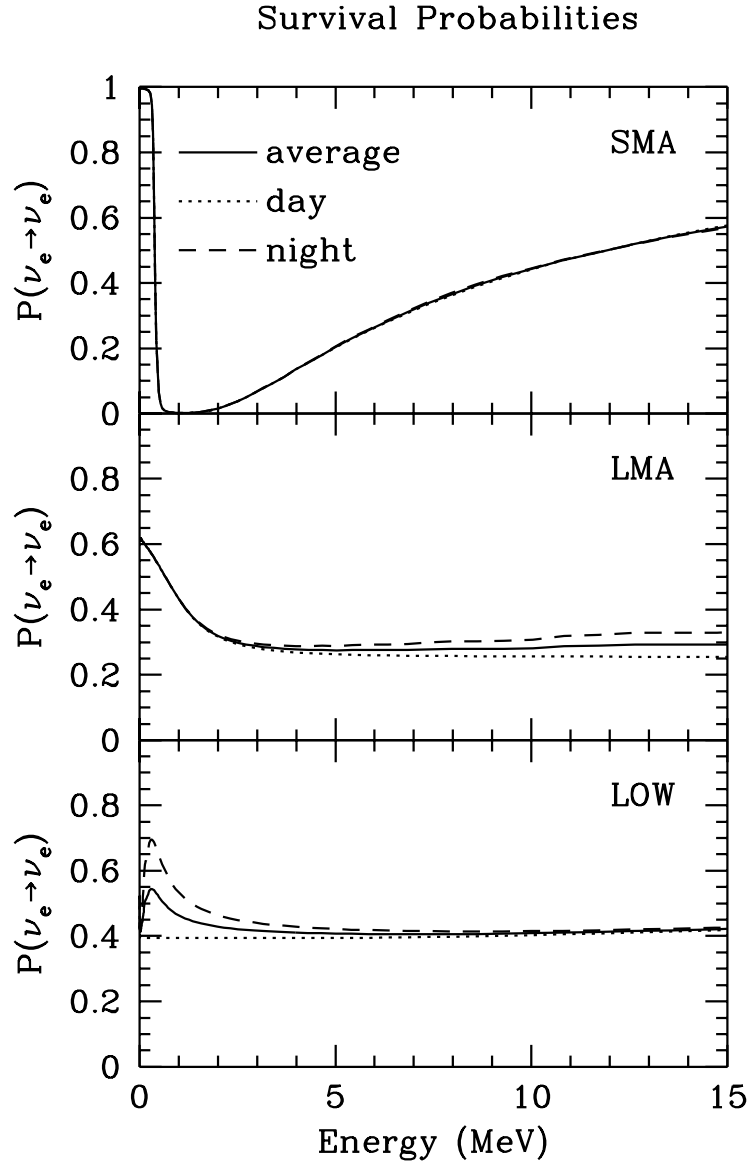


Figure II.12: Survival probability for MSW solutions.

The figure presents the yearly averaged survival probabilities for an electron neutrino that is created in the sun to remain an electron neutrino upon the arrival at the SuperKamiokaNDE detector. There are only slight differences for detectors located in LNGS.

The full line refers to the average survival probabilities computed taking into account regeneration in the earth and the dotted line refers to calculations for the daytime that do not include regeneration. The dashed line includes regeneration at night.

The figure is taken from reference [BKS98].

Chapter III

... and its Counting Test Facility

III-A The CTF project

The scientific goals of BX impose very stringent requirements on the admissible background. The BX requirements on the background at energies lower than 1 MeV are unprecedented.

The key of the feasibility of BX is an extremely low internal background that can be achieved only by means of scintillator purification. The efforts spent in a long research and development project permitted to identify several solutions for the scintillator and the related purification methods. The identified solutions were promising because they allowed to achieve the design goals of internal radioactive contamination in laboratory test performed on small-scale scintillator samples. However, the analytical techniques available at that time (end of 80's) allowed to measure radioimpurities at the BX level only by means of the preconcentration process, which adds a lot of uncertainties to the significance of the measurements. Moreover, the laboratory tests did not allow to verify the purification efficiencies on the tons mass-scale.

Therefore the BX collaboration decided in 1991 to build the detector called Counting Test Facility of BX (CTF), that is a small-scale prototype of BX with a 4.5 tons scintillator mass and a 2.1 m diameter Inner Vessel.

The CTF cannot and it is not aimed to establish the feasibility of BX. The dominating background source in CTF is external background, while in BX it is internal background. Indeed, as far as the external background is concerned, the CTF volume can be compared to the BX crust (see figure II.7): the limited (mass and linear) scale of CTF does not allow to define a fiducial volume and it forbids to check the total internal counting rate at the level of ${}^7\text{Be}$ neutrinos interaction, to say 0.5 counts/day/ton.

On the other hand, CTF can perform several “kill the background or die” tests. Above all, it can check the contamination from the natural radioactive chains (that is supposed to be the strongest source of background in BX) at the level of 5×10^{-16} g/g using the delayed coincidence technique. The same technique allows to measure the contamination of other specific radioactive sources, like the by-product of nuclear fallout ${}^{85}\text{Kr}$. Moreover, CTF can measure the ${}^{14}\text{C}/{}^{12}\text{C}$ relative abundance at the level of 10^{-18} . It can verify the efficiency of the purification methods. Finally, it can be used as a benchmark for the choice of the construction materials.

The CTF has been designed to achieve the following records:

- to measure the ${}^{238}\text{U}$ and ${}^{232}\text{Th}$ contamination in the liquid scintillator with an upper limit of 5×10^{-16} g/g;
- to measure the ${}^{14}\text{C}$ contamination in the liquid scintillator with an upper limit of 10^{-18} for the relative concentration ${}^{14}\text{C}/{}^{12}\text{C}$;
- to check construction materials for very low radioactivity;
- to check purification methods for bulk shielding and detecting materials;
- to determine the optical properties of liquid scintillators;
- to implement cleaning methods during the construction and the installation of the detector and of the auxiliary plants.

During the running of CTF analysis techniques were developed to study the total background rate in CTF, overcoming as much as possible the lack of a fiducial volume. Exploiting the spatial reconstruction of

the events, these techniques allowed to push the CTF sensitivity to the total background rate to 20 times the neutrino interaction rate, thus providing a further “kill or die” test.

Many analysis on the CTF data, including those on the contamination from the natural radioactive chains and on the total counting, have been developed as research work for the preparation of this dissertation, and will be discussed in chapters IV and V.

III-B The structure of the CTF detector

The structure of the CTF detector is very similar to the BX one and it is shown in figure III.1.

The active part of the detector is 4.5 tons of liquid scintillator contained in a spherical nylon bag (Inner Vessel, IV). Figure III.2 is a picture of the IV surrounded by PMTs before the filling of the detector.

The buffer liquid and the SSS present in the BX design are absent in CTF. An Open Structure built with stainless steel tubes acts as support for the PMTs.

The IV is directly immersed in an ultrapure water buffer. The water tank is a cylindrical structure of 11 m diameter and of 10 m height.

The following subsections describe the components of the detector. Emphasis will be given to the description of the electronics, that has some particular feature allowing to tag several background sources.

A very detailed description of the detector and of each of its components can be found in reference [A⁺98b].

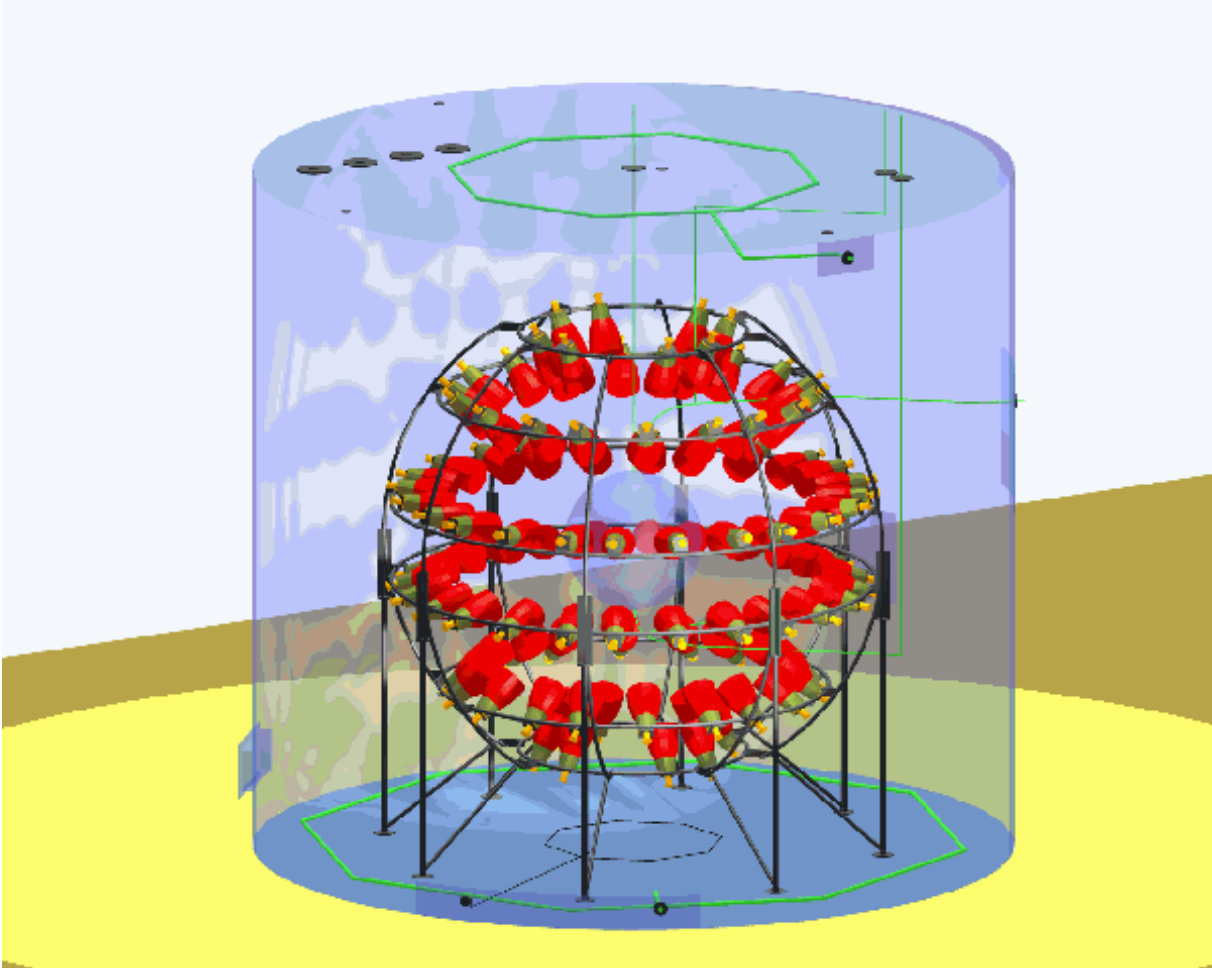


Figure III.1: A drawing of CTF.

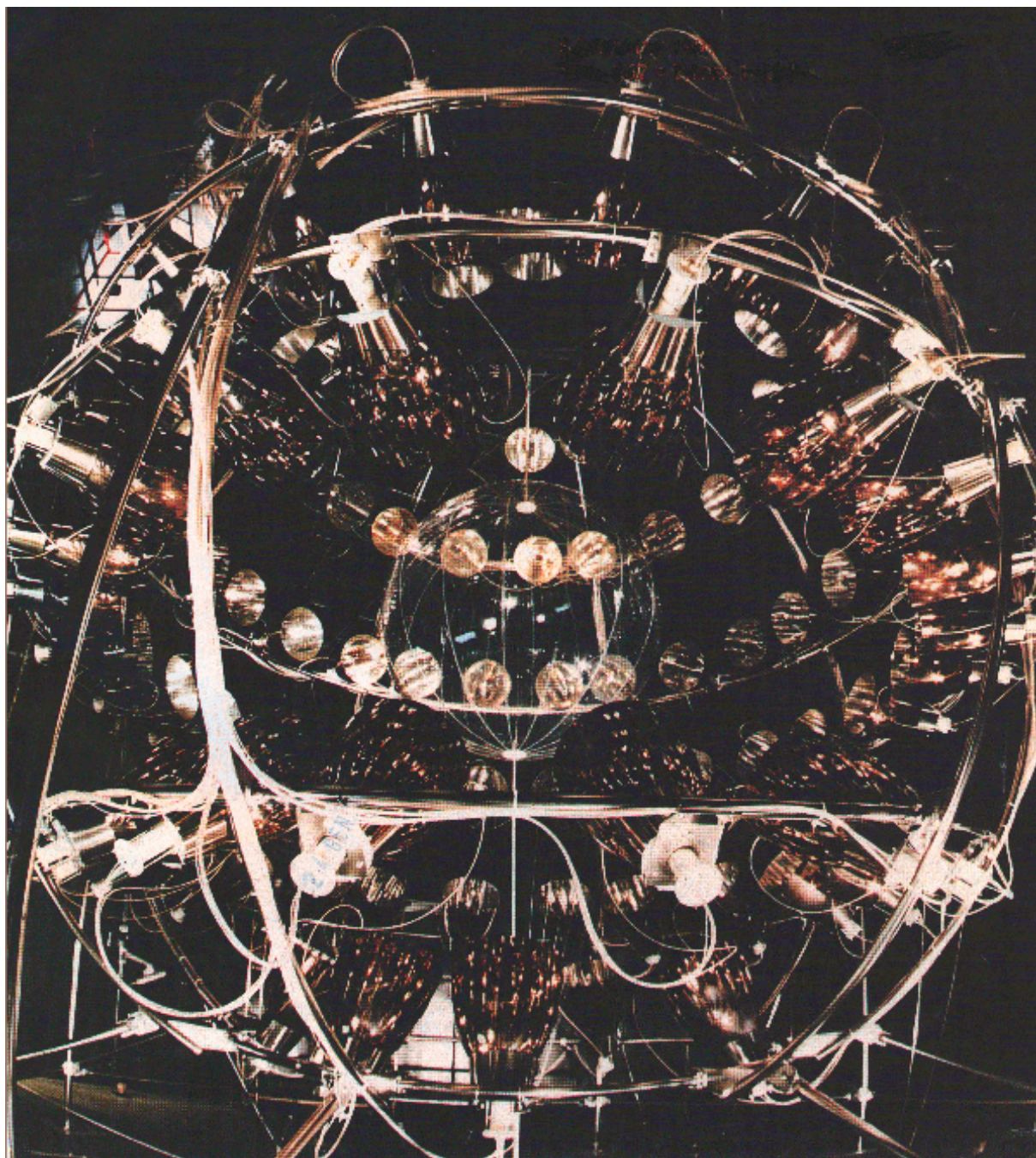


Figure III.2: A picture of the internal part of CTF, showing the Inner Vessel surrounded by PMTs.

III-B.1 The water tank

The tank containing the shielding water is constructed of 8 mm thick carbon steel, coated with Permatex on the interior. It stands 10 m high and it is 11 m in diameter.

The IV is centered horizontally, and its center vertically sits 4.5 m from the bottom of the tank. A steel plate 5 m x 5 m x 50 mm thick was positioned below the center of the tank, to provide equivalent of 4.5 m water shielding of the scintillator in all directions.

During the installation of all the equipments within the tank, the air in the tank itself was filtered through HEPA filters maintaining the atmosphere in the tank as a class $< 10^5$ clean room.

III-B.2 The Water Buffer

The scintillator is shielded by 10^3 m^3 of ultrapure water contained in the water tank.

The ultrapure water is produced by the Water Purification Plant (WPP) which has been already discussed in section II-B.3. The radiopurity levels of the ultrapure water can be found as well in table II.3.

The main function of the ultrapure water buffer is the reduction of the external background. The most penetrating gamma rays among the main components of the local γ -ray flux are emitted from ^{208}Tl with the energy of 2.6 MeV (see table II.1). Since the minimum path in water is 4.5 m and the absorption length for the 2.6 MeV gamma rays in water amounts to 20 cm, the minimum reduction factor achieved by the buffer is 10^{-9} .

The radiopurity levels of ultrapure water are reported in table II.5. The background originating from radioactive contaminants in the ultrapure water buffer is discussed in sections IV-C.2 and V-G.

III-B.3 The Open Structure

It is a structure build by stainless steel electropolished tubes and composed by six parallel and horizontal rings holding the PMTs and the light guides, as it is shown in figure III.1

III-B.4 The nylon scintillator vessel or Inner Vessel

The Inner Vessel confines the scintillator within the water buffer. Being in direct contact with water on the outside and scintillator on the inside, the vessel must be compatible with both ultrapure water and aromatic solvent. It must be optical transparent and it should not contribute significant background from radioimpurities. The vessel sustains the $5 \times 10^3 \text{ N}$ buoyant force associated with the 12 % density difference between scintillator solution and water. These requirements were met by a flexible ball made of the amorphous nylon Durethane C38F. The nylon sheets 0.5 mm thick were cut in an orange slice pattern and solvent welded over a spherical frame. The IV is a spherical nylon bag 1.05 m in diameter and its total volume of amounts to 4.8 m^3 .

In air, the 0.5 mm thick nylon has an optical transmittance of 80 % at 365 nm and the remaining 20 % of the light appears to be reflected or elastically scattered.

The radiopurity levels of nylon are reported in table II.5. The background originating from radioactive contaminants in the IV nylon is discussed in section IV-C.2.

III-B.5 The Scintillator

The scintillator solution used in CTF is a mixture of PC as solvent and a scintillation fluor, PPO, as solute in concentration of 1.5 g/l. After its test in CTF the solution has been adopted as scintillator for BX. A detailed description of the main physical and optical characteristics has already been presented in the frame of BX in section III-B.5.

III-B.6 The Scintillator Purification System

The purification system in use in CTF was composed by the following units:

- sub-micron filtration;
- N_2 counter-current stripping column;
- water extraction unit;
- vacuum distillation unit.

Filtration removes suspended dust particles larger than $50\text{ }\mu\text{m}$. Nitrogen stripping removes dissolved gas impurities. Water extraction is effective at removing ionizable species, such as metals (U, Th, and K). Vacuum distillation removes low volatility components such as metals and dust particles.

The purification system was constructed entirely of electropolished stainless steel, quartz and teflon.

The plant capacity was of 20–50 l/h.

III-B.7 The detection of light

The scintillation light is detected by 100 PMTs held by the Open Structure. The PMTs adopted in CTF were the same selected for BX and section II-B.9 presents a wide discussion of their characteristics.

The components of the bases of the PMTs were selected to minimize the radioactivity. The bases were sealed with a silicon gel to be resistant to water.

The dynodes of the PMTs were shielded against magnetic fields with μ -metal collars.

The PMTs were coupled with light guides shaped as “Winston cones” [WW89] of 57 cm length and of 50 cm maximum diameter. The light collectors were fabricated with low radioactivity UV-transparent acrylic with thin layers of silver and copper deposited on the outer surface of the acrylic, coated with acrylic paint.

A small optical fiber was coupled to each light concentrator. The bunch of all the fibers was connected to a laser for the purpose of charge and time calibrations.

III-B.8 The electronics and the data acquisition

In CTF as well as in BX, the measurement of short time (10^{-7} – 10^{-3} s) delayed coincidences allows to tag the contamination induced by the natural radioactive chains. Therefore the electronics were designed with two parallel chains in order to record the sequence of two delayed coincidences with a dead time of the order of 100 ns after the first trigger.

The electronics for CTF were designed for the following capabilities:

They supply the PMTs with a continuous voltage.

They process the signal coming from the PMTs.

They determine the trigger for the signal coming from each PMT.

They define the “ordinary event” determining the trigger in the first electronic chain.

They define the “delayed coincidence event” determining the trigger in the second electronic chain.

In case of a trigger, they measure and digitalize the following quantities:

- the charge collected by each electronic channel;
- the arrival time of the first photon for each electronic channel;
- the pulse waveshape of each event;
- the time elapsed between possible delayed coincidences.

They record the dark count rate of each PMT and they continuously monitor the gain of the system PMT + amplifier.

They perform the charge and time calibration of the signals by means of the laser and of the connected bunch of optical fibers.

A scheme of the CTF electronics

The signals coming from the PMTs are multiplexed. There are 100 PMTs and only 64 electronic channels. 28 channels have the signal of one PMT as input, and 36 have the signal of two PMTs (close by and held by the same ring) as input.

In case of a trigger, each electronic channel measures the arrival time of the first photoelectron by means of a Time Digital Converter (TDC) and the total charge of the detected photoelectrons by means of an Analog Digital Converter (ADC).

The first electronic chain is composed by:

- 64 TDCs and 64 ADCs (a couple for each channel);
- the trigger of the first chain;

- a Transient Time Recorder (TTR) digitizing the pulse waveshape that is provided by the sum of all the analog signals.

The “ordinary event” is defined as a trigger of the first electronic chain. The dead time for the acquisition of the ordinary events is fixed by the the CAMAC bus transfer time and it amounts to about 10 ms. However, the dead time of the scintillator is much shorter and it is fixed by the decay time of the slow components of the scintillation spectrum, that is of about 50 ns. Therefore it is possible to record delayed coincidences with delay times as short as 50 ns using a separate and dedicated electronic chain.

The second electronic chain is composed by:

- 64 TDCs and 64 ADCs (a couple for each channel);
- the trigger system of the first chain;

The “delayed coincidence event” is defined as a trigger of the second chain. The second chain trigger is enabled starting from 50 ns up to 8 ms since the trigger on the first chain. In case of a trigger on both the first and second chain, the cumulative dead time is always fixed by the CAMAC bus transfer rate and it amounts to about 20 ms.

III-C The CTF data taking

This section provides a summary of the data taking in CTF as a reference for the forthcoming discussion of the data analysis.

The CTF detector was built during the years 1993–94. The data taking started in December 1994 and it ended in January 1997. During the 26 months of data taking the detector configuration was changed several times. The full data taking interval is subdivided in several data taking phases, each phase being defined so as to correspond to a stable detector configuration. Phases are characterized by their start date and end date and by the Runs performed during the phase itself. Each Run corresponds to a data taking interval of 1–2 days. Phases are identified by latin letters and Runs are identified by arabic numbers.

Section III-D is a detailed review of all the phases. Emphasis is given to the detector configuration and to the scintillator processing.

Not all of the phases are relevant for the data evaluation and only few of them are of fundamental interest. Section III-E is a brief review of the only phases which are relevant for the forthcoming discussion of the data analysis.

III-D A detailed review of the data acquisition phases

Alpha The first data were recorded in December 94. The installation of the PMTs had just been completed, the inner vessel was already installed and the water tank had undergone its final cleaning. The water tank had just been closed and sparged with N₂.

During phase Alpha, from December 18th to December 20th, Run # 0 was recorded. The water tank and the inner vessel were filled with N₂.

Bravo The filling of the tank with ultrapure water started in the second decade of December 94. The filling was completed in January 95.

During phase Bravo, from January 10th to January 14th, Runs # 1–2 were recorded. Both the water tank and the inner vessel were filled with ultrapure water.

Charlie The filling of the inner vessel with the first cubic meter of scintillator started in the late January 95. The scintillator was filled into the inner vessel from the top inlet, and the water was drained from the bottom outlet. No on-site purification of the solvent was performed. The only purification processes undergone were distillation of the solvent carried out in the production plant during the synthesis process and water extraction of the fluors performed at Gran Sasso.

During phase Charlie, from February 5th to March 10th, Runs # 34–53 were recorded. The inner vessel was filled with one cubic meter of scintillator and with four cubic meters of water. The scintillator was situated in the upper section of the inner vessel sphere of about 70 cm height.

- Delta** The completion of the inner vessel filling with scintillator of the started in April 95. The scintillator was filled into the inner vessel from the top inlet, and water was drained from the bottom outlet. Four cubic meters of scintillator were filled in. No on-site purification of the solvent was performed. The only purification processes undergone were distillation of the solvent carried out in the production plant during the synthesis process and water extraction of the fluors performed at Gran Sasso.
- During phase Delta, from April 4th to April 6th, Runs # 73–74 were recorded. The inner vessel was being filled with scintillator.
- Echo** The filling of the inner vessel was completed on April 13th 95.
- During phase Echo, from April 14th to April 21st, Runs #76–81 were recorded. The inner vessel was filled with five cubic meters of scintillator.
- Phase Echo is affected by problems on the electronic channels dedicated to the α - β discrimination.
- Foxtrot** The electronic problems affecting phase Echo were solved and fixed as of April 21st.
- During phase Foxtrot, from April 21st to May 27th, Runs #82–99 were recorded. The inner vessel was filled with five cubic meters of scintillator. The electronic problems affecting the previous phase were solved and all the recorded data are reliable.
- Golf** The on-site purification of the scintillator started on May 27th. The scintillator was drained from the bottom outlet of the inner vessel and it was conveyed to the purification plants' box installed on the top of the water tank. The scintillator was circulated through the stripping tower with a N₂ countercurrent and then it was filled back into the inner vessel from the top inlet.
- During phase Golf, from May 27th to July 18th, Runs # 101–157 were recorded. The inner vessel was filled with five cubic meters of scintillator. N₂ countercurrent stripping was performed on the scintillator during this phase.
- Hockey** The stripping with N₂ countercurrent ended on July 18th 95.
- During phase Hockey, from July 18th to July 21st, Runs # 158–163 were recorded. The inner vessel was filled with five cubic meters of scintillator. N₂ countercurrent stripping was performed on the scintillator prior to this phase.
- Phase Hockey is affected by huge problems on the electronics of CTF. The recorded data are almost unusable.
- Juliet** The second step of the scintillator purification started on July 21st 95. The scintillator was processed with countercurrent ultrapure water extraction in the plants' box. Then the scintillator was stripped with N₂ countercurrent to remove water and filled back into the inner vessel.
- During phase Juliet, from July 21st to August 12th, Runs # 164–188 were recorded. The inner vessel was filled with five cubic meters of scintillator. Ultrapure water countercurrent extraction and N₂ countercurrent stripping were performed on the scintillator during this phase.
- Kilo** The second step of the scintillator purification ended on August 12th 95.
- During phase Kilo, from August 12th to September 19th, Runs # 189–219 were recorded. The inner vessel was filled with five cubic meters of scintillator. Ultrapure water countercurrent extraction and N₂ countercurrent stripping were performed on the scintillator prior to this phase.
- Phase Kilo is affected by problems on the electronics of CTF, due also to the simultaneous installation and testing of the electronic channels for the muon chambers. The recorded data are almost unusable.
- Lima** The electronic problems affecting phase Kilo were solved and fixed as of September 19th 95.
- During phase Lima, from September 19th to September 28th, Runs # 220–229 were recorded. The inner vessel was filled with five cubic meters of scintillator. Ultrapure water countercurrent extraction and N₂ countercurrent stripping were performed on the scintillator prior to this phase. The electronic problems affecting the previous phase were solved and all the recorded data are reliable.
- Mike** The last step of the scintillator purification started on September 29th 95. The scintillator was distilled in the plants' box, then stripped with N₂ countercurrent and finally filled back into the inner vessel.
- During phase Mike, from September 29th to November 18th, Runs # 231–278 were recorded. The inner vessel was filled with five cubic meters of scintillator. Distillation and N₂ countercurrent stripping were performed on the scintillator during this phase.

November The distillation was completed on November 18th 95.

During phase November, from November 18th to December 2nd, Runs # 279–289 were recorded. The inner vessel was filled with five cubic meters of scintillator. Distillation and N₂ countercurrent stripping were performed on the scintillator prior to this phase.

The electronics were affected by several problems during this phase. The recorded data are almost unusable.

Oscar The electronics problems affecting phase November were solved as of December 2nd 95.

During phase Oscar, from December 2nd to December 11th, Runs # 290–296 were recorded. The inner vessel was filled with five cubic meters of scintillator. Distillation and N₂ countercurrent stripping were performed on the scintillator prior to this phase. The electronic problems affecting the previous phase were solved and all the recorded data were reliable.

Papa The radon-in-water test started on December 12th 95. The aim of the test was to verify the contribution of external sources to the CTF background by probing the detector's response to an increase of the main external source, ²²²Rn dissolved in the water buffer. The ²²²Rn concentration in water was raised by a factor of about 100 by means of the insertion of 5 m³ of water (purified but not stripped with N₂ countercurrent) rich of ²²²Rn. The insertion of ²²²Rn in the water buffer took place on December 12th.

During phase Papa, on December 12th, Run # 297 was recorded. The inner vessel was filled with five cubic meters of scintillator. Insertion of ²²²Rn in the water buffer was being performed during this phase.

Quebec The insertion of ²²²Rn in the water buffer finished on December 12th. At the end of the insertion, the external background was overwhelming any other source. The leading activity of the external background was decaying exponentially with the ²²²Rn meanlife and it was monitored for a period of about 40 days up to when it reached the usual values.

During phase Quebec, from December 13th to January 23rd, Runs # 298–339 were recorded. The inner vessel was filled with five cubic meters of scintillator. Introduction of ²²²Rn in the water buffer was being performed prior to this phase. The overwhelming signal from external background was decaying exponentially.

Rubatto The insertion into the inner vessel of ²²²Rn localized sources started on January 23rd 96. The sources were made of ²²²Rn dissolved in few cm³ of scintillator. The scintillator was enclosed in cylindrical quartz vessels, with diameters of about 1 cm and height of about 3 cm. The tests were aimed to calibrate the detector and the position reconstruction code, and to study the light propagation in the scintillator.

During phase Rubatto, from January 23rd to July 20th, Runs # 340–487 were recorded. The inner vessel was filled with five cubic meters of scintillator. Introduction of ²²²Rn sources in the inner vessel was being performed during this phase.

Sierra The test of a second scintillator based on the Pxe solvent in CTF started on July 20th 96.

This phase refers to all the Pxe based scintillator test. It is not divided in smaller units because the measurements on Pxe are not object of this thesis.

During phase Sierra, from July 20th 96 to July 3rd 97 Runs # 488–641 were recorded.

III-E A review of the data acquisition phases relevant for the discussion of the data analysis

The relevant phases are:

Foxtrot during phase Foxtrot the first data with the inner vessel completely filled of scintillator were recorded. No on-site purification of the solvent was performed. The only purification processes undergone were distillation of the solvent carried out in the production plant during the synthesis process and water extraction of the fluors performed at Gran Sasso. The data taking length amounts to 36 days.

Golf during phase Golf the first data during the N₂ sparging were recorded. Owing to a leakage in the N₂ pipes, a relevant sample of ²²⁰Rn nuclides was observed in the vessel. The data taking length amounts to 51 days.

- Lima** during phase Lima the first good data after scintillator water extraction were recorded. The data taking length amounts to 9 days.
- Oscar** during phase Oscar the first good data taken after scintillator distillation. The data taking length amounts to 25 days.
- Quebec** during phase Quebec the data during the ^{222}Rn -in-water test (just after the insertion of ^{222}Rn in water) were recorded. The data taking length amounts to 40 days.

Chapter IV

Measurements performed using the delayed coincidence method

The ability to record delayed coincidences is one of the most powerful features of CTF. It allows to select specific background sources from the burden of all the backgrounds. A narrow selection of the background sources was fundamental to calibrate the detector and to calculate the contamination induced by specific isotopes.

Let's consider the decay of two nuclides in a radioactive chain. Let's suppose the second nuclide has a "short" lifetime that we indicate with τ . By "short" we mean that τ is much lower than the background rates r_1 and r_2 for the decay of the first and of the second nuclide. The delayed coincidence method consists in the selection of the combined signals from the two nuclides: one looks for a couple of subsequent events separated by no more than τ in time and having respectively the characteristics of the first and of the second nuclide. The delayed coincidence method is very efficient because the background rate for the selection of the combined signals is:

$$r_1 \times r_2 \times \tau \quad (\text{IV.1})$$

and it is much lower than r_1 and r_2 .

The trigger rate of CTF was of about 1 Hz and typical background rates for the signals from specific decays ranged from 10^{-1} Hz to 10^{-3} Hz. The CTF electronics recorded delayed coincidences at delay times as short as 100 ns. The delay times of the relevant coincidences were in the range 10^{-7} – 10^{-4} s. Indeed it was possible to upgrade the sensitivity by a factor 10^3 – 10^5 simply by using the delayed coincidence method.

IV-A The initial ^{222}Rn contamination: a powerful monitoring tool

The filling of the first ton of scintillator was realized successfully but not without problems.

Once the tank containing the scintillator had been shipped in LNGS, it was realized that the tank was leaking. Owing to the leak some air mixed with the scintillator during the shipping. Furthermore, pipes and connections of the fluid handling plant were not completely tight. During the filling some air of the underground laboratories - with a ^{222}Rn concentration of about 30 Bq/m³ - contaminated the scintillator.

Just after the filling of the first ton of scintillator the trigger rate of CTF was of about 7 Hz. The main contribution to the trigger rate was from the activity of ^{222}Rn and daughters dissolved in the scintillator and coming from air. When the filling of the inner vessel with scintillator was completed the problem of the leaking tank was solved. On the other hand the tightness of pipes and connection was not yet achieved. During the completion of the filling a big increase of the activity of ^{222}Rn dissolved into the scintillator was observed. After the completion of the filling, the trigger rate of CTF was of about 1.5 Hz. The ^{222}Rn activity into the scintillator amounted to 3×10^{-2} Bq. Once the ^{222}Rn decayed the trigger rate of CTF settled down at the level of 0.9 Hz. The main contribution to the trigger rate was due to decay of ^{14}C in the scintillator.

The initial ^{222}Rn contamination produced by the filling procedures gave rise to serious problems. First, it was necessary to wait several weeks until the ^{222}Rn decay rate decreased to a level that allowed the measurements of the ^{238}U and ^{232}Th intrinsic contamination of the scintillator. Moreover a sample of the ^{210}Pb nuclides, daughter of ^{222}Rn decaying with a 32 years meanlive, was left into the IV. ^{210}Pb is an important source of background owing to the decay of its daughters ^{210}Bi (β emitter; $Q = 1.17$ MeV; $\tau = 7.23$ d) and ^{210}Po (α emitter; $Q = 5.3$ MeV; $\tau = 200$ d). The relevance of this background source in the CTF frame will be discussed in section V-G.

Table IV.1: Results of the measurements of quenching factors and electron equivalent energies for α particles performed in the Munich experiment.

Nuclide	Q [MeV]	quenched energy [keV]	quenching factor
^{210}Po	5.30	395 ± 10	13.4 ± 0.3
^{222}Rn	5.49	410 ± 6	13.4 ± 0.2
^{218}Po	6.00	483 ± 6	12.4 ± 0.2
^{214}Po	7.68	751 ± 7	10.2 ± 0.1

However, the initial ^{222}Rn contamination offered also a good opportunity. It was possible to get a rough and preliminary energy calibration of the detector by checking the detector against the signal of a well known source. The calibration was obtained by measuring in CTF the light yield of the α particles belonging to the ^{222}Rn chain and by measuring in laboratory the values of the α energy quenching (to electron equivalent energy), as it is described in sections IV-A.1 and IV-A.2.

IV-A.1 The Munich measurement on α quenching

The values of the α energy quenching to the electron equivalent energy for the CTF scintillator were measured at the Technical University of Munich by M. Neff et al. [Nef96].

The Munich experiment was mainly aimed at studying the extraction efficiency of several purification methods for the nuclides ^{210}Po and ^{210}Pb . A sample of the CTF scintillator was exposed to a high ^{222}Rn density for several weeks in order to achieve a high concentration of ^{210}Po and ^{210}Pb .

The measurement consisted in checking the compton edges of the two following γ -rays sources against the electron equivalent energies of the α particles daughters of ^{222}Rn :

- ^{22}Na (γ -ray energy 511 KeV; compton edge 341 KeV)
- ^{137}Cs (γ -ray energy 661.7 KeV; compton edge 477 KeV)

The results are summarized in table IV.1. The measurements showed that the α -quenching factors range from 13 to 10 for α particles with energies between 5 and 8 MeV.

IV-A.2 The energy calibration

The sequence composed by $^{214}\text{Bi}(\beta)$ - $^{214}\text{Po}(\alpha)$, daughters of ^{222}Rn , can be tagged very efficiently with the delayed coincidence method (see also a more detailed discussion in section IV-C). By means of this method a clean sample of mass 214 sequences, shown in figure IV.1, was selected during phase Foxtrot.

The best value of the photoelectron yield is deduced from the light yield of the ^{214}Po nuclides selected in the abovementioned sample. It amounts to 300 photoelectrons/MeV. The energy resolution is also evaluated from the width of the ^{214}Po peak. The resolution is 9 % (1σ) at the electron equivalent energy of 750 KeV. It is expected to scale as $1/\sqrt{E}$.

The mean value of the ^{214}Po energy is reconstructed with the accuracy of a fraction of percent. The value of the α quenching has an accuracy of 1 %. The photoelectron yield has a bigger relative error (10 %) owing to possible systematic effects. In fact the vial source tests (discussed in section V-G) showed that fluctuations in the energy response due to the variation of the source position in the IV amount to 10 %.

A check of the linearity of the energy response was obtained by means of the α decays of ^{222}Rn and ^{218}Po (Q values 5.49 and 6.02 MeV, quenched to 410 ± 6 and 483 ± 6 KeV respectively). A fit of the combined energy distribution allowed to reconstruct the mean electron equivalent energies for the decays of the two nuclides at 405 ± 7 and 488 ± 10 KeV, confirming the linearity within a few percent. A second linearity check was provided by the study of the ^{85}Kr decay (see section IV-D). The peak from the 514 KeV gamma which is emitted in the 0.43 % branching ratio is situated within 5 % from the expected position. A third linearity check was provided by the spectrum of ^{222}Rn dissolved in the water buffer, which was measured during the radon-in-water test (discussed in section V-G). The shoulder from the 609 KeV γ -rays emitted from the daughter ^{214}Bi is centered within a few percent of the nominal value.

IV-B The ^{232}Th contamination

IV-B.1 The sensitivity

The CTF measures the activity of the ^{232}Th chain in the scintillator by probing the rate of the daughter sequence $^{212}\text{Bi}(\beta)$ - $^{212}\text{Po}(\alpha)$.

The ^{232}Th chain is shown in figure IV.15. Because of possible breaking of the chain at the level of ^{228}Th (meanlife of 2.7 years) the measurement reports directly the ^{228}Th contamination. For the sake of convenience the results will be quoted in terms of ^{232}Th equivalent contamination as if the chain were in secular equilibrium.

The meanlife of ^{232}Th amounts to 1.41×10^{10} y. The only branch in the chain starts with the ^{212}Bi nuclide: ^{212}Bi decays with a 64 % branching ratio into ^{212}Po emitting β and γ -rays, and it decays with a 36 % branching ratio into ^{208}Tl emitting an α particle.

Considering the ^{232}Th meanlife, the branching ratios of the ^{212}Bi decay and the density of the scintillator, at the ^{232}Th equivalent contamination level of 10^{-16} g/g the expected rate for the mass 212 sequences is 2.0×10^{-2} events/day/ton.

^{212}Bi decays into ^{212}Po emitting β and γ -rays with a meanlife of 87.4 min. The Q value amounts to 2.25 MeV. ^{212}Po decays into ^{208}Pb emitting an α particle with a meanlife of 432 ns. The Q value is 8.79 MeV and the electron equivalent energy is 1010 KeV. The corresponding quenching value has not been measured directly and it is based on the extrapolation of the values measured at lower energies in the Munich experiment (see section IV-A). Table IV.2 resumes the physical characteristics of the two nuclides decays.

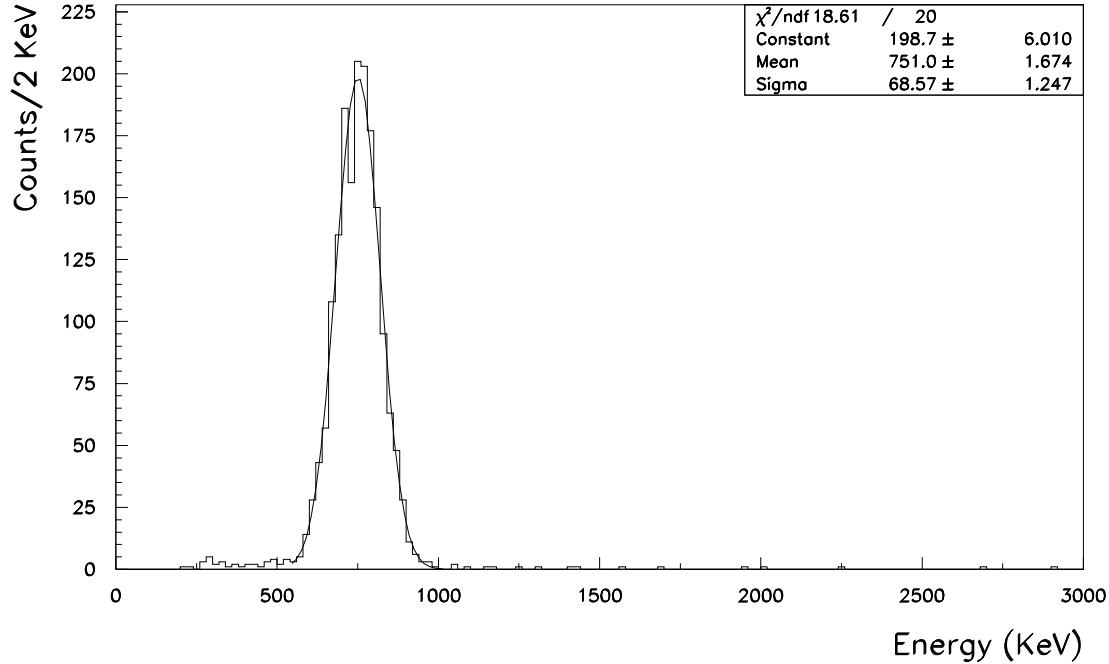


Figure IV.1: Phase Foxtrot, Runs # 82–85 only.

Energy spectrum of ^{214}Po candidates.

The candidates are selected using a subset of the U cuts described in section IV-C.

The cuts used are: coincidence cut (the delay time between the candidate ^{214}Bi and ^{214}Po is required to be lower than two times the ^{214}Po meanlife. The efficiency for the mass 214 sequences is 88 %); cut on the energy of the candidate ^{214}Bi (the energy is required to be greater than 300 KeV. It discards most of the random background. The efficiency for the mass 214 sequences is 90 %). No cut on the energy of the candidate ^{214}Po is applied.

Table IV.2: Decay products, Q values, electron equivalent energies and meanlives for mass 212 sequence nuclides.

Nuclide	Decay products	Q	Electron equivalent energy	Meanlife
		[MeV]	[MeV]	[s]
^{212}Bi	$\beta + \gamma$	2.25	$0 \rightarrow 2.25$	5.2×10^3
^{212}Po	α	8.79	1.01	4.32×10^{-7}

Table IV.3: Efficiencies of the Th cuts for the selection of mass 212 sequences.

Cut	Efficiency (212)
Delay	0.79
Energy first event	0.90
Energy second event	0.98
Combined cuts	0.70

Selection of mass 212 sequence candidates is performed by means of the following cuts, referred to as the Th cuts:

- the delay between the two candidate events must lie in the range between 100 and 2000 ns.

The upper limit of the range is roughly five times the ^{212}Po meanlife.

The lower limit of the range has been selected taking into account the features of the CTF electronics. The dead time after the record of an event on the main electronic chain amounts to 50 ns and the ADCs gates are open for 70 ns. The value of 100 ns has been selected in order to discard with a safety margin any sequence of events presenting a pile-up in the ADCs measurement.

The efficiency of the delay cut is 79 % for mass 212 sequences.

- the energy of the candidate ^{212}Bi must exceed 300 KeV.

Since 90% of the CTF spectrum is detected below the threshold of 300 KeV, the cut rejects 90 % of the random coincidences.

Moreover, the cut discards only 10 % of ^{212}Bi events because the ^{212}Bi energy spectrum is shifted to higher energies.

The efficiency of the ^{212}Bi energy cut is 90 % for mass 212 sequences.

- the energy of the candidate ^{212}Po must lie within 2σ from the mean value expected for ^{212}Po events.

The cut also helps in rejecting random coincidences.

Moreover, it discards only 2 % of ^{212}Po events.

The efficiency of the ^{212}Po energy cut is 98 % for mass 212 sequences.

It is also necessary to remove by hand from the sample of mass 212 sequence candidates the fake sequences due to muon signal reflections. These fake sequences are due to reflections of the signal on the first stage of the electronics chain, the amplifier, owing to the impedance mismatch at the level of 2 % on the 50 Ω nominal value. The back scattered wave is forward scattered by the PMTs without amplitude reduction since the PMTs are not terminated at 50 Ω . For huge main signals like muons crossing the inner vessel, the reflections can trigger the auxiliary chain. The fake sequences are characterized by the fixed delay of 400 ns which is determined by the length of the cables. They are removed by means of the inspection the waveshape recorded by the TTR (see section III-B.8). Since the waveshape of a muon crossing the inner vessel is completely different from that of a scintillation event, all the fake sequences are identified and none of the scintillation sequences is misidentified. Therefore the efficiency of this cut for mass 212 sequences is 1.

The global efficiency of the combined Th cuts for mass 212 sequences amounts to 70 %. A summary of the efficiencies of the Th cuts is reported in table IV.3.

The rate of random sequences surviving the Ml cuts amounts to:

$$r = r_1 \times r_2 \times \tau \quad (\text{IV.2})$$

$$= 10^{-1} \text{ s}^{-1} \times 10^{-2} \text{ s}^{-1} \times 10^{-6} \text{ s} \quad (\text{IV.3})$$

$$= 10^{-9} \text{ s}^{-1} \quad (\text{IV.4})$$

and it is negligible. The lowest measurable ^{232}Th contamination in CTF in the data taking length of one year is limited by statistics. At the 3σ confidence level it corresponds to 7 expected decays, which is equivalent to $2 \times 10^{-17} \text{ g/g}$.

IV-B.2 The toron

The data collected during phase Golf contain our biggest sample of mass 212 sequences. In phase Golf it took place the first step of purification, consisting in on-line sparging of the scintillator with a N_2 countercurrent. At the same time a huge increase of the ^{222}Rn activity in the vessel was observed. The most likely interpretation is that an imperfect tightness of the pipes of the fluid handling plant allowed some air of the underground labs to mix with the scintillator.

In phase Golf a sample of 62 candidate mass 212 sequences was selected by means of the Th cuts. Figures IV.2 and IV.3 shows the distribution of delay and of energy of the candidates ^{212}Po for the selected sample. The activity of mass 212 sequences deduced from these distributions amounts to 5 counts/day and it is much higher than the activity recorded in the previous phases. The interpretation for the increase of mass 212 sequences activity was that the excess of mass 212 sequences were daughters of ^{220}Rn coming from air. The ^{220}Rn nuclide, also known as toron, has a very short lifetime amounting to 80 s. It lives in a gaseous phase as well the other Rn isotopes, and it might have been coming from air together with ^{222}Rn .

The study of signal from toron showed a potentially relevant problem. Both the abovementioned distributions indicate the possible presence of a background source for the mass 212 sequences signal. The delay time distribution shows the presence of a background source passing the Th cuts and characterized by delay time bigger than ^{212}Po meanlife. The energy distribution of candidates ^{212}Po shows as well the possible presence of background in the lowest part of the energy window defined by Th cuts.

In order to clarify the pattern a wider selection of the sample was performed. The new selection criteria differed from the previous in the requirements for two parameters, owing to the necessity to explore the possible sources of background for the 212 mass sequence signal: the delay times was required to be greater than 100 ns and lower than 10 μs ; the energy for the candidate ^{212}Po was required to be between 700 KeV and 2σ plus the mean expected value for ^{212}Po . Figure IV.4 shows the distribution of delay time versus energy for the candidate ^{212}Po in the sample selected with the wider cuts. Three classes of events are identified:

- the bunch of mass 212 sequences having delay times lower than 1 μs and energies of about 1.1 MeV;
- the belt of mass 214 sequences having delay times uniformly distributed and energies of about 0.8 MeV;
- the lonely event with delay time of about 7 μs and energy of about 1.2 MeV. I have no interpretation for that event.

Mass 214 sequences are daughters of ^{222}Rn . The first nuclide is ^{214}Bi and the second is ^{214}Po . The nuclides decay are very similar to those of the mass 212 sequence decays except for some difference (see also section IV-C):

- the first decay in the mass 214 sequence gives a $(\beta+\gamma)$ -ray whose Q value is very close to that of ^{212}Bi , the first nuclide in the mass 212 sequence. Therefore the first events of the two sequences are almost indistinguishable;
- the second decay gives an α particle with a mean expected energy 3σ far from the mean expected energy of the ^{212}Po ;
- the mass 214 sequence delay time is roughly 10^3 greater than the 212 sequence delay.

If the rate of mass 214 sequences is very high, they could represent a background source for the mass 212 sequences signal. It is not impossible to disentangle the two signal sources, because the mean expected energies of the second events are 3σ apart and the delay time distribution are significantly different. But since the mass 212 sequences rates is really low, the mass 214 contribution to the mass 212 signal must be carefully subtracted in order to evaluate correctly the ^{232}Th contamination.

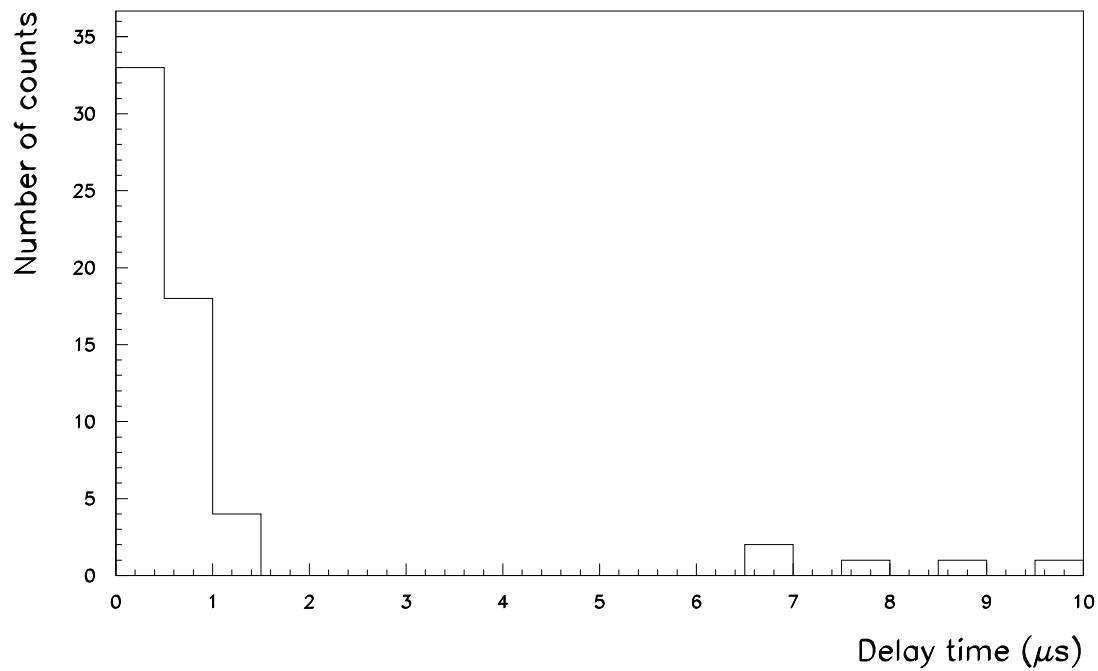


Figure IV.2: Phase Golf.

Delay time distribution for the sample of sequences selected by means of the Th cuts.

Two classes of events are identified: at delay time lower than $1\ \mu\text{s}$ a probable bunch of mass 212 sequences; at delay times greater than $5\ \mu\text{s}$ a possible source of background with delay times greater than ^{212}Po meanlife.

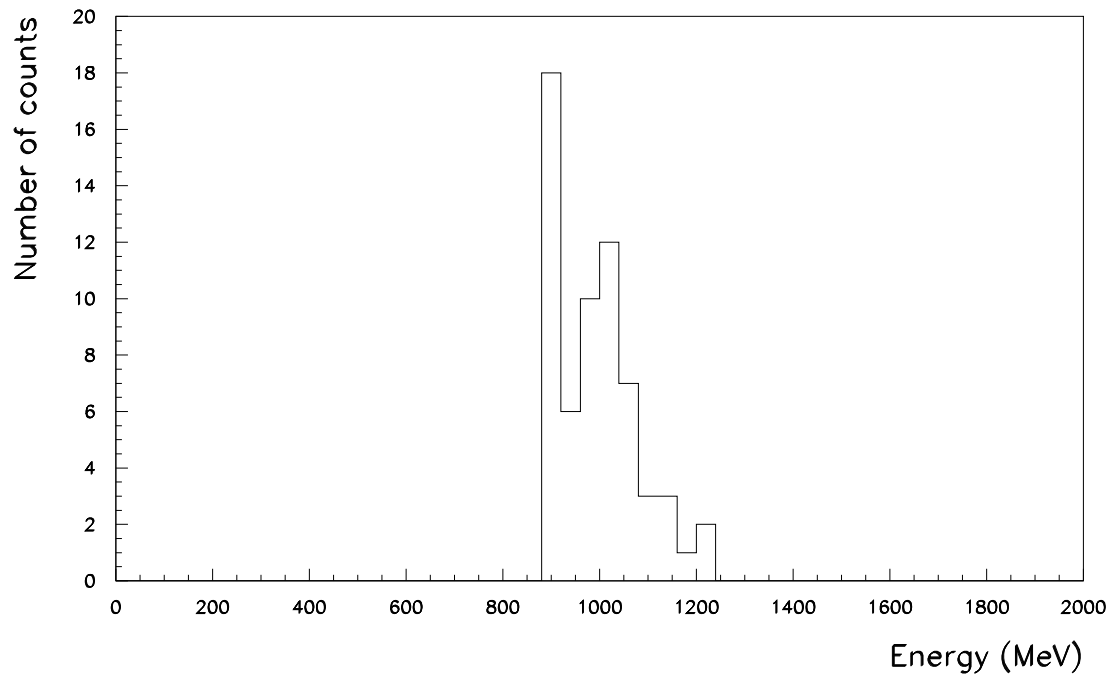


Figure IV.3: Phase Golf.

Energy distribution for the candidate ^{212}Po in the sample of sequences selected by means of the Th cuts. The bunch of mass 212 sequences forms a peak around the central value of 1.0 MeV. At the lower limit ($\simeq 0.9$ MeV) of the 2σ energy window of about a count excess may be interpreted as a possible background from lower energy events.

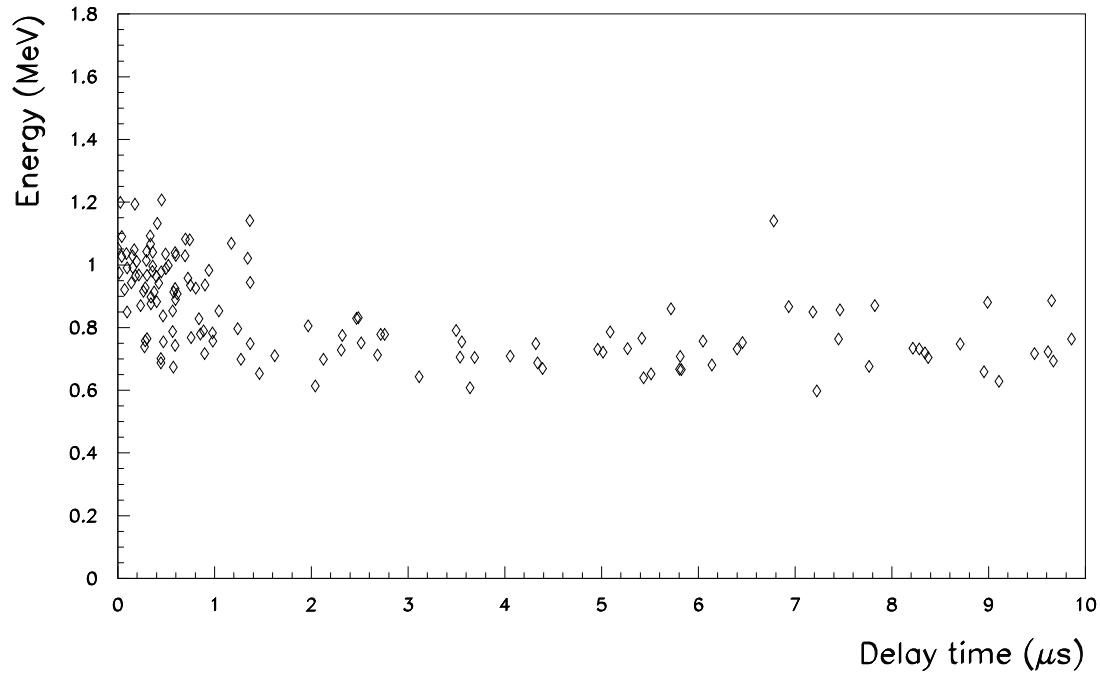


Figure IV.4: Phase Golf.

Distribution of delay time versus energy for the candidate ^{212}Po for in the sample of sequences selected by means of the wider Th cuts.

Three classes of events are identified: the bunch of mass 212 sequences having delay times lower than $1\ \mu\text{s}$ and energy of about 1.0 MeV; the belt of mass 214 sequences having delay times uniformly distributed and energy of about 0.8 MeV; a lonely and “spurious” event with delay time of about $7\ \mu\text{s}$ and an energy of about 1.2 MeV.

Table IV.4: Efficiencies of the Th cuts for the selection of mass 212 and of mass 214 sequences.

Cut	Efficiency (for mass 212)	Efficiency (for mass 214)
Delay	0.79	0.09
Energy first event	0.90	0.97
Energy second event	0.98	0.99
Combined cuts	0.71	0.08

IV-B.3 The Maximum Likelihood method

The data taking phases Foxtrot, Lima and Oscar were not performed in optimal conditions. For all the three phases the data taking started just after the completion of scintillator processing. All the operations performed on the scintillator had as a side effect a huge increase of ^{222}Rn in the scintillator. Our present understanding of the problem is that the ^{222}Rn came from air owing to imperfect tightness of the pipes in the fluid handling plant. Furthermore, the data taking of each of the three phases was stopped just few days after the ^{222}Rn rate reached a level allowing a measurement of the mass 212 sequences with a negligible background from mass 214 sequences. The reason for cutting the data taking was the necessity of performing many tests on the purification plants in a short time. Therefore the most important data of the experiment were taken in presence of a transient and huge source of background, ^{222}Rn which would have been absent if the time available for the tests had been three times greater.

The transient ^{222}Rn background gave rise in all of the three data taking phases to some thousands of the mass 214 sequences. Considering the ratio of the ^{212}Po to the ^{214}Po meanlife, it can be estimated that in each of the three phases some (up to twenty) mass 214 sequences are detected with a delay time compatible with that of a mass 212 sequence. Consequently in order to measure the rate of mass 212 sequences it is necessary to monitor the possible transient ^{222}Rn background and to subtract the mass 214 sequences contribution to the mass 212 sequences signal. We decided to use the maximum likelihood method in order to perform correctly this subtraction. The maximum likelihood method allows to reconstruct the number of counts due to the single sources on the basis of the distributions recorded for a mixed sample of events coming from several sources. This method is usually employed in the frame in low counting rate experiment to disentangle background sources from the signal.

In order to monitor the background from the mass 214 sequences the cuts on the delay time and on the energy of the second events were relaxed. This new set of cuts will be referred to as the maximum likelihood (ML) cuts:

- the delay between the two candidate events must lie in the range between 100 and 20000 ns.
The upper limit is of the order of one tenth of the ^{214}Po meanlife, in order to monitor a significant fraction of the mass 214 activity.
The lower limit is the same as in the Th cuts.
The efficiency of the delay cut is 80 % for the mass 212 sequences.
- the energy of the candidate first event recorded in the main electronic channel must exceed 300 KeV.
The efficiency of the ^{212}Bi energy cut is 90 % for the mass 212 sequences and it is 98 % for the mass 214 sequences.
- the energy of the candidate second event recorded in the auxiliary electronic channel must lie within 2σ whether from the mean value expected for ^{212}Po events or from the mean value expected for ^{214}Po events.
The efficiency of the ^{214}Po energy cut is 99 % for both the mass 212 and the mass 214 sequences.

The global efficiency of the combined ML cuts amounts to 71 % for the mass 212 sequences and to 8 % for the mass 214 sequences. A summary of the efficiencies of the ML cuts for both the mass 212 and of the mass 214 sequences is reported in table IV.4.

The distributions having markedly different probability density distributions for the signal and the background are the most useful in disentangling the source signal from the background signal. In the present case, this role is played by the distributions in the energy of the second event (E), in the delay between the two

events (t) and in real time from the start of the data taking (T). Considering possible mass 212, mass 214 and random sequences, the function describing the probability density to obtain a sequence with the given parameters (E,t,T) is:

$$\rho(E, t, T; w_{212}, w_{214}, w_{\text{random}}) = w_{212} \times \rho_{212}(E, t, T) \quad (\text{IV.5})$$

$$+ w_{214} \times \rho_{214}(E, t, T) \quad (\text{IV.6})$$

$$+ w_{\text{random}} \times \rho_{\text{random}}(E, t, T) \quad (\text{IV.7})$$

$$= w_{212} \times e^{-t/\tau_{212}} \times e^{-(E-E_{212})^2/2\sigma_{212}^2} \quad (\text{IV.8})$$

$$+ w_{214} \times e^{-t/\tau_{214}} \times e^{-(E-E_{214})^2/2\sigma_{214}^2} \times e^{-T/\tau_{\text{Rn}}} \quad (\text{IV.9})$$

$$+ w_{\text{random}} \times f(E) \quad (\text{IV.10})$$

where:

τ_{212} is the ^{212}Po meanlife;

E_{212} is the ^{212}Po energy;

σ_{212} is the ^{212}Po energy standard deviation;

ρ_{212} is the mass 212 sequence probability distribution function;

w_{212} is the mass 212 sequence weight;

τ_{214} is the ^{214}Po meanlife;

E_{214} is the ^{214}Po energy;

σ_{214} is the ^{214}Po energy standard deviation;

ρ_{214} is the mass 214 sequence probability distribution function;

w_{214} is the mass 214 sequence weight;

τ_{Rn} is the ^{222}Rn meanlife;

f is the function describing the probability density for the energy of random events.

the first addendum in the above formula represents the probability to obtain a mass 212 sequence, the second represents the probability to obtain a mass 214 sequence and the third the probability to obtain a random sequence. The three weights have the dimension of $(\text{Energy} \times \text{time})^{-1}$.

Let's now consider the case when a number of n sequences are selected. Let's indicate each one of the sequences with the label i ($i=1,n$), and the respective energies of the second event, delay time and real time with t_i , E_i and T_i . The likelihood is a function of the parameters w_{212} , w_{214} and w_{random} , and its value is determined by the values of the physical quantities t_i , E_i and T_i . The likelihood function represents the probability that in the case n sequences are detected the first is characterized by the values (t_1, E_1, T_1) , the second by the values (t_2, E_2, T_2) and so on:

$$L(w_{212}, w_{214}, w_{\text{random}}) = \prod_{i=1}^n \rho(E_i, t_i, T_i; w_{212}, w_{214}, w_{\text{random}}) \quad (\text{IV.11})$$

the best estimate for the values of w_{212} , w_{214} and w_{random} is defined as that point of the parameter space which maximizes the likelihood function. The best estimates of counts for each source, n_{212} , n_{214} and n_{random} , are deduced directly from the best estimates of the weights:

$$n_{212} = w_{212} \times \int \rho_{212}(E, t, T) dE dt dT \quad (\text{IV.12})$$

$$n_{214} = w_{214} \times \int \rho_{214}(E, t, T) dE dt dT \quad (\text{IV.13})$$

$$n_{\text{random}} = w_{\text{random}} \times \int \rho_{\text{random}}(E, t, T) dE dt dT \quad (\text{IV.14})$$

$$(\text{IV.15})$$

In order to calculate and maximize the likelihood function it is convenient to deal with its logarithm version:

$$\Lambda(w_{212}, w_{214}, w_{\text{random}}) = \log L(w_{212}, w_{214}, w_{\text{random}}) \quad (\text{IV.16})$$

$$= \sum_{i=1}^n \log \rho(E_i, t_i; w_{212}, w_{214}, w_{\text{random}}) \quad (\text{IV.17})$$

the uncertainty region (1σ) is defined as the region of the parameter space where the logarithm of the likelihood exceeds the maximum value decreased by $1/2$.

IV-B.4 The measurements

Phase Foxtrot

During phase Foxtrot the first good data after the completion of the filling of the inner vessel with scintillator were recorded (see also chapter III-C). The data taking length amounts to 34.8 d. A sample of 191 sequences was selected by means of the ML cuts.

The real time distribution of the candidate mass 212 sequences is shown in figure IV.5. The distribution has an exponential behaviour with a few days meanlife, indicating that the main contribution to the signal is background from mass 214 sequences.

The distribution of the energy of the candidates ^{212}Bi is shown in figure IV.6. The distribution is compatible with a mixture of mass 214 and mass 212 sequences. It is not very helpful in disentangling the two signal sources because the two expected distributions are very similar.

The distribution of the energy of the candidates ^{212}Po is shown in figure IV.7. The distribution shows very clearly that the predominant signal is from mass 214 sequences. The cluster of 11 events with energy of about 1.0 MeV may be compatible with signal from mass 212 sequences.

The distribution of the delay time is shown in figure IV.8. The count excess in the first two bins is compatible with the signal of about 10–15 mass 212 sequences. Still, the predominant signal is coming from mass 214 sequences.

The distribution of delay time versus energy of the candidates ^{212}Po is shown in figure IV.9. The pattern is similar to the one obtained in phase Golf. The belt of mass 214 sequences and a cluster of mass 212 sequences can be identified. From the distribution it can be argued that the signal of mass 212 sequences ranges from 10 to 15 counts.

The right number of mass 212 sequences is obtained from the likelihood analysis of the sample of candidate sequences, following the method described in section IV-B.3. The best estimates for the counts from each source are:

- $n_{212} = 10.8^{+3.8}_{-3.1}$
- $n_{214} = 178 \pm 14$
- $n_{\text{random}} = 2.0^{+2.7}_{\text{at limit}}$

the best estimate for n_{214} is compatible with the expected number of counts, which is known from the measurement of the counts of mass 214 sequences and amounts to 174. The best estimate for n_{random} is compatible with the expected number of counts which is zero. Considering the data taking length and the efficiency of the ML cuts, the best estimate for the mass 212 sequence count rate amounts to:

$$0.31^{+0.11}_{-0.09} \text{ counts/day} \quad (\text{IV.18})$$

and the best estimate for the ^{232}Th contamination is:

$$4.4^{+1.5}_{-1.2} \times 10^{-16} \text{ g/g} \quad (\text{IV.19})$$

Table IV.5 summarizes the results of the measurement on ^{232}Th contamination in phase Foxtrot.

Phase Lima

During phase Lima the first good data after the scintillator water extraction were recorded (see also chapter III-C). The data taking length unfortunately is very short and amounts to 6.4 d. A sample of 6 sequences was selected by means of the ML cuts.

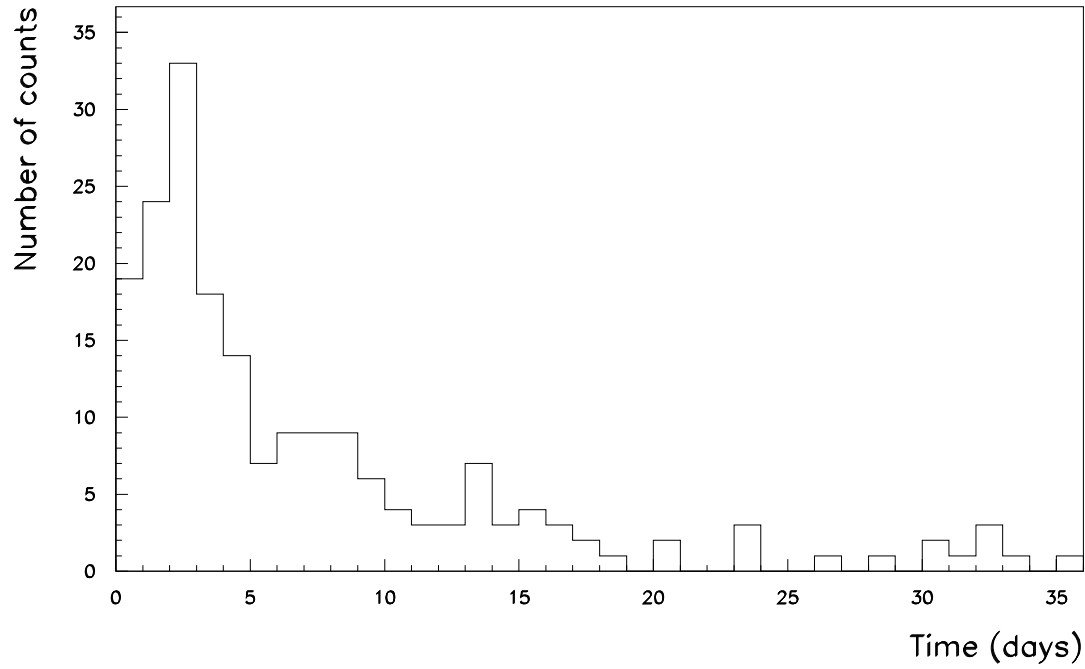


Figure IV.5: Phase Foxtrot.

Real time distribution for the sample of sequences selected by means of the M1 cuts.

The time is measured from the start of the data taking in phase Foxtrot.

The distribution has an exponential behaviour with a few days meanlife, indicating that the main contribution to the signal is background from mass 214 sequences. Departure from exponential behaviour in the first two bins is only apparent and it is due to a significant dead time in the first two days of data taking (the plot reports raw counts. No correction for dead time is performed).

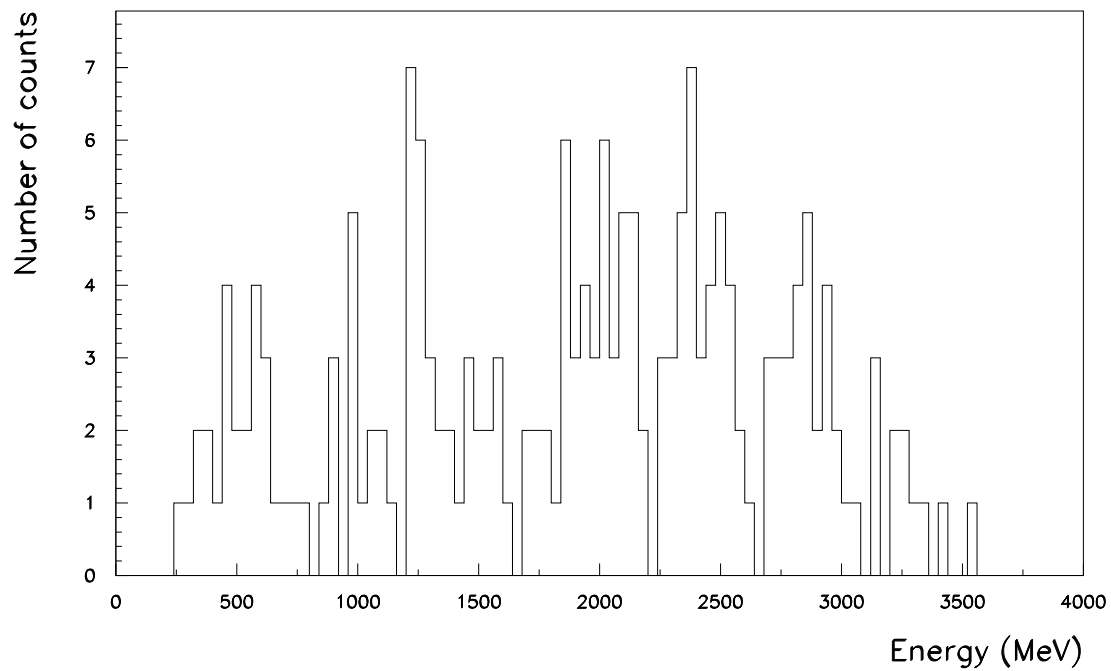


Figure IV.6: Phase Foxtrot.

Energy distribution for candidates ^{212}Bi in the sample of sequences selected by means of the Ml cuts. The distribution is compatible with a mixture of mass 214 and mass 212 sequences. It is not very helpful in disentangling the two signal sources because the two expected distributions are very similar.

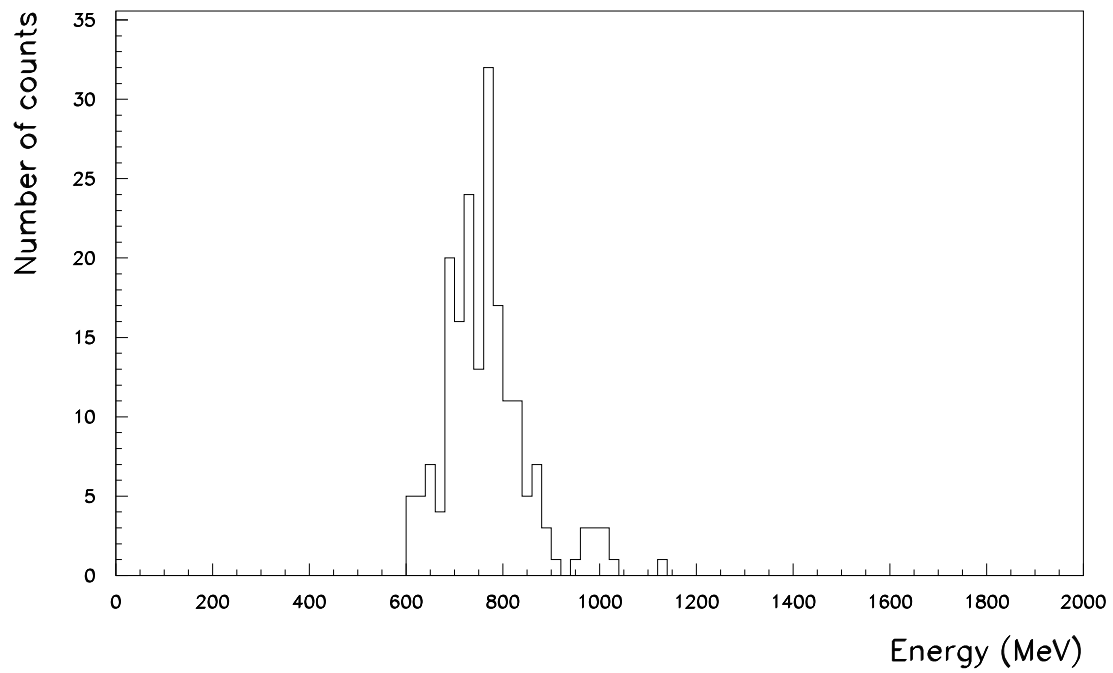


Figure IV.7: Phase Foxtrot.

Energy distribution for candidates ^{212}Po in the sample of sequences selected by means of the M1 cuts. The predominant signal is from mass 214 sequences. The cluster of 11 events with energy of about 1.0 MeV may be compatible with signals from mass 212 sequences.

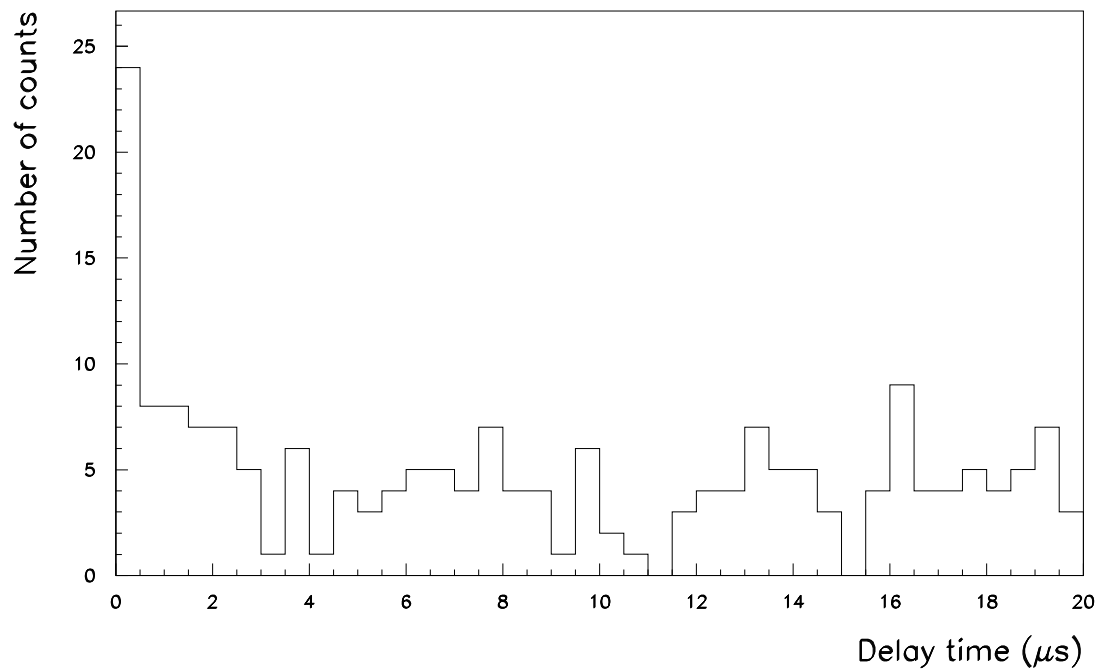


Figure IV.8: Phase Foxtrot.

Delay time distribution for the sample of sequences selected by means of the M1 cuts.

The count excess in the first two bins is compatible with the signal of about 10–15 sequences of mass 212.

Still, the predominant signal is coming from mass 214 sequences.

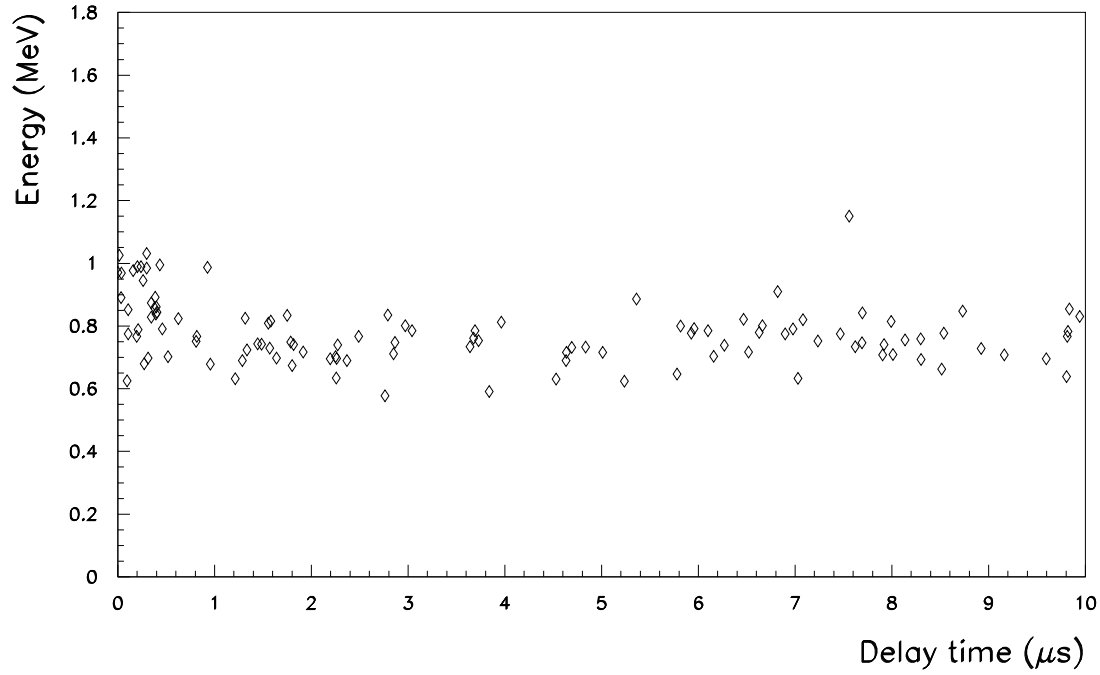


Figure IV.9: Phase Foxtrot.

Distribution of delay time versus energy for the candidates ^{212}Po in the sample of sequences selected by means of the MI cuts.

Three classes of events are identified: the bunch of mass 212 sequences having delay times lower than $1\ \mu\text{s}$ and energy of about 1.0 MeV; the belt of mass 214 sequences having delay times uniformly distributed and energy of about 0.8 MeV; a lonely and “spurious” event with delay time of about $7\ \mu\text{s}$ and energy of about 1.2 MeV.

From the distribution it can be argued that the number of mass 212 sequences ranges from 10 to 15.

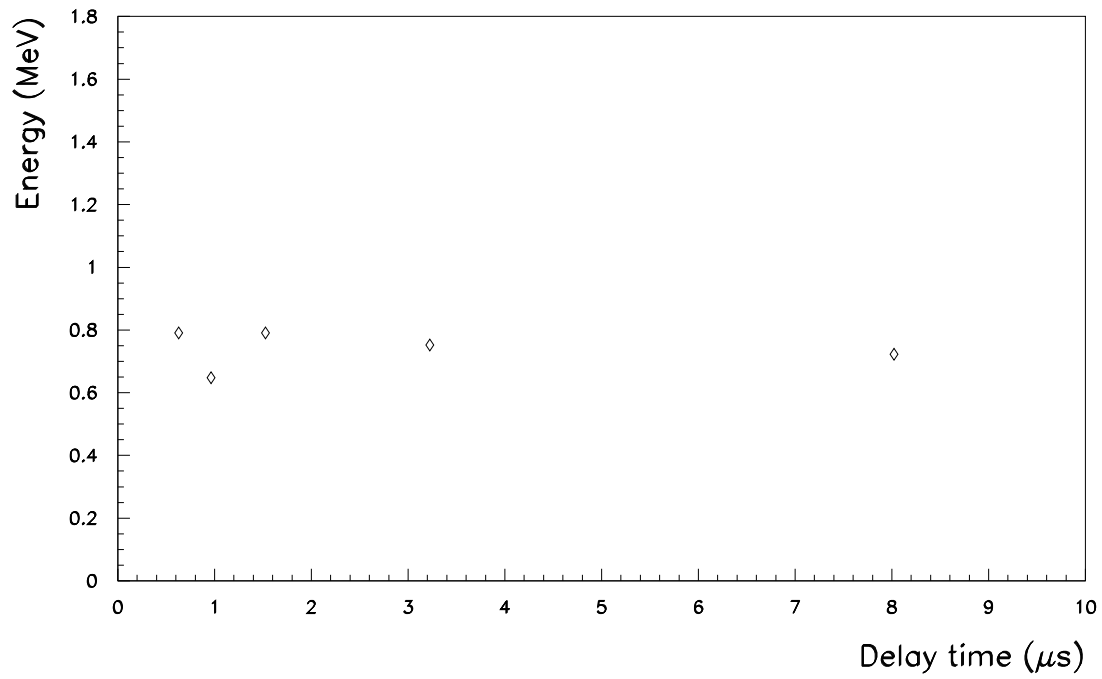


Figure IV.10: Phase Lima.

Distribution of delay time versus energy for the candidate ^{212}Po in the sample of sequences selected by means of the Ml cuts.

Only 5 sequences are shown because the sixth delay time exceeds $10 \mu s$. None of the signals is compatible with a signal from mass 212 sequences.

Table IV.5: Phase Foxtrot. Summary of the results on ^{232}Th contamination.

Phase Foxtrot		
	Measured	Expected
Data taking length [d]	34.8	
n_{212}	$10.8^{+3.8}_{-3.1}$	
n_{214}	178 ± 14	174
n_{random}	$2.0^{+2.7}_{\text{at limit}}$	0
^{232}Th contamination [g/g]	$4.4^{+1.5}_{-1.2} \times 10^{-16}$	

Table IV.6: Phase Lima. Summary of the results on ^{232}Th contamination.

Phase Lima		
	Measured	Expected
Data taking length [d]	6.4	
n_{212}	< 1.5 (1σ C.L.)	
n_{214}	$6.0^{+2.8}_{-2.1}$	8
n_{random}	< 1.5 (1σ C.L.)	0
^{232}Th contamination [g/g]	$< 3.3 \times 10^{-16}$ g/g at 1σ C.L. $< 4.1 \times 10^{-16}$ g/g at 90 % C.L.	

The distribution of delay time versus the energy of the candidates ^{212}Po is shown in figure IV.10. From the distribution it can be argued that none of the signals is compatible with signal coming from mass 212 sequences.

In absence of a signal from the mass 212 sequence, the likelihood analysis of the sample can give us an upper limit on the expected counts from mass 212 sequences. The best estimates for the counts from each source are:

- $n_{212} < 1.5$ at 1σ C.L.
- $n_{214} = 6.0^{+2.8}_{-2.1}$
- $n_{\text{random}} < 1.5$ at 1σ C.L.

the best estimate for n_{212} is compatible with the expected number of counts, which is known from the measurement of the counts of mass 214 sequences and amounts to 8. The best estimate for n_{random} is compatible with the expected number of counts which is zero. Considering the data taking length and the efficiency of the ML cuts, the best estimate for the mass 212 sequence activity amounts to:

$$< 0.23 \text{ counts/day at } 1\sigma \text{ C.L.} \quad (\text{IV.20})$$

and the best estimate for the ^{232}Th contamination is:

$$< 3.3 \times 10^{-16} \text{ g/g at } 1\sigma \text{ C.L.} \quad (\text{IV.21})$$

$$< 4.1 \times 10^{-16} \text{ g/g at } 90 \% \text{ C.L.} \quad (\text{IV.22})$$

Table IV.6 summarizes the results of the measurement on ^{232}Th contamination in phase Lima.

Phase Oscar

During phase Oscar the first good data after the scintillator distillation were recorded (see also chapter III-C). The data taking length amounts to 22.8 d. A sample of 77 events was selected by means of the ML cuts.

Unfortunately, during phase Oscar the TTR was broken and the digitalized waveshapes of the candidate mass 212 sequences were not available. The rejection of the fake coincidences due to muons crossing the inner

Table IV.7: Phase Oscar. Summary of the results on ^{232}Th contamination.

Phase Foxtrot		
	Measured	Expected
Data taking length [d]	22.8	
n_{212}	$12.3^{+4.0}_{-3.3}$	
n_{214}	64 ± 8	65
n_{random}	$1.0^{+2.1}_{\text{at limit}}$	0
^{232}Th contamination [g/g]	$8.0^{+2.6+0.0}_{-2.1-0.8} \times 10^{-16}$	

vessel was performed by means of a software cut: the energy of the first event of the candidate sequence was required to be lower than 4 MeV. This new cut was effective in rejecting fake coincidences. However, a check performed against the data of phase Foxtrot showed that the replacement of the TTR cut with the software cut introduces a systematic error of about 10^{-16} g/g: the estimate of the contamination in phase Foxtrot obtained with the cut replacement was $5.2^{+1.8}_{-1.5} \times 10^{-16}$ g/g. In order to account for the difference with the best estimate (obtained with the TTR cut) a systematic error of $^{+0.0}_{-0.8} \times 10^{-16}$ g/g was associated to the software cut replacing the TTR cut.

The distribution of delay time versus energy of the candidates ^{212}Po is shown in figure IV.10. The pattern is similar to the one obtained in phases Golf and Foxtrot. The belt of mass 214 sequences and a cluster of mass 212 sequences can be identified. From the distribution it can be argued that the signal of mass 212 sequences ranges from 10 to 15 counts.

The right number of mass 212 sequences is obtained from the likelihood analysis of the sample of candidate sequences, following the method described in section IV-B.3. The best estimates for the counts from each source are:

- $n_{212} = 12.3^{+4.0}_{-3.3}$
- $n_{214} = 64 \pm 8$
- $n_{\text{random}} = 1.0^{+2.1}_{\text{at limit}}$

the best estimate for n_{212} is compatible with the expected number of counts, which is known from the measurement of the counts of mass 214 sequences and amounts to 65. The best estimate for n_{random} is compatible with the expected number of counts which is zero. Considering the data taking length and the efficiency of the ML cuts, the best estimate for the mass 212 sequence activity amounts to:

$$0.54^{+0.18}_{-0.15} \text{ counts/day} \quad (\text{IV.23})$$

and the best estimate for the ^{232}Th contamination is:

$$8.0^{+2.6+0.0}_{-2.1-0.8} \times 10^{-16} \text{ g/g} \quad (\text{IV.24})$$

Table IV.7 summarizes the results of the measurement on ^{232}Th contamination in phase Oscar.

IV-C The ^{238}U contamination

IV-C.1 The sensitivity

The CTF measures the activity of ^{238}U chain in the scintillator by probing the rate of the daughter sequence $^{214}\text{Bi}(\beta)\text{-}^{214}\text{Po}(\alpha)$.

The ^{238}U chain is shown in figure IV.17. Because of possible breaking of the chain at the level of ^{226}Ra (meanlife of 2340 years), the measurement reports directly the ^{226}Ra contamination. For the sake of convenience the results will be quoted in terms of ^{238}U equivalent contamination as if the chain were in secular equilibrium.

The meanlife of ^{238}U amounts to 6.44×10^9 y. There are no branches in the chain.

Considering the meanlife of ^{238}U and the density of the scintillator, at the ^{238}U equivalent contamination level of 10^{-16} g/g the expected rate for the mass 214 sequences is 0.1 events/day/ton.

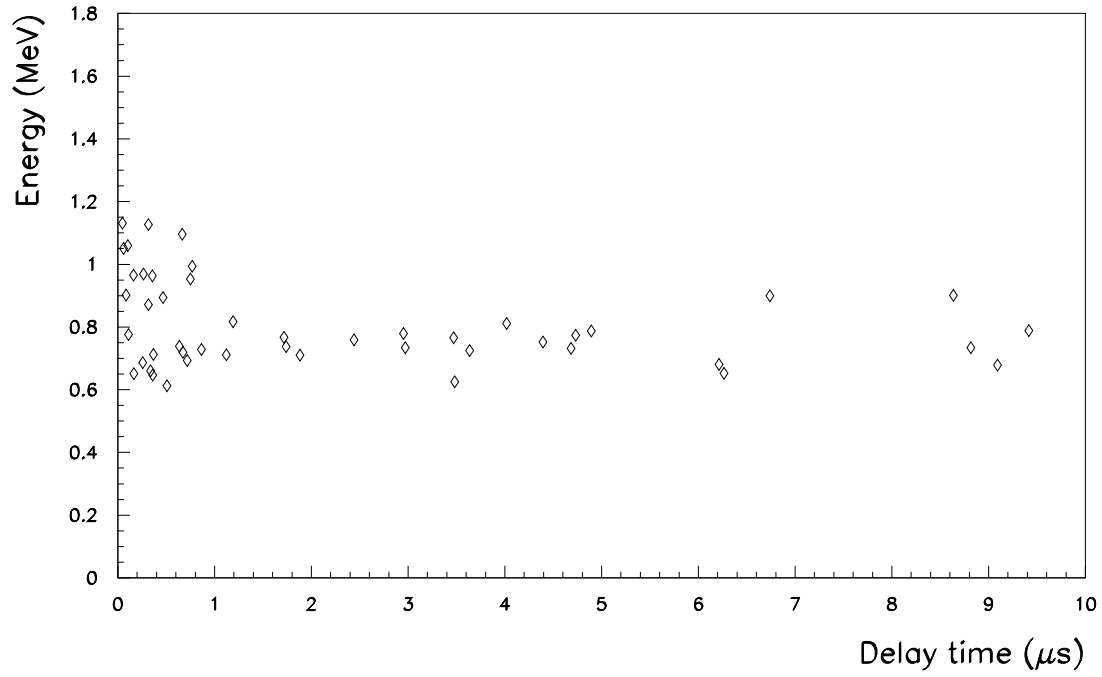


Figure IV.11: Phase Oscar.

Distribution of delay time versus energy for the candidates ^{212}Po in the sample of the sequences selected by means of the MI cuts.

Two classes of events are identified: the bunch of mass 212 sequences having delay times lower than $1\ \mu\text{s}$ and energy of about 1.0 MeV; the belt of mass 214 sequences having delay times uniformly distributed and energy of about 0.8 MeV.

From the figure it can be argued that the number of mass 212 sequences ranges from 10 to 15.

Table IV.8: Decay products, Q values, electron equivalent energies and meanlives for the mass 214 sequence nuclides.

Nuclide	Decay products	Q	Electron equivalent energy	Meanlife
		[MeV]	[MeV]	[s]
^{214}Bi	$\beta + \gamma$	3.20	$0 \rightarrow 3.20$	1.7×10^{-3}
^{214}Po	α	7.69	0.75	2.36×10^{-4}

Table IV.9: Efficiencies of the U cuts for the selection of the mass 214 sequences.

Cut	Efficiency (214)
Delay	0.80
Energy first event	0.97
Energy second event	0.98
Combined cuts	0.76

^{214}Bi decays into ^{214}Po emitting β and γ -rays with a meanlife of 28.4 m. The Q value amounts to 3.20 MeV. ^{214}Po decays into ^{210}Pb emitting an α particle with a meanlife of 236 μs . The Q value is 7.69 MeV and the electron equivalent energy is 751 KeV. The corresponding quenching value has been measured directly in the Munich experiment (see section IV-A.1). Table IV.8 resumes the physical characteristics of the two nuclides decays.

Selection of mass 214 sequences is performed by means of the following cuts, referred to as the U cuts:

- the delay between the two candidate events must lie in the range between 20 and 500 μs .

The lower limit removes the PMTs afterpulses.

The upper limit corresponds to two ^{214}Po meanlives.

The efficiency of the delay cut is 80 % for mass 214 sequences.

- the energy of the candidate ^{214}Bi must exceed 300 KeV.

Since 90% of the CTF spectrum is detected below the threshold of 300 KeV, the cut rejects 90 % of the random coincidences.

Moreover, the cut discards only 3 % of the good ^{214}Bi events because the ^{214}Bi energy spectrum is shifted to higher energies.

The efficiency of the ^{214}Bi energy cut is 97 % for mass 214 sequences.

- the energy of the candidate ^{214}Po must lie within 2σ from the mean value expected for ^{214}Po events.

This cut also helps in rejecting random coincidences.

Moreover, it discards only 2 % of the good ^{214}Po events.

The efficiency of the ^{214}Po energy cut is 98 % for mass 214 sequences.

The global efficiency of the combined U cuts amounts to 76 %. A summary of the efficiencies of the U cuts is reported in table IV.9.

The rate of random sequences surviving the U cuts amounts to:

$$r = r_1 \times r_2 \times \tau \quad (\text{IV.25})$$

$$= 10^{-1} \text{ s}^{-1} \times 10^{-2} \text{ s}^{-1} \times 5 \times 10^{-4} \text{ s} \quad (\text{IV.26})$$

$$= 5 \times 10^{-7} \text{ s}^{-1} \quad (\text{IV.27})$$

and it is negligible. The lowest measurable ^{238}U contamination in CTF is limited by the background coming from external and surface Radon sources, as it is discussed in section IV-C.2.

Table IV.10: Physical and chemical characteristics of Rn.

Fusion temperature	202 K
Boiling temperature	211 K
Critical temperature	377 K
Triple point temperature	202 K
Critical pressure	6.2 MPa
Triple point pressure	0.65 MPa
Density (gaseous STP)	$9.37 \times 10^3 \text{ g/cm}^3$
Density (liquid at boiling temperature)	4.4 g/cm^3
Diffusion coefficient in air	$0.1 \text{ cm}^2/\text{s}$

IV-C.2 Background from ^{222}Rn

Rn is a noble gas. It is chemically inert and has a great capacity of diffusion through matter. Table IV.10 resumes the main physical and chemical characteristics of Rn.

Rn isotopes are a big source of environmental radioactivity. Three isotopes give the main contribution to environmental Rn activity:

- ^{220}Rn belongs to ^{232}Th chain and has a meanlife of 78 s (see figure IV.15);
- ^{219}Rn belongs to ^{235}U chain and has a meanlife of 5.7 s (see figure IV.16);
- ^{222}Rn belongs to ^{238}U chain and has a meanlife of 5.49 d (see figure IV.17).

as far as diffusion is concerned, only the ^{222}Rn isotope is relevant since its meanlife is much greater than that of the other two isotopes.

^{222}Rn is produced by decay of ^{238}U and daughters. In the nylon of the inner vessel and in the water buffer ^{222}Rn is produced at a rate per unit volume much higher than in the scintillator, since the intrinsic ^{238}U contaminations of nylon and water are orders of magnitude higher than that of scintillator (see table II.5). ^{222}Rn from nylon can emanate into the scintillator, ^{222}Rn from water can permeate through nylon into the scintillator.

Diffusion of gases through isotropic and homogeneous media is governed by Fick's law:

$$\vec{J} + D\vec{\nabla}\rho = 0 \quad (\text{IV.28})$$

combining Fick's law with the continuity equation:

$$\vec{\nabla}\vec{J} + \partial_t\rho = 0 \quad (\text{IV.29})$$

the diffusion equation is obtained:

$$\partial_t\rho = D\nabla^2\rho \quad (\text{IV.30})$$

in the case of Rn, another term has to be added to the diffusion equation in order to account for Rn decay with the decay constant λ :

$$\partial_t\rho = D\nabla^2\rho - \lambda\rho \quad (\text{IV.31})$$

in the steady state case, the equation for Rn diffusion reduces to:

$$D\nabla^2\rho = \lambda\rho \quad (\text{IV.32})$$

Analytical solutions of the equation depend on the diffusion length defined as:

$$d = \sqrt{D/\lambda} \quad (\text{IV.33})$$

in one dimension, the general solution to the steady state equation is:

$$\rho(x) = Ae^{-x/d} + Be^{+x/d} + C \quad (\text{IV.34})$$

The formalism developed in this section can be specialized to derive the expressions for emanation and diffusion rates in the CTF and in the BX geometry.

Emanation

Let's suppose that the surface of separation between nylon ($x < 0$) and scintillator ($x > 0$) is at $x=0$. Let's suppose also that nylon thickness is much greater than diffusion length. Let's call B_{nylon} the ^{222}Rn activity per unit volume in nylon. The boundary conditions for the steady state equation are:

$$\rho(x) \rightarrow B_{\text{nylon}}/\lambda \text{ for } x \rightarrow -\infty \quad (\text{IV.35})$$

$$\rho(x) = 0 \text{ for } x > 0 \quad (\text{IV.36})$$

The solution is given by:

$$\rho(x) = B_{\text{nylon}}/\lambda \left(1 - e^{x/d}\right) \text{ for } x < 0 \quad (\text{IV.37})$$

and the flux of ^{222}Rn at the separation surface is:

$$J = -D \left(\frac{\partial \rho}{\partial x} \right) \Big|_{x=0-} = \frac{D}{\lambda d} B_{\text{nylon}} = dB_{\text{nylon}} \quad (\text{IV.38})$$

Calling R the radius of the inner vessel, the activity A_{eman} into the scintillator due to emanation is:

$$A_{\text{eman}} = J \times \text{Surface} = 4\pi R^2 dB_{\text{nylon}} \quad (\text{IV.39})$$

owing to the thumb rule that nylon contribution to ^{222}Rn activity into the inner vessel is equivalent to the activity of ^{222}Rn in a nylon shell of thickness d . Calling S_{nylon} and S_{scint} the nylon and the scintillator densities, the equivalent intrinsic contamination of the scintillator induced by emanation $U_{\text{scint}}^{\text{eman}}$ is related to the nylon intrinsic contamination U_{nylon} by:

$$U_{\text{scint}}^{\text{eman}} = \frac{\text{Surface}}{\text{Volume}} \times \frac{J}{B_{\text{nylon}}} \times \frac{S_{\text{nylon}}}{S_{\text{scint}}} \times U_{\text{nylon}} = \frac{3d}{R} \times \frac{S_{\text{nylon}}}{S_{\text{scint}}} \times U_{\text{nylon}} \quad (\text{IV.40})$$

Permeation

Let's call t the thickness of nylon. Let's suppose the separation surface between scintillator and nylon is located at $x = -t$ and the separation surface between nylon and scintillator is located at $x = 0$. Let's call B_{water} the ^{222}Rn activity per unit volume in water. The boundary conditions for the steady state equation are:

$$\rho(x) = B_{\text{water}}/\lambda \text{ for } x < -t \quad (\text{IV.41})$$

$$\rho(x) = 0 \text{ for } x > 0 \quad (\text{IV.42})$$

The ^{222}Rn concentration in nylon at the surface of separation with water is $SB_{\text{water}}/\lambda$, where S is the partition coefficient of Rn between water and nylon (called also relative solubility). The steady state equation must be solved for the interval $[-t, 0]$ and the left and right boundary conditions are respectively $SB_{\text{water}}/\lambda$ and 0. The solution is:

$$\rho(x) = -\frac{S \sinh(x/d)}{\lambda \sinh(t/d)} B_{\text{water}} \quad (\text{IV.43})$$

the flux at the scintillator surface is:

$$J = -D \left(\frac{\partial \rho}{\partial x} \right) \Big|_{x=0-} = DS \frac{t/d}{\sinh(t/d)} \times \frac{1}{\lambda t} \times B_{\text{water}} = \frac{P_{\text{eff}}}{\lambda t} B_{\text{water}} \quad (\text{IV.44})$$

$$P_{\text{eff}} = DS \frac{t/d}{\sinh(t/d)} \quad (\text{IV.45})$$

P_{eff} is the effective permeability of the membrane. Let's consider the case $\Theta_m t/d \ll 1$. The time lag, defined in the literature [W⁺91] as the time needed for ^{222}Rn to cross the nylon membrane, is much lower than the ^{222}Rn meanlife:

$$\frac{t^2}{6D} \ll \frac{1}{\lambda} \quad (\text{IV.46})$$

it follows that the fraction of ^{222}Rn decaying while crossing the membrane is negligible. In this case P_{eff} is equal to the ordinary permeability:

$$P_{\text{eff}} \simeq P = DS \quad (\text{IV.47})$$

Otherwise, if $t/d > 1$, P_{eff} is lower than the ordinary permeability owing to the loss of ^{222}Rn nuclides decaying while crossing the nylon.

The ^{222}Rn activity induced by permeation in the scintillator A_{perm} is:

$$A_{\text{perm}} = J \times \text{Surface} = 4\pi R^2 \frac{P_{\text{eff}}}{t} B_{\text{water}} \quad (\text{IV.48})$$

calling S_{water} the water density, the equivalent intrinsic contamination of the scintillator induced by permeation $U_{\text{scint}}^{\text{perm}}$ is related to the intrinsic contamination of the water U_{water} by:

$$U_{\text{scint}}^{\text{perm}} = \frac{\text{Surface}}{\text{Volume}} \times \frac{J}{B_{\text{water}}} \times \frac{S_{\text{water}}}{S_{\text{scint}}} \times U_{\text{nylon}} = \frac{3P_{\text{eff}}}{R\lambda t} \times \frac{S_{\text{water}}}{S_{\text{scint}}} \times U_{\text{water}} \quad (\text{IV.49})$$

It is noteworthy that the emanation rate depends on the partition coefficient between water and nylon, but it does not depend on the partition coefficient between nylon and scintillator.

The measurement of the diffusion coefficient for wet nylon

The diffusion and the partition coefficient for Rn in dry nylon are very well known from laboratory measurements performed at Cracow University. The best estimate for the nylon in air are (see reference [Woj97]):

$$D = 1.0 \times 10^{-12} \text{ cm}^2/\text{s} \quad (\text{IV.50})$$

$$S = 5.5 \quad (\text{IV.51})$$

However, wet nylon is a material very different from dry nylon. Nylon internal bonds are attacked and weakened by water polar bonds. After a long contact with water, the mechanical characteristics of nylon are modified. The changes in the mechanical characteristics are produced in a characteristic time scale of several months. In absence of specific measurements, the diffusion and the partition coefficients for wet nylon were measured directly in CTF. The measurement was performed exploiting the data recorded in the radon-in-water test performed during phase Quebec. At the beginning of the test a huge increase of the ^{222}Rn density in the water buffer was provoked by the insertion of five tons of water purified but not stripped with nitrogen. The nominal ^{222}Rn activity of the water inserted was of about 1000 Bq/m^3 and the average content of ^{222}Rn in the water buffer after the insertion was of about 5 Bq/m^3 . The trigger rate grew up to 20 Hz and the signal from ^{222}Rn in the water buffer was the predominant source of background along the whole energy spectrum.

The activity of ^{222}Rn and daughters in the external water was monitored by measuring the counts in the energy window between 1.5 and 2.7 MeV (called also the external Rn window because in the ordinary data taking phases the major sources of signal in that window were γ -rays emitted by the ^{222}Rn daughter ^{214}Bi present in water and cosmic rays). Figure IV.12 shows the measured count rate in the external Rn window for a period of 40 days starting from the beginning of phase Quebec. The distribution is fitted with a constant plus an exponential with meanlife fixed at the ^{222}Rn meanlife. The fit shows that external Rn is the predominant source of background for over 25 days in the external Rn window.

Figure IV.13 shows the count rate for mass 214 sequences selected by means of the U cuts. The values of the diffusion and of the partition coefficient can be extracted directly from this distribution, as it is discussed below.

Let's consider in a first approximation the case for $t/d \ll 1$. Remembering that $P_{\text{eff}} \simeq P$, the time variation of the number of ^{222}Rn nuclides present in the inner vessel can be approximated by:

$$\frac{dn}{dT} = -\lambda n + A + 4\pi R^2 \frac{P}{\lambda t} \text{Be}^{-\lambda T} \quad (\text{IV.52})$$

where A (dimension of $[\text{s}^{-1}]$) is the constant ^{222}Rn activity in the scintillator due to internal ^{238}U contamination, to emanation of ^{222}Rn from nylon and to permeation of a constant activity of ^{222}Rn in water (due to ^{238}U or ^{226}Ra contamination either in water or in the constructing material); $\text{Be}^{-\lambda T}$ (dimension of $[\text{cm}^{-3}\text{s}^{-1}]$) is the transient activity of ^{222}Rn in water due to the provoked insertion of non-stripped water. Integrating from the start time with the boundary condition $n(\infty) = A/\lambda$, the solution is obtained:

$$n(T) = \frac{A}{\lambda} + 4\pi R^2 \frac{P}{\lambda t} \text{Be}^{-\lambda T} T \quad (\text{IV.53})$$

an approximate value of P can be derived by fitting the real time distribution of the mass 214 sequences rate with the above function while keeping A and B as free parameters (see figure IV.13):

$$P = DS = 15 \times 10^{-10} \text{ cm}^2/\text{s} \quad (\text{IV.54})$$

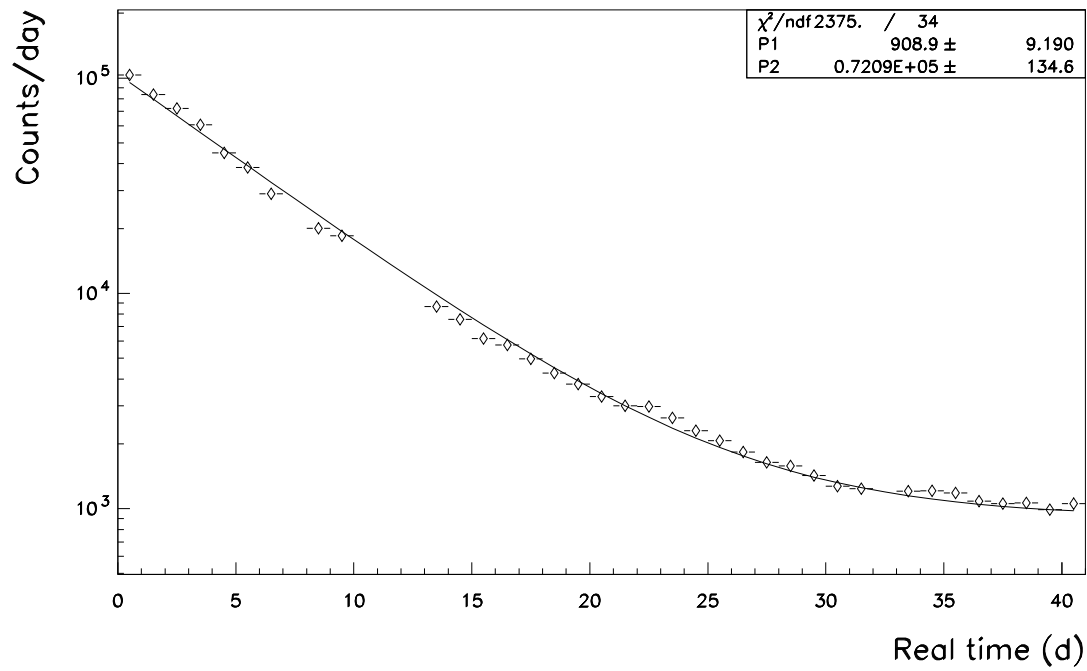


Figure IV.12: Phase Quebec.

Count rate in the external Rn window (1.5–2.7 MeV).

The count rate is shown for a period of 40 days starting from the beginning of phase Quebec.

Dead time in the acquisition is corrected for.

The distribution is fitted with a constant plus an exponential with meanlife fixed at the ^{222}Rn meanlife. The fits shows that external Rn is the predominant source of background for over 25 days in the external Rn window.

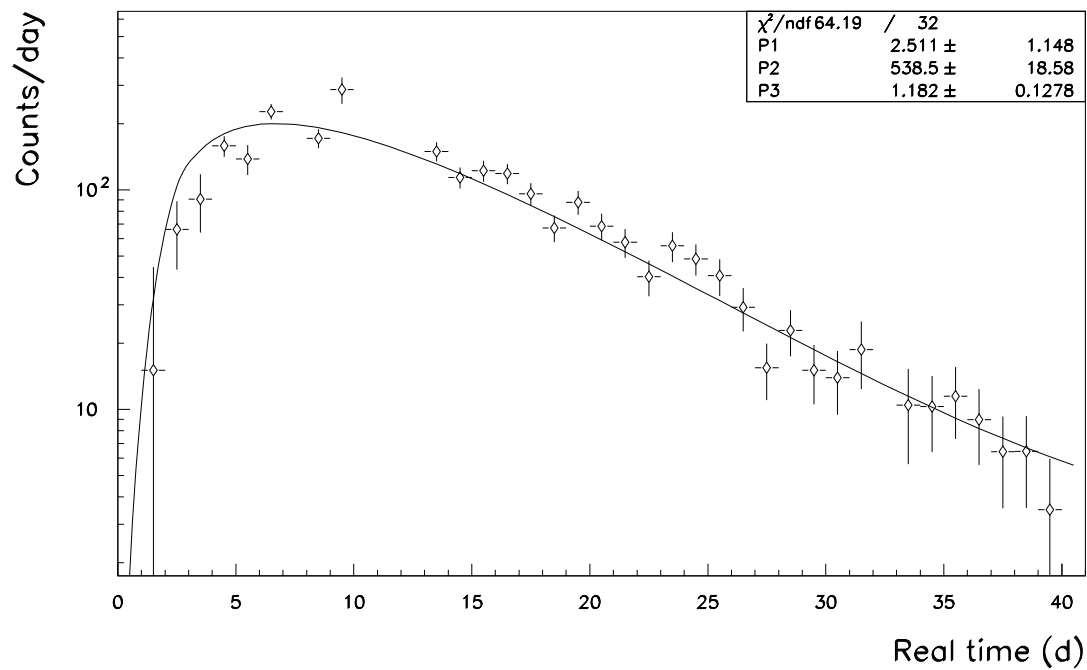


Figure IV.13: Phase Quebec.

Count rate for mass 214 sequences selected by means of the U cuts.

The count rate is shown for a period of 40 days starting from the beginning of phase Quebec.

Dead time in the acquisition is corrected for.

The distribution is fitted with the function described in equation IV.53 to derive the value of the permeability.

A further attempt to analyze the same data has been tried by Laura Cadonati, a Princeton student. Leaving the hypothesis $t/d \ll 1$, the general solution is a non-analytical function given by a series of analytical functions. Fitting the data with the solution calculated by a computer allows to derive both the values of D and S:

$$D = 6 \times 10^{-10} \text{ cm}^2/\text{s} \quad (\text{IV.55})$$

$$S = 5 \quad (\text{IV.56})$$

these are the best estimate for D and S at the time of phase Quebec.

From these results the values of the effective permeability and of the diffusion length at the time of phase Quebec can be derived.

$$d \simeq 170 \text{ } \mu\text{m} \quad (\text{IV.57})$$

$$t/d \simeq 3 \quad (\text{IV.58})$$

$$P_{\text{eff}} = 10 \times 10^{-10} \text{ cm}^2/\text{s} \quad (\text{IV.59})$$

The best estimate for the Uranium content into the inner vessel results from laboratory measurements of nylon samples and it is (see table II.5):

$$U_{\text{nylon}} = 2 \times 10^{-12} \text{ g/g} \quad (\text{IV.60})$$

From this estimate and from the value of nylon density ($S_{\text{nylon}}=1.1 \text{ g/cm}^3$) it can be argued that the best estimate for the equivalent intrinsic contamination due only to emanation $U_{\text{scint}}^{\text{eman}}$ is:

$$U_{\text{scint}}^{\text{eman}} = 8 \times 10^{-16} \text{ g/g} \quad (\text{IV.61})$$

It was shown (see chapter V for the derivation) that the best estimate for the ^{222}Rn activity in the water buffer is 30 mBq/m^3 . From this estimate, the best estimate for the equivalent intrinsic contamination due only to permeation $U_{\text{scint}}^{\text{perm}}$ is:

$$U_{\text{scint}}^{\text{perm}} = 2 \times 10^{-16} \text{ g/g} \quad (\text{IV.62})$$

IV-C.3 The measurement of ^{238}U contamination

While measuring the scintillator intrinsic ^{238}U contamination by probing the rate of mass 214 sequences, the transient ^{222}Rn contamination produced by the scintillator processing operations must be disentangled from the intrinsic ^{238}U contamination. The former is expected to decay with the ^{222}Rn lifetime while the latter will remain constant.

In order to disentangle the two contributions, it is necessary that the data taking length were long enough to allow the transient ^{222}Rn contamination to decay at levels of 1–2 counts/day. The only data taking phase long enough for the evaluation of the intrinsic ^{238}U contamination is phase Foxtrot. During phase Foxtrot the first good data after the completion of the filling of the inner vessel with scintillator were recorded (see also chapter III-C). The data taking length amounts to 34.8 d.

The ^{222}Rn coming either from emanation or from permeation is a background source for the measurement of the internal contamination. Moreover, the background from emanation and permeation is time dependent since it is related to the value of the effective permeability. Phase Foxtrot dates back six months before phase Quebec: therefore the background from emanation and permeation is not precisely determined, but we can guess that it amounts to a few 10^{-16} g/g . Consequently the contamination measured in phase Foxtrot can be quoted only as an upper limit.

Figure IV.14 shows the rate of mass 214 sequences selected via U cuts. The rate is corrected for dead time in the data acquisition. The distribution is fitted using an exponential with ^{222}Rn meanlife plus a constant function in order to disentangle the transient ^{222}Rn contamination from the internal intrinsic ^{238}U contamination (it is noteworthy that if allowed to vary, the meanlife is consistent with ^{222}Rn meanlife). The best fit estimate of the constant contribution amounts to:

$$1.5 \pm 0.6 \text{ counts/day} \quad (\text{IV.63})$$

which corresponds for the ^{238}U contamination to the upper limit:

$$< (3.5 \pm 1.3) \times 10^{-16} \text{ g/g } (1\sigma) \quad (\text{IV.64})$$

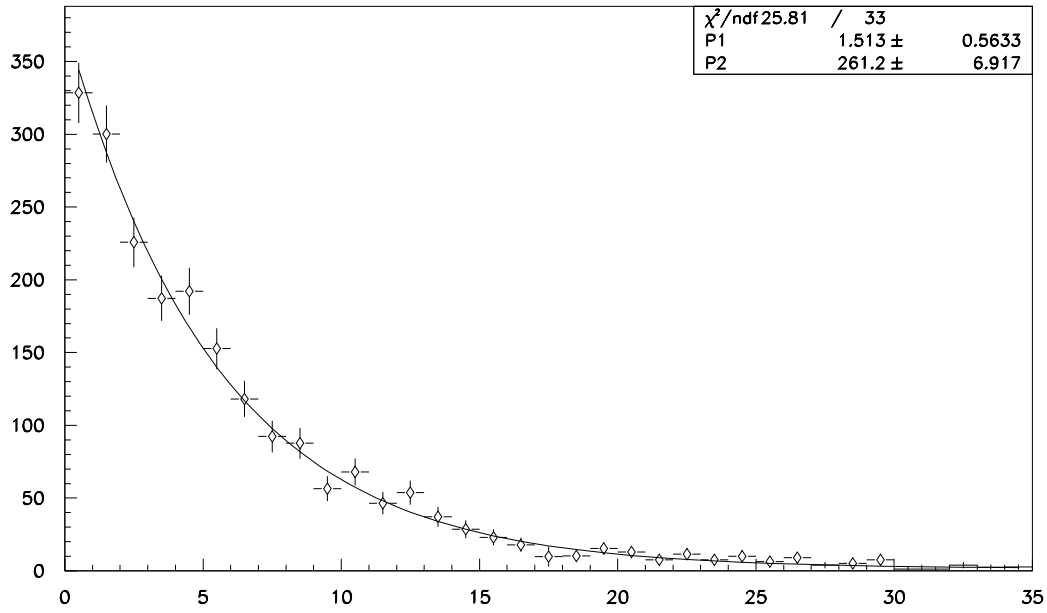


Figure IV.14: Phase Foxtrot.

Rate of mass 214 sequences selected by means of the U cuts.

The rate is corrected for dead time in data acquisition.

The distribution is fitted using an exponential with ^{222}Rn meanlife plus a constant function in order to disentangle the transient ^{222}Rn contamination from the internal intrinsic ^{238}U contamination. If allowed to vary, the meanlife is consistent with ^{222}Rn meanlife.

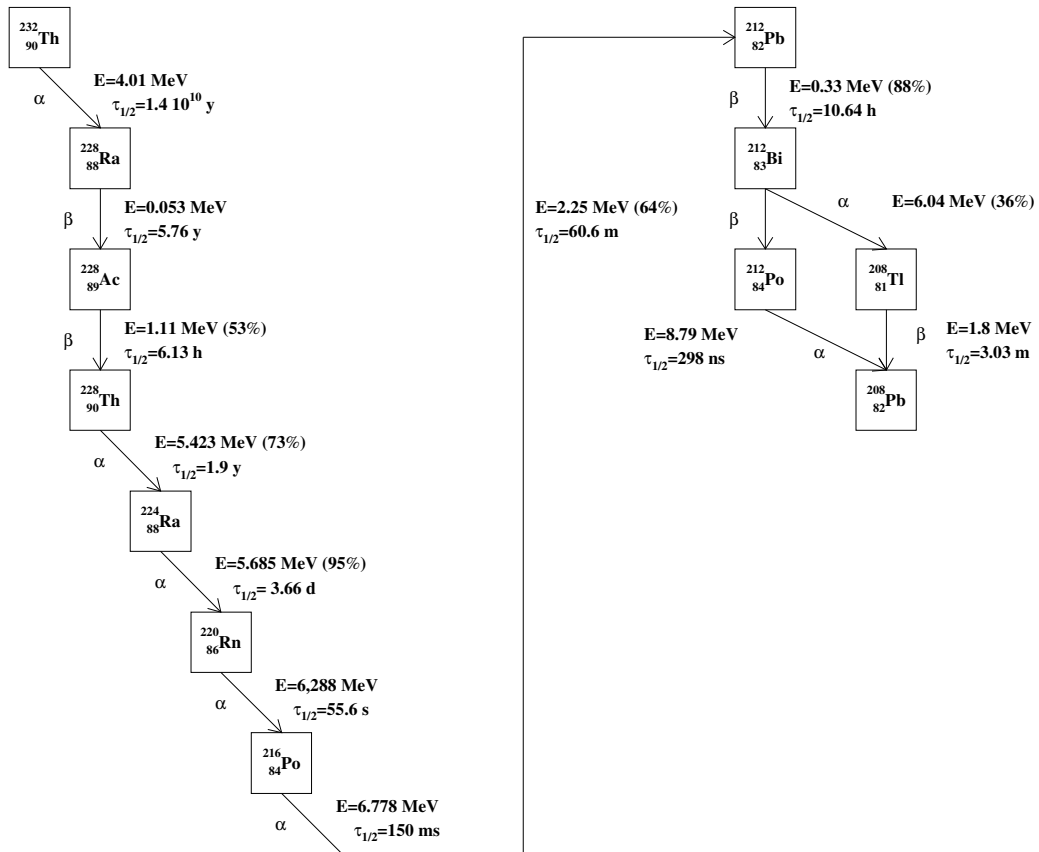


Figure IV.15: The ^{232}Th radioactive chain.

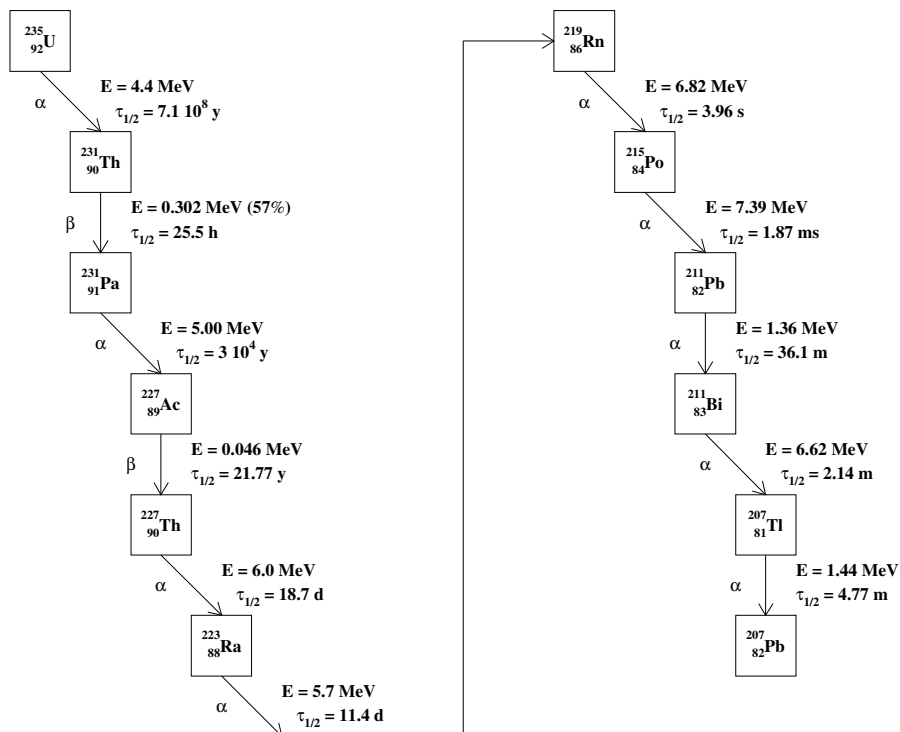


Figure IV.16: The ^{235}U radioactive chain.

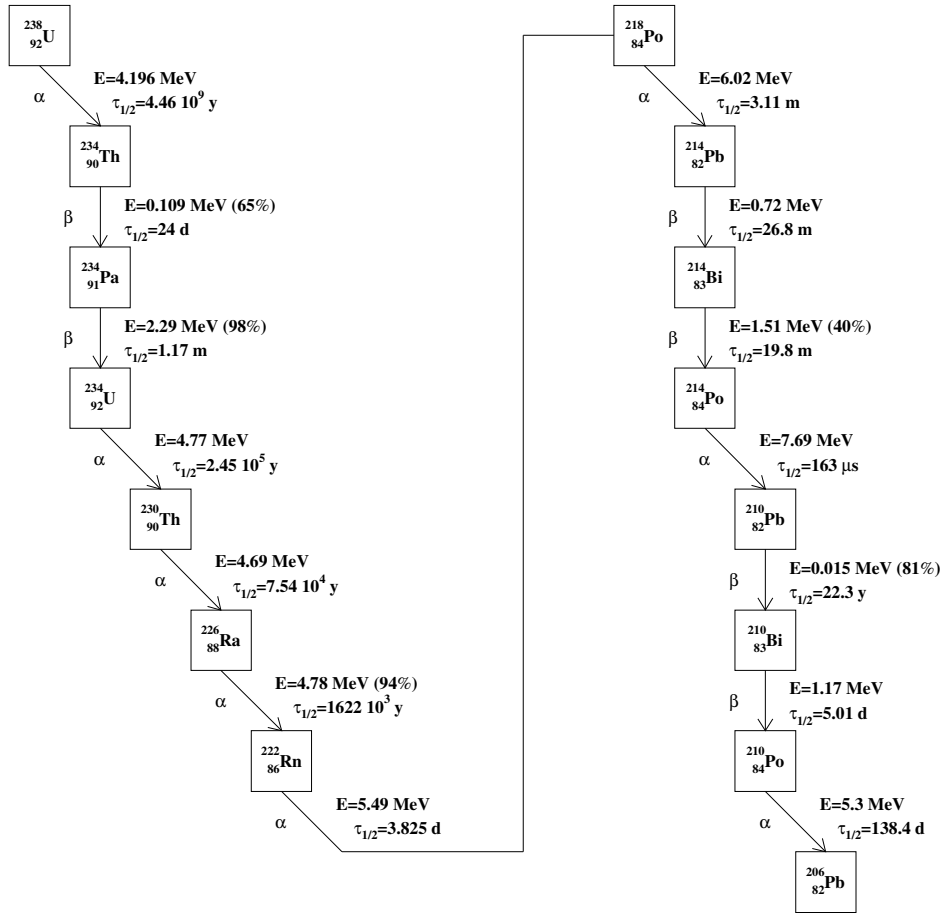


Figure IV.17: The ^{238}U radioactive chain.

IV-D The ^{85}Kr contamination

IV-D.1 The sensitivity

Owing to the initial presence of ^{222}Rn it was known from the beginning of CTF that a certain amount of air mixed with the scintillator. In march 1995, a very insightful hint came from F.X. Hartmann and from R.S. Raghavan, who suggested to look for fall-out radioactive gases and specifically for ^{85}Kr .

Krypton is a noble gas. The ^{85}Kr nuclide is not present in nature. Its meanlife amounts to 10.7 years. It is present in the atmosphere because it is produced by nuclear fission in nuclear reactors. The activity of ^{85}Kr in central Europe is of about 1 Bq/m³.

^{85}Kr decays into ^{85}Rb emitting a β particle with a 99.57 % branching ratio. The Q value of the reaction amounts to is 687 KeV.

For the remaining 0.43 % branching ratio, ^{85}Kr decays into the metastable state $^{85\text{m}}\text{Rb}$ emitting a β particle whose maximum kinetic energy is 173 KeV. $^{85\text{m}}\text{Rb}$ has a meanlife of 1.46 μs and decays in the ground state ^{85}Rb emitting a γ ray with energy of 514 KeV.

The signal from ^{85}Kr can be disentangled from the other background sources looking for the delayed coincidences provided by the lower branching ratio decay channel. The two decaying nuclides involved are ^{85}Kr and $^{85\text{m}}\text{Rb}$ and the two signals come respectively from β and γ decay. The sequence will be referred to as mass 85 sequence.

Mass 85 sequences have four signatures:

- the expected real time distribution is uniform owing to the long ^{85}Kr meanlife;
- the expected distribution of delay time between the first and the second event of the sequence is an exponential with meanlife equal to the $^{85\text{m}}\text{Rb}$ meanlife;
- the energy spectrum expected for the first events is a β spectrum with highest energy at 173 KeV;
- the energy spectrum expected for the second events is peaked around the γ -ray energy of 514 KeV.

Mass 85 sequences are selected by means of the following set of cuts:

- the delay between the two candidate events must lie in the range between 0.1 μs and 5 μs .

The lower limit of the delay window is fixed in analogy with the value of the same quantity in the Th cuts.

The upper limit is three times the $^{85\text{m}}\text{Rb}$ meanlife.

The efficiency of the delay time cut is 90 % for mass 85 sequences.

- the energy of the candidate first event must be lower than 300 KeV.

The value of 300 KeV is 4σ above the maximum energy for ^{85}Kr decay into $^{85\text{m}}\text{Rb}$.

A relevant fraction of the spectrum for ^{85}Kr decaying in $^{85\text{m}}\text{Rb}$ lies below the energy threshold.

The combined efficiency of the ^{85}Kr energy cut and of the hardware trigger threshold is 79 %.

- the energy of the candidate $^{85\text{m}}\text{Rb}$ must be lower than 700 KeV.

Since the expected mean energy is 514 KeV and standard deviation amounts to 60 KeV, the upper limit of the energy window is 3σ higher than the mean expected value.

The efficiency of the $^{85\text{m}}\text{Rb}$ energy cut is 99 %.

The global efficiency of the combined Kr cuts amounts to 70 %. A summary of the efficiencies of the Kr cuts is reported in table IV.11.

The rate of random sequences surviving the Kr cuts amounts to:

$$r = r_1 \times r_2 \times \tau \quad (\text{IV.65})$$

$$= 1 \text{ s}^{-1} \times 1.5 \times 10^{-1} \text{ s}^{-1} \times 6 \times 10^{-6} \text{ s} \quad (\text{IV.66})$$

$$= 10^{-6} \text{ s}^{-1} \quad (\text{IV.67})$$

and it is not negligible.

The lowest measurable rate of mass 85 sequences in CTF is limited by the random background rate and it amounts to 0.1 counts/day. This limit corresponds to 4×10^{-4} Bq or 35 events/day for the total ^{85}Kr activity in the inner vessel.

Table IV.11: Efficiencies of the Kr cuts for the selection of the mass 85 sequences.

Cut	Efficiency (85)
Delay	0.90
Energy first event	0.79
Energy second event	0.99
Combined cuts	0.70

IV-D.2 The measurement

Phase Foxtrot

During phase Foxtrot the first good data after the completion of the filling of the inner vessel with scintillator were recorded (see also chapter III-C). The data taking length amounts to 34.8 d. A sample of 38 mass 85 sequences was selected by means of the Kr cuts.

The real time distribution of the candidate mass 85 sequences is shown in figure IV.18. It is compatible with a flat distribution as expected for a ^{85}Kr signal.

The distribution of the energy of the candidate first events is shown in figure IV.19. The distribution is compatible with that of a β spectrum with end point at 173 KeV as expected for a ^{85}Kr signal.

The distribution of the energy of the candidate the second event energies is shown in figure IV.20. The distribution is compatible with that of a γ -ray line spectrum peaked around the energy of 514 KeV as expected for a ^{85}Kr signal.

The distribution of the delay time is shown in figure IV.21. The distribution is compatible with an exponential of $1.45 \mu\text{s}$ meanlife as expected for a ^{85}Kr signal.

In order to evaluate the number of candidate sequences to be attributed to ^{85}Kr activity, a Likelihood analysis has been performed in analogy with the analysis described in section IV-B.3. The results of the Likelihood analysis are:

- $n_{85} = 37 \pm 6$
- $n_{\text{random}} < 1.5$ at 1σ C.L.

the best estimate for the rate of mass 85 sequences detected amounts to (1.1 ± 0.2) counts/day. Considering the ^{85}Kr branching ratios and the efficiency of the Kr cuts the best estimate for the ^{85}Kr total activity in the inner vessel amounts to $(4.4 \pm 0.6) \times 10^{-3}$ Bq or (389 ± 70) counts/day.

Phase Lima

During phase Lima the first good data after the scintillator water extraction were recorded (see also chapter III-C). The data taking length unfortunately is very short and amounts to 6.4 d.

The analysis of the data collected in phase Lima shows no evidence for ^{85}Kr signal.

The upper limit for ^{85}Kr activity in phase Lima amounts to 50 counts/day at 90 % C.L..

Phase Oscar

During phase Oscar the first good data after the scintillator distillation were recorded (see also chapter III-C). The data taking length amounts to 22.8 d.

The analysis of the data collected in phase Oscar shows no evidence for ^{85}Kr signal.

The upper limit for ^{85}Kr activity in phase Oscar amounts to 35 counts/day at 90 % C.L..

IV-E The neutrons produced by cosmic rays

In CTF neutrons are produced in nuclear reactions by ultrarelativistic muons crossing the detector. A nuclear cascade can give rise either to a single or to a multiple neutrons production. The flux of muons in the Gran Sasso Laboratory is of about $1 \text{ particle/m}^2/\text{h}$.

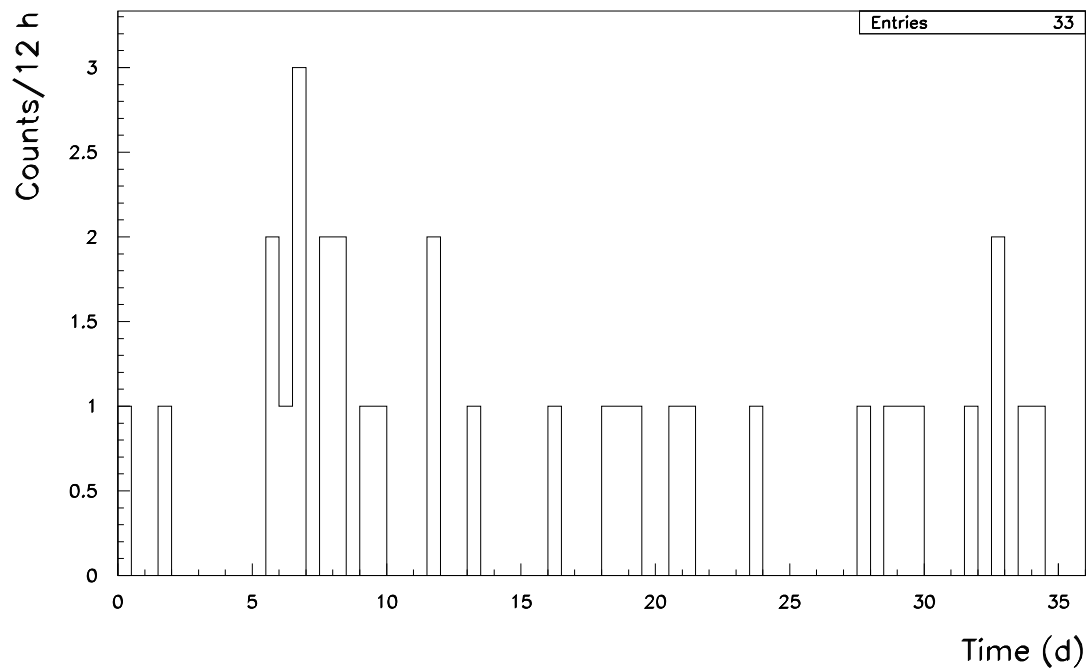


Figure IV.18: Phase Foxtrot.

Real time distribution for the sample of sequences selected by means of the Kr cuts.

The time is measured from the start of the data taking in phase Foxtrot.

The distribution is compatible with a flat distribution as expected for a ^{85}Kr signal.

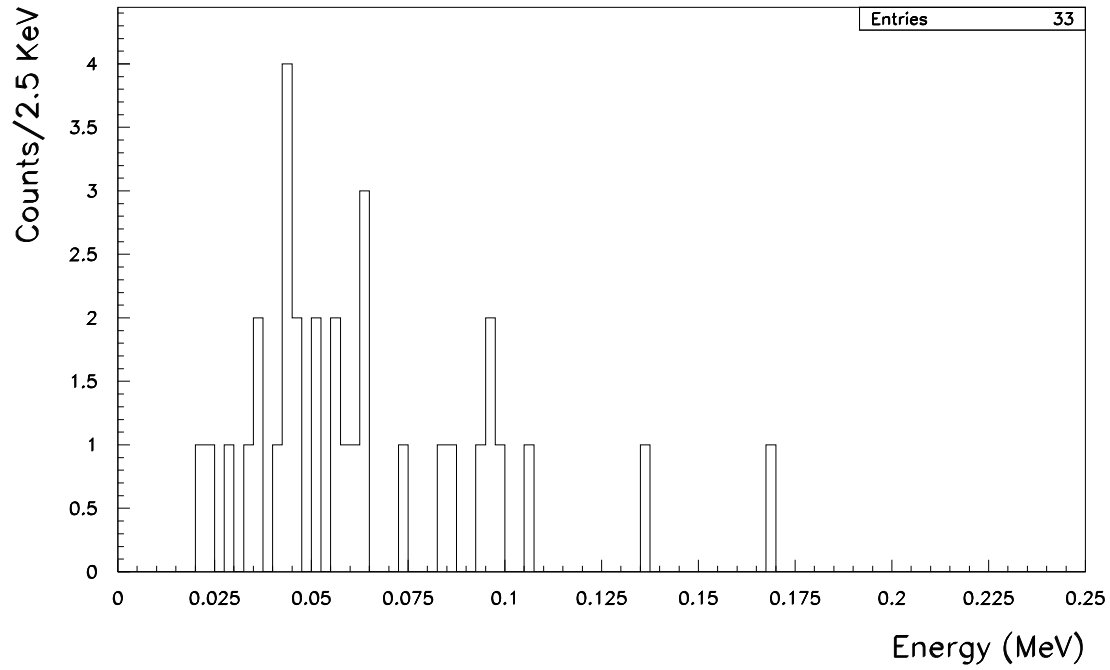


Figure IV.19: Phase Foxtrot.

Energy distribution for the candidate first events in the sample of the sequences selected by means of the Kr cuts.

The distribution is compatible with that of a β spectrum with end point at 173 KeV as expected for a ^{85}Kr signal.

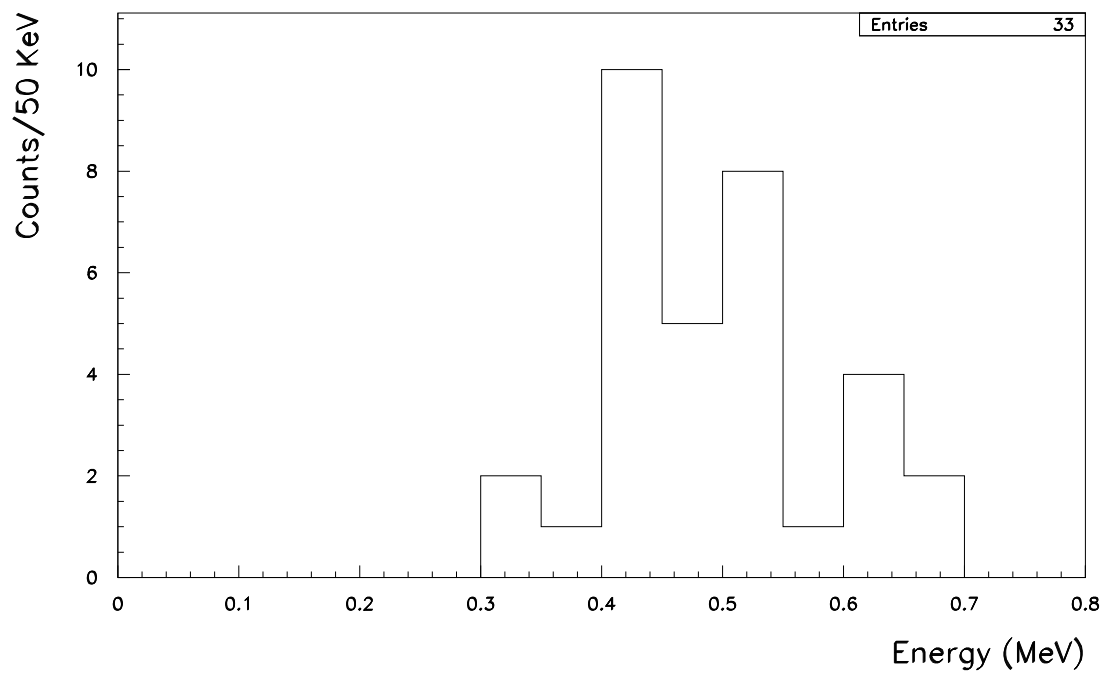


Figure IV.20: Phase Foxtrot.

Energy distribution for the candidate ^{85m}Rb in the sample of the sequences selected by means of the Kr cuts. The distribution is compatible with that of a γ -ray line spectrum peaked around the energy of 514 KeV as expected for a ^{85}Kr signal.

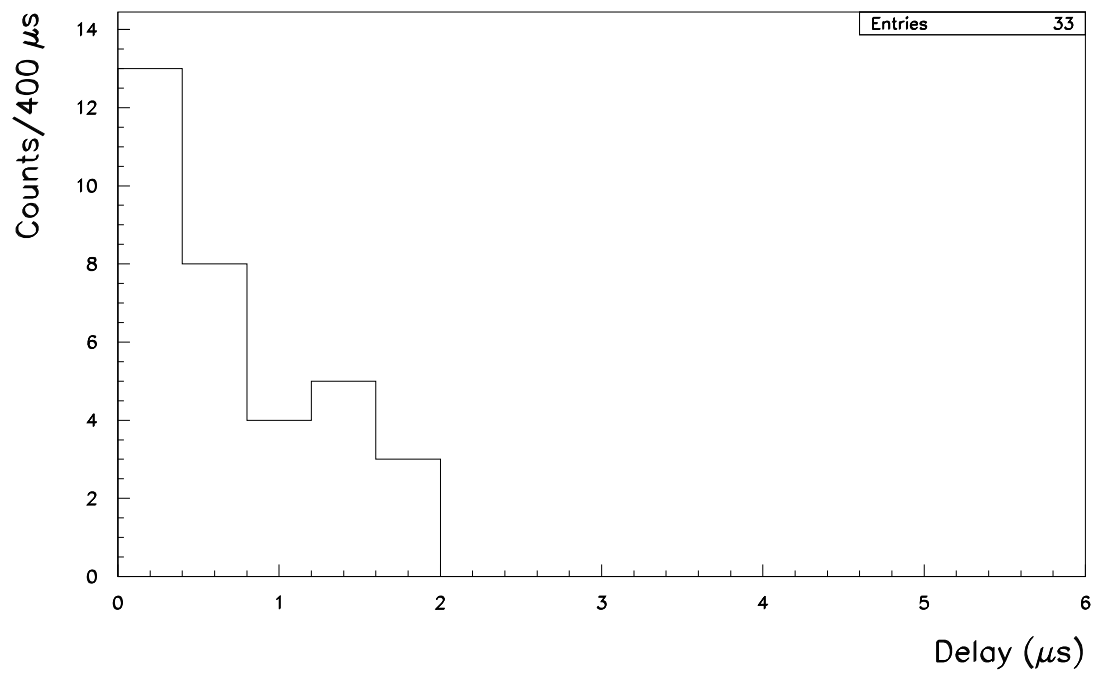


Figure IV.21: Phase Foxtrot.

Delay time distribution for the sample of sequences selected by means of the Kr cuts.

The distribution is compatible with an exponential of $1.45 \mu\text{s}$ meanlife as expected for a ^{85}Kr signal.

Table IV.12: Physical quantities determining the mean capture time of thermal neutrons in water and in PC.

	Water	PC
Molecular weight	18	120
Hydrogen atoms per molecule	2	12
Hydrogen mass fraction [%]	12	10
Density [g/cm ³]	1.00	0.86
n [cm ⁻³]	7.2×10^{22}	5.1×10^{22}
τ [μ s]	220	300

The CTF measures directly the number of muon induced nuclear cascades producing neutrons. It does not measure the number of neutrons produced because the electronics can keep track of only one delayed coincidence. Possible other coincidences are not recorded.

Neutrons produced either in the scintillator or in the water are thermalized primarily by elastic interactions with the hydrogen atoms (see reference [Fer49]). Thermal neutrons are captured by hydrogen in the reaction:



The γ -ray energy is 2.19 MeV. Calling v is the velocity of thermal neutrons, the capture cross section in the thermal energies range is (see [Fer49]):

$$\sigma_{(n,\gamma)} = \frac{6.4 \times 10^4 \text{ barns} \times \text{cm}}{v \quad s} \quad (\text{IV.69})$$

Calling n the proton density, the mean capture time τ of neutrons is:

$$\tau = \frac{1}{\sigma n v} = \frac{1.6 \times 10^{19} \text{ s}}{n \quad \text{cm}^3} \quad (\text{IV.70})$$

table IV.12 reports the physical quantities determining the mean capture time of neutrons in scintillator and in water:

- $\tau_{\text{PC}} = 300 \mu\text{s}$
- $\tau_{\text{water}} = 220 \mu\text{s}$

Neutrons give rise to a delayed coincidence between the combined signal of the muon and of the nuclear cascade on one hand and the neutron capture γ -ray on the other hand. Candidate neutron sequences are selected using the following set of cuts, referred to as the neutron cuts:

- the delay between the two candidate events must lie in the range between 10 μs and 2 ms.

The upper limit of the range amounts to more than 5 neutron meanlives.

The efficiency of the delay cut is 97 % for neutrons thermalized in PC and it is 96 % for neutrons thermalized in water.

- the energy of the candidate first event must exceed than 3.5 MeV.

In absence of a dedicated muon veto in CTF this cut is the only effective way to select signal from a muon crossing the tank with a track close to the inner vessel.

The efficiency of the first event energy cut is guessed to be of the order of 1, in absence of a dedicated simulation.

- the energy of the candidate second event must lie in the range between 250 KeV and 3 MeV.

The lower limit of the energy window is not set to zero to prevent background from random coincidences.

The efficiency of the second event energy cut is known from Monte Carlo simulations of the energy spectra performed with the GENEB code (see reference [B⁺93]). The simulated spectra for the neutrons thermalized in water and in PC are shown respectively in figure IV.23 and IV.22. In the case of neutrons thermalized in water the spectrum is shifted to lower energies since a fraction of γ -rays energy is deposited outside the inner vessel.

The efficiency of the second event energy cut is 95 % for neutrons thermalized in PC and it is 60 % for neutrons thermalized in water;

Table IV.13: Efficiencies of the neutron cuts for the selection of the neutron sequences.

Cut	Efficiency (water)	Efficiency (PC)
Delay	0.96	0.97
Energy first event	~ 1	~ 1
Energy second event	0.60	0.95
Combined cuts	~ 0.6	~ 0.9

The global efficiency of the combined neutron cuts is of about 90 % for neutrons thermalized in PC and of about 60 % for neutrons thermalized in water. A summary of the efficiencies of the neutron cuts is reported in table IV.13.

The rate of random sequences surviving these cuts amounts to:

$$r = r_1 \times r_2 \times \tau \quad (\text{IV.71})$$

$$= 10^{-1} \text{ s}^{-1} \times 5 \times 10^{-3} \text{ s}^{-1} \times 2 \times 10^{-3} \text{ s} \quad (\text{IV.72})$$

$$= 10^{-6} \text{ s}^{-1} \quad (\text{IV.73})$$

and it is negligible with respect to the expected rate (see below in this section).

Neutron sequences were looked for in the data taking period going from phase Lima to phase Oscar. The overall data length is 160 days.

Figure IV.24 shows the delay distribution for the sample of sequences selected by means of the neutron cuts. The delay time distribution is an exponential with a meanlife of about $250 \mu\text{s}$ and it is compatible with a superposition of signals from neutrons thermalized in water and in scintillator. The distribution of the energy of the candidate second events is shown in figure IV.25 and it is in agreement with the prediction of the Monte Carlo simulation performed using the GENEB code (see reference [B⁺93]) which is shown in figure IV.26.

The sample of sequences with energy of the candidate second event in the gamma peak includes 170 units. Taking into account the simulated spectra for neutrons captured in water and in the scintillator, the CTF estimate for the number of events producing neutrons is:

$$(1.5 \pm 0.1) \times 10^{-2} \text{ events/m} \quad (\text{IV.74})$$

The best estimate for the neutron production rate by ultrarelativistic muons in deep underground laboratories comes from an experiment performed in the Mont Blanc laboratory [A⁺89] and amounts to:

$$(5 \pm 1) \times 10^{-4} \text{ (neutrons} \times \text{cm}^2\text{)/g} \quad (\text{IV.75})$$

for materials of density of about 1 g/cm^3 like water or the CTF scintillator the previous estimate corresponds to:

$$(5 \pm 1) \times 10^{-2} \text{ neutrons/m} \quad (\text{IV.76})$$

The best estimate for the mean multiplicity also comes from the Mont Blanc experiment, and it ranges from 2 to 4.

We conclude that the CTF estimate is not in disagreement with the results quoted in the literature. The CTF cannot improve the results of the literature because it cannot record multiple coincidences. However it must be remarked that Borexino will be able to measure the neutron production rate with an accuracy higher than quoted in the literature.

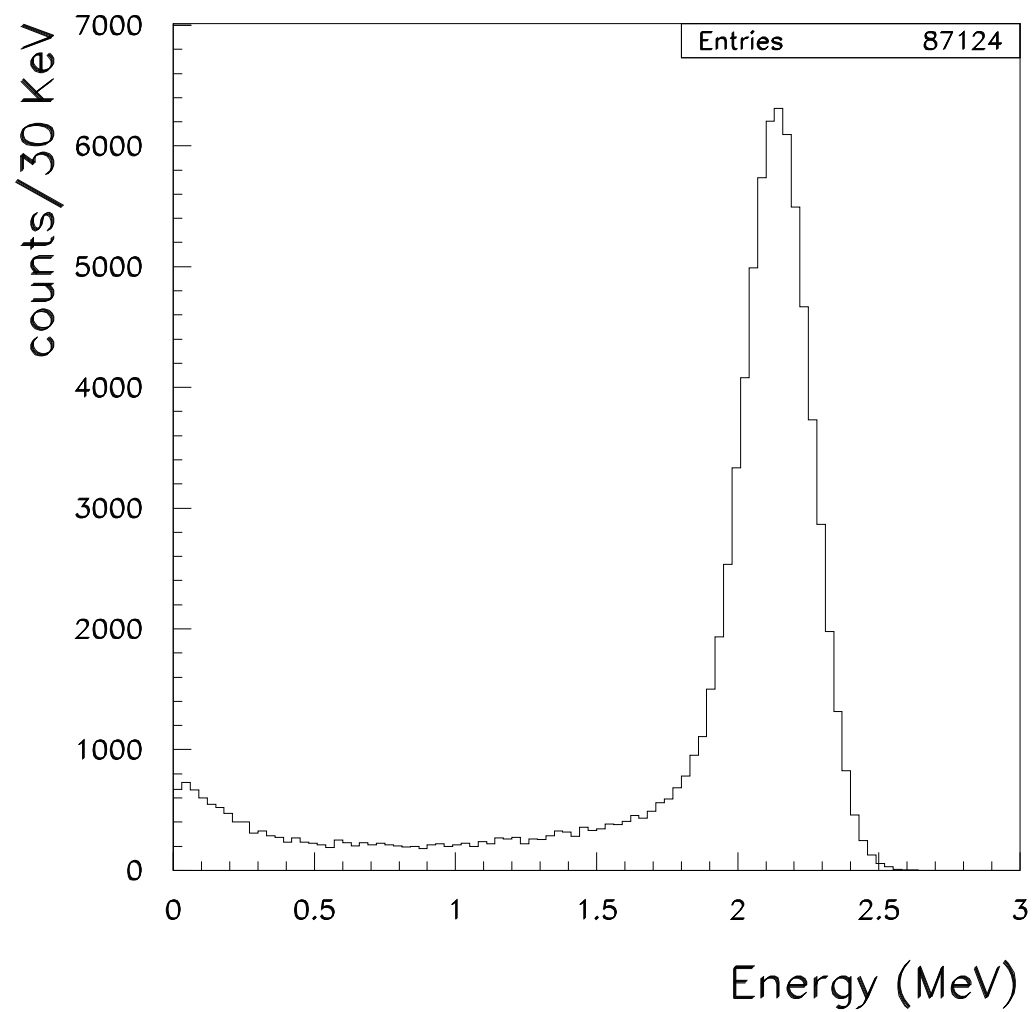


Figure IV.22: Simulation.
Expected energy spectrum for γ -rays from capture of neutrons thermalized in the scintillator.

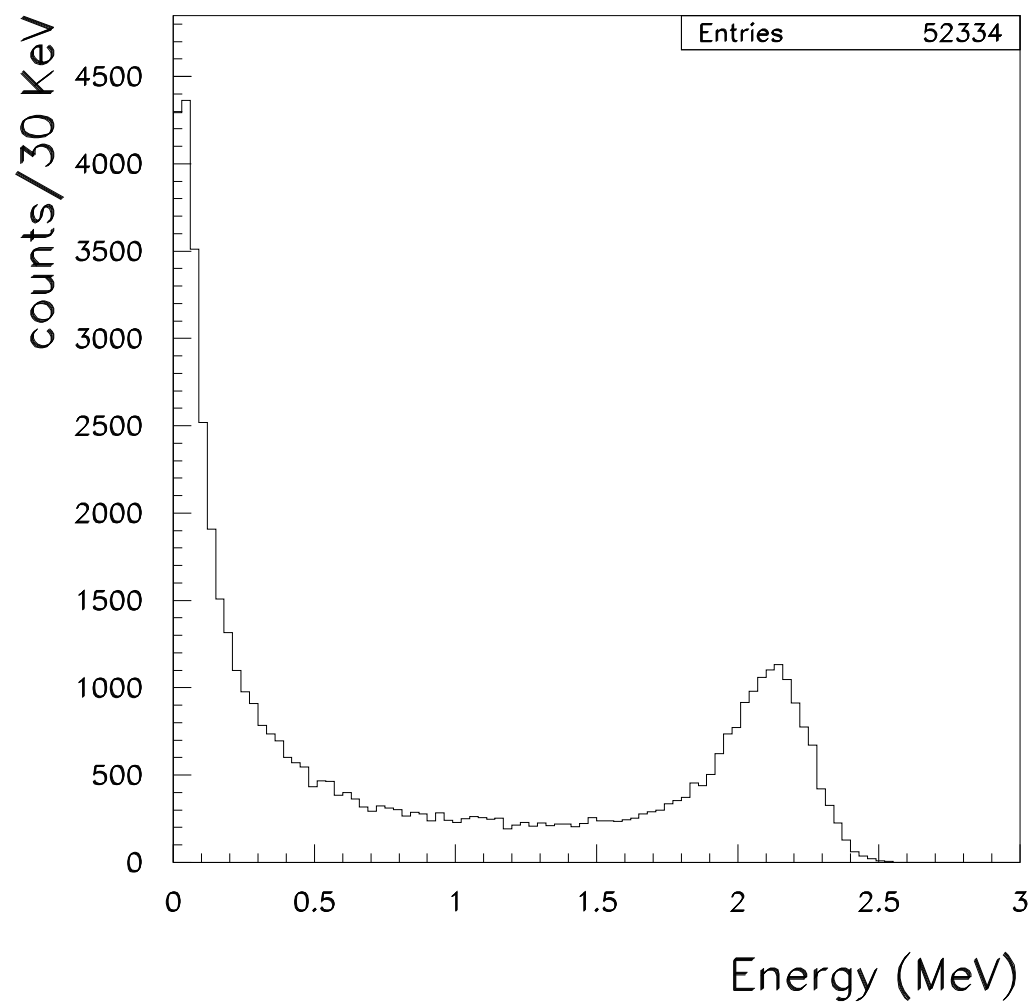


Figure IV.23: Simulation.
Expected energy spectrum for γ -rays from capture of neutrons thermalized in the water buffer.

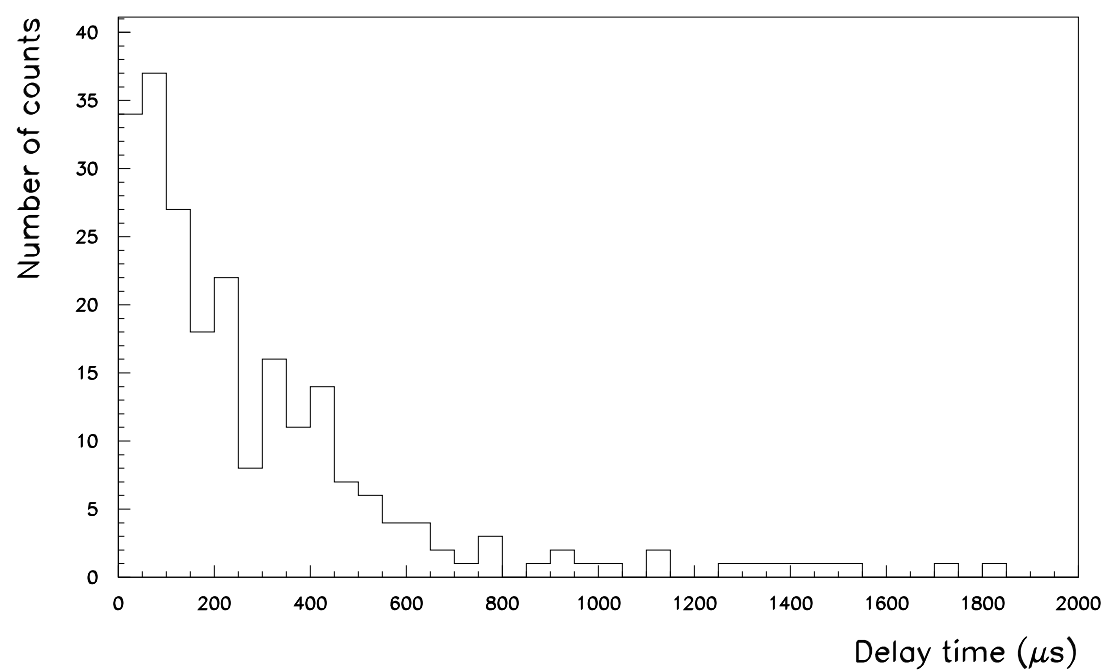


Figure IV.24: 160 d of data taking, from phase Lima to phase Oscar.
 Delay distribution for the sample of sequences selected by means of the neutron cuts.

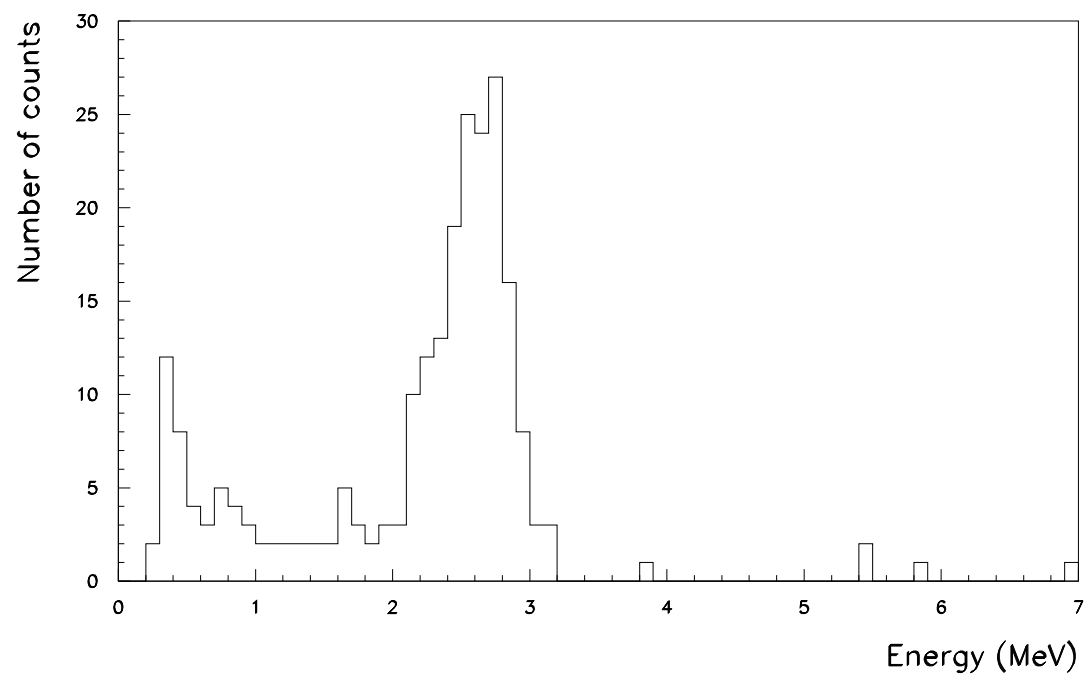


Figure IV.25: 160 d of data taking, from phase Lima to phase Oscar.
 Energy distribution for the candidate second events in the sample of sequences selected by means of the neutron cuts.

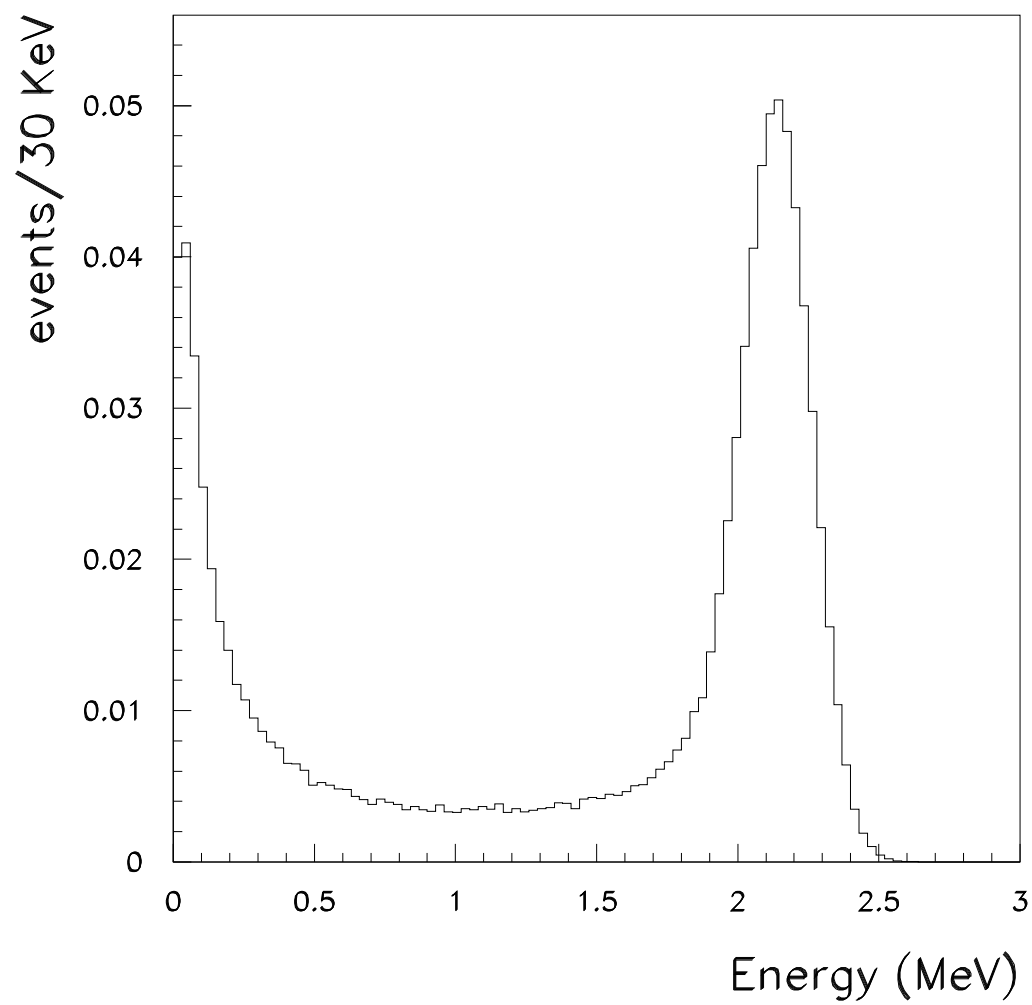


Figure IV.26: Simulation.

Expected energy spectrum for γ -rays from capture of neutrons thermalized both in the scintillator and in the water buffer.

Chapter V

Measurements performed without using the delayed coincidences method

V-A α/β discrimination

In liquid organic scintillators it is possible to discriminate between scintillation events excited either by α or β radiation by exploiting the different excitation modes of the scintillator. α events differ from β events owing to a bigger fraction of photons in the slow scintillator decay component, as discussed in section II-B.9. Both BX and CTF use this method to discriminate between α and β events. However the techniques implemented in BX and in CTF are slightly different owing to the different mean number of photons detected per electronic channel.

In BX the mean number of photons detected per channel is much lower than one (light yield of 300 p.e./MeV and 2200 PMTs), allowing to measure the arrival time distribution of photons. The subtraction of the time of flight after the position reconstruction allows to obtain the full distribution of the scintillator decay. The discrimination between α and β pulses is performed by a fit on the scintillation decay time, as it is described in reference [Man97].

In CTF the mean number of photons detected per channel is much bigger than one (light yield of 300 p.e./MeV and 100 PMTs). Since an electronic channel can record the arrival time only for the first photon detected, it is not possible to reconstruct the full arrival time distribution of photons. The informations about the tail is completely lost, therefore the fraction of light belonging to the slow scintillation component cannot be reconstructed from the time measurement. CTF cannot discriminate between α and β events on the basis of the time measurement, and it is forced to use a less effective method.

In CTF the full charge and the tail charge of the signal are measured separately by integrating the output of the analog sum channel. The ratio of the tail charge to the full charge is expected to be bigger for α events than for β events, owing to the difference in the tail component. The discrimination of α from β events is based just on the ratio of the tail charge to the total charge.

On the basis of laboratory measurements of the scintillator decay (see II.4), the integration gate for the full charge is set to 500 ns. There are two different integration gates for the tail charge (also set to 500 ns), which are opened with the fixed delays of 32 ns and 48 ns with respect to the start of the signal, and the corresponding discrimination parameters are respectively called as charge ratios R32 and R48.

Figure V.1 shows the distribution of the charge ratio R32 versus energy for the events of phase Foxtrot. The α particles from ^{214}Po (~ 750 KeV) and from ^{222}Rn and ^{218}Po (~ 450 KeV) are identified owing to the higher value of the charge ratio R32 (~ 0.3 – 0.4). The distribution for α particles are well separated from the belt of β events due to ^{214}Bi with a charge ratio of ~ 0.2 – 0.3 .

The easiest way to determine the efficiency of α/β discrimination is to check it against samples of mass 214 sequences. Mass 214 sequences are easily separated from background by means of the U cuts which use the delayed coincidence method. They are a sequence composed by a $(\beta+\gamma)$ event and by an α event, allowing to identify α or β signals on the single event basis. At the electron equivalent energy of the ^{214}Po , to say 751 KeV, the efficiency for α identification is of ~ 97 % with an associated β misidentification of ~ 3 %.

The efficiency of α/β discrimination can be measured also at lower energies (350–550 KeV) where β events from ^{214}Bi and α events from ^{222}Rn and ^{218}Po can be found. In this case the coincidence method cannot be used and therefore it is not possible to identify α and β signals on the single event basis. The mixed distribution of α and β events for the charge ratios R32 and R48 is fitted with a linear combination of two gaussians in order to disentangle the two contributions. The efficiency for α identification ranges from 90 %

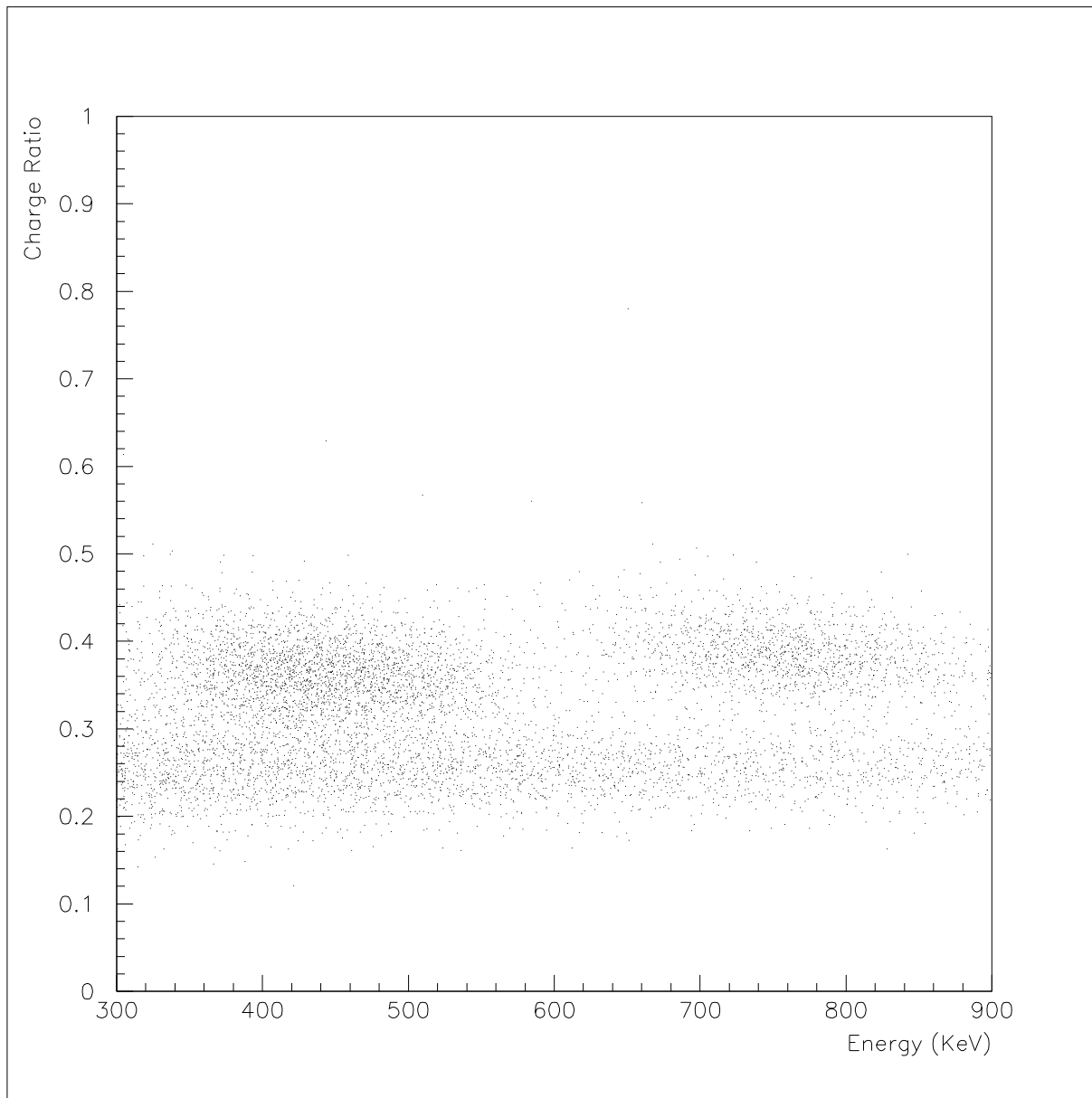


Figure V.1: Phase Foxtrot.

Distribution of the charge ratio R32 versus energy.

The α particles from ^{214}Po (~ 750 KeV) and from ^{222}Rn and ^{218}Po (~ 450 KeV) have a charge ratio R32 of ~ 0.3 – 0.4 and are separated from the belt of β events due to ^{214}Bi having a charge ratio of ~ 0.2 – 0.3 .

to 97 % with an associated β misidentification of 10 %.

V-B Discrimination of the Čerenkov from the scintillation events

In CTF it is possible to discriminate the scintillation events from the Čerenkov events produced in the shielding water by cosmic rays and γ -rays.

Tags for Čerenkov events were obtained by analyzing the data collected in phase Bravo when the IV was filled with water (see chapter III-C). In figure V.2 the spectrum for the Čerenkov radiation is shown.

The low energy component of the spectrum (less than 30 photoelectrons) is Čerenkov radiation produced by γ -rays and electrons of radioactive origin, while the component covering all the spectrum is due to the through-going muons. The time spread of the photons for the two components is completely different. For events with less than 30 photoelectrons (p.e.), the mean arrival time of the p.e. with respect to the first is lower than 10 ns (see figure V.3). For events with more than 30 p.e., the mean arrival time exceeds 20 ns (also shown in figure V.3). The distributions of the photon arrival times for Čerenkov events are very different from the same distribution for scintillation events with more than 30 p.e. (which is roughly equivalent to 100 KeV), shown in figure V.4. In the latter case, the mean arrival time lies in the range between 10 and 25 ns.

Furthermore, the spatial distribution of the Čerenkov light produced by the through-going muons is not uniform. Due to the directionality of the incoming muon flux, more light is detected by the bottom hemisphere PMTs than by the top PMTs. The typical fraction of light detected by the PMTs of the upper hemisphere is 15–20 % of the total.

Therefore, the identification and rejection of the Čerenkov events is performed by means of the following cuts, referred to as the scintillation cuts:

- the mean arrival time of the photoelectrons is required to lie between 3 and 16 ns.

The limits of the time window are chosen so as to maximize the Čerenkov rejection while minimizing the misidentification of scintillation events;

- the fraction of the light detected by the tubes of the upper hemisphere over the total is required to lie in the range 0.35–0.75.

The upper limit of 0.75 is chosen as to reject a further class of events that was observed both in the water and in the scintillator runs and showed a fraction of light detected by the upper hemisphere > 80 %. These events are interpreted as electronic noise and they are completely rejected by this cut.

The rejection efficiency of the scintillation cuts for the Čerenkov events in the energy range above 250 KeV is 95 %. In the same energy range, misidentification of scintillation events by the scintillation cuts amounts to only 2 %.

V-C Spatial reconstruction

The space-time coordinates of the events are calculated from the arrival time distribution of the photons using the maximum likelihood method (see section IV-B.3 for a description of the method).

The arrival time t_a^i of the first detected photon on the i^{th} electronic channel is:

$$t_a^i = t_0 + t_d^i + t_f^i + t_j^i \quad (\text{V.1})$$

where t_0 is the absolute time of the event, t_d^i is the scintillator decay time, t_f^i is the photon time of flight and t_j^i is the jitter time proper of the PMT.

The Probability Density Function called PDF is defined as the convolution of the probability density functions for the scintillator decay time (t_d) and the jitter time (t_j). The PDF was first measured in laboratory and then tuned using the data collected with a ^{222}Rn source during phase Rubatto (see section V-D for a description of the ^{222}Rn source tests). Since in the relevant range of energies usually more than one photon is detected per each channel, the PDF depends on the energy.

The optical path of the single photon is not unambiguously determined by the start and stop points: deviation from Fermat's law arise from light scattering, reflection on the vessel, absorption and reemission. These deviations are accounted for by defining an effective refractive index n_{eff} . The value of $n_{\text{eff}} = 1.9$ used in the reconstruction code was finely tuned using the data collected of the ^{222}Rn source tests performed during phase Rubatto (see section V-D). The source was situated in about 30 different positions. Figure V.5

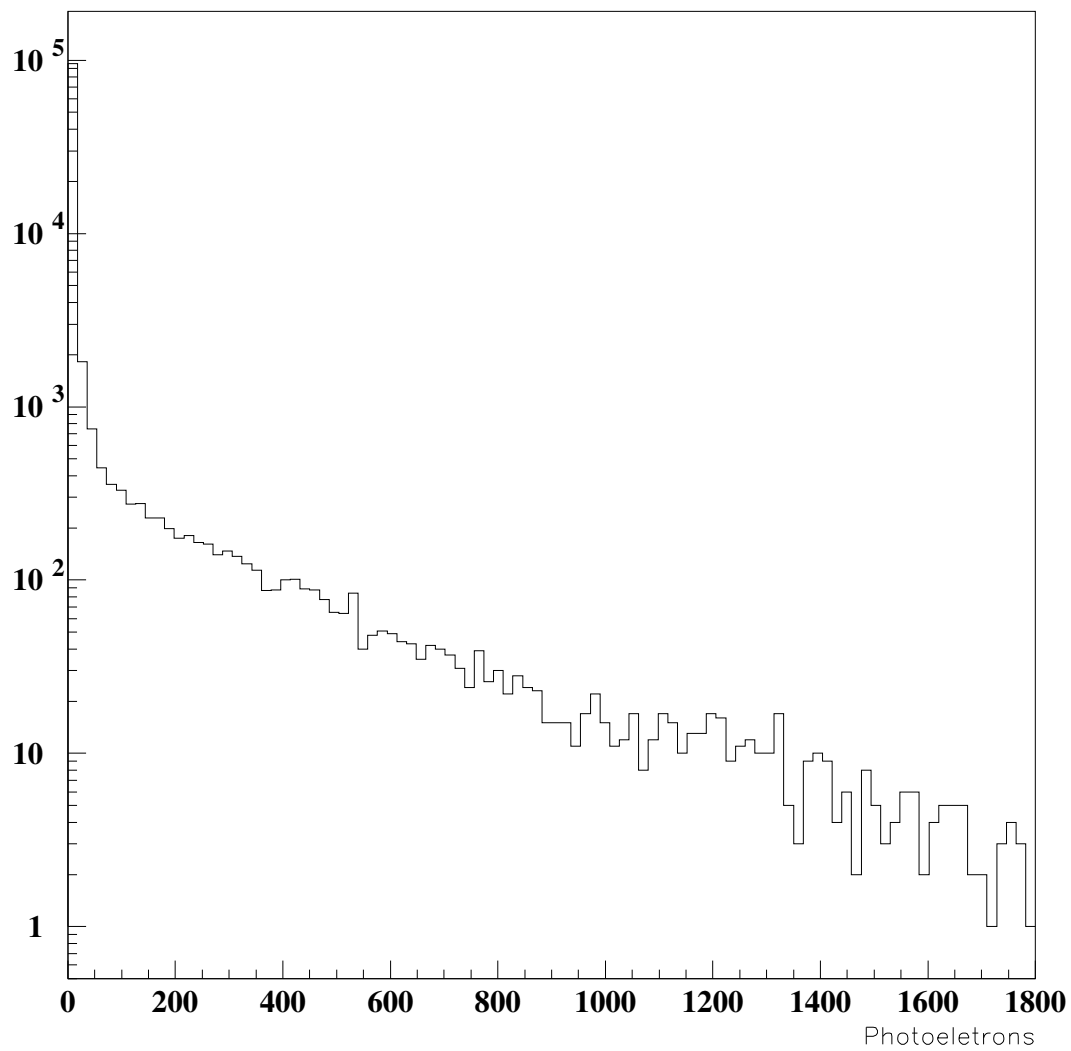


Figure V.2: Phase Bravo. Spectrum of the Čerenkov radiation.

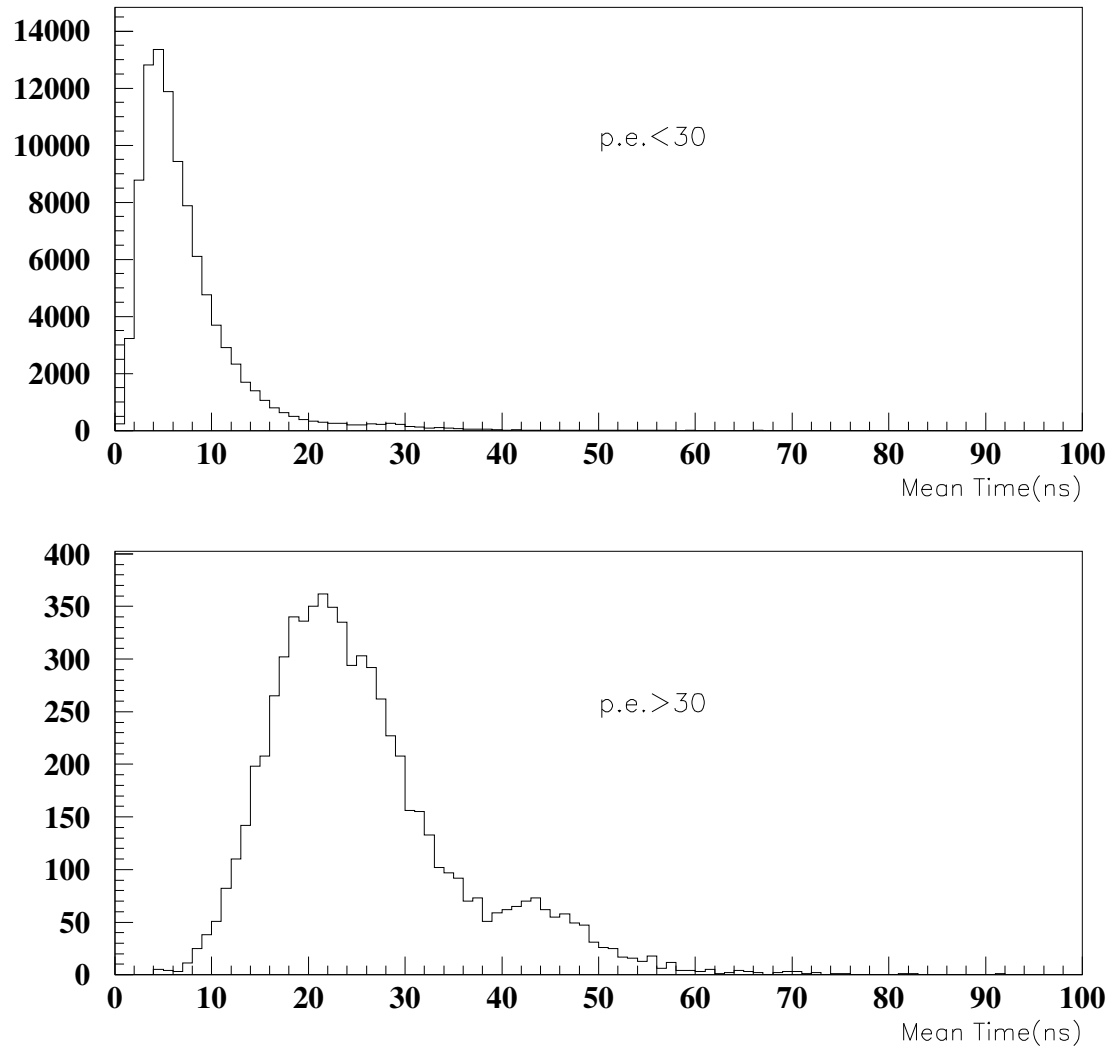


Figure V.3: Phase Bravo. Photon arrival time distribution for the two components of Čerenkov radiation.

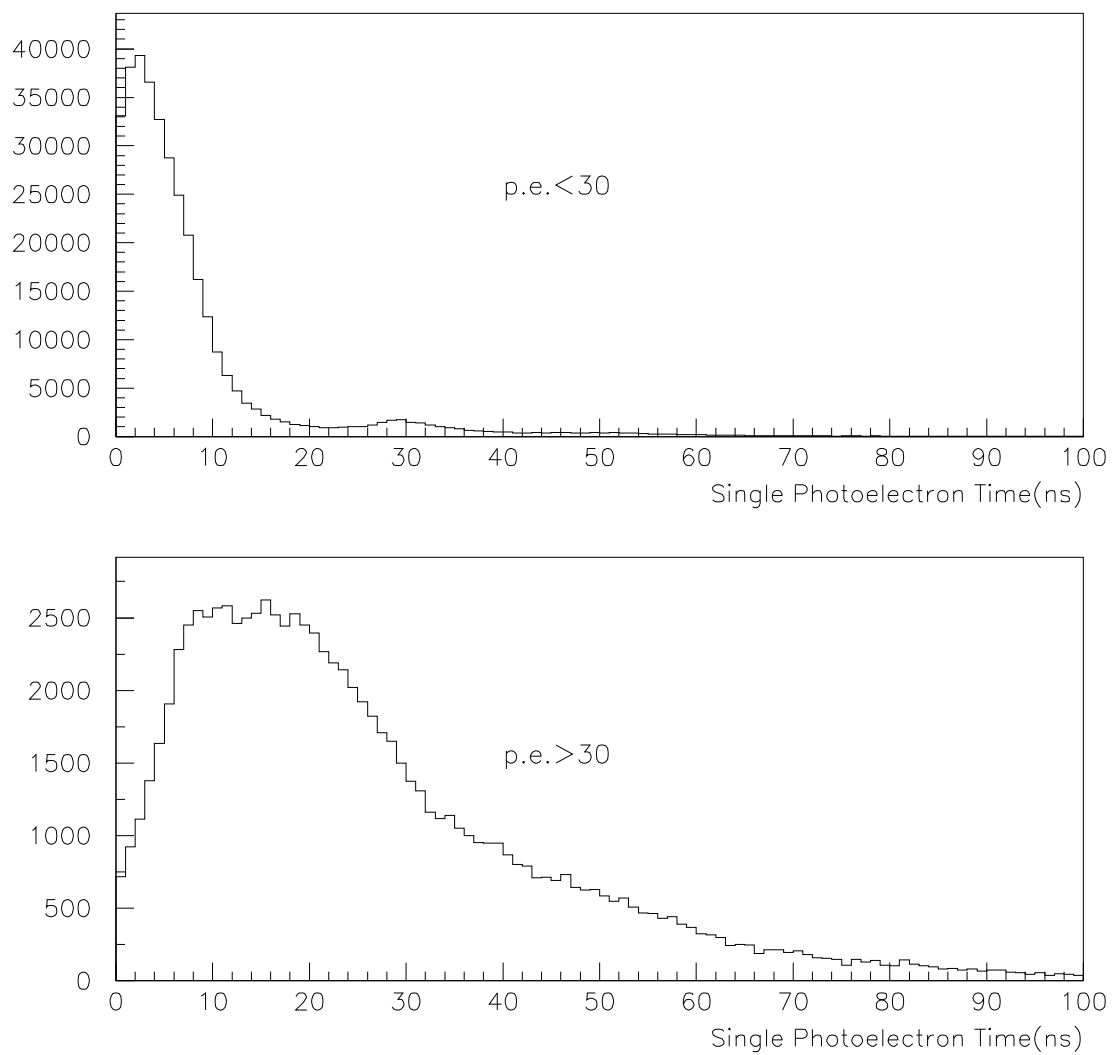


Figure V.4: Phase Foxtrot. Photon arrival time distribution for the scintillation events.

shows the comparison between the nominal positions of the ^{222}Rn source and the reconstructed positions. The differences between the nominal and reconstructed positions were minimized for the value $n_{\text{eff}} = 1.9$ and they were found to be zero within the error of 5 cm.

The time of flight t_f^i is defined as:

$$t_f^i = \frac{d_0^i \times n_{\text{eff}}}{c} \quad (\text{V.2})$$

where d_0^i is the distance between the i^{th} PMt and the assumed birth place of the photon.

Given an eventual set of space-time coordinates (t_0, x_0, y_0, z_0) as candidate to represent the space-time point of the event, it is possible to derive the associated value of $t_d^i + t_j^i$:

$$t_d^i + t_j^i = t_a^i - t_0 - \frac{d_0^i \times n_{\text{eff}}}{c} \quad (\text{V.3})$$

The likelihood is a function of the space-time points defined as:

$$L(t_0, x_0, y_0, z_0) = \prod_i \text{PDF}(t_d^i + t_j^i) \quad (\text{V.4})$$

the space time point which is the maximum for L is taken as the best estimate for the reconstructed point.

The resolution of the reconstructed spatial coordinates is of 25 cm at 0.25 MeV and 10 cm at 1 MeV.

V-D Decay mechanism of the scintillator and light propagation

The studies were performed by means of ^{222}Rn sources composed by small quartz vials filled with ^{222}Rn spiked scintillator. The ^{222}Rn source tests were performed during phase Rubatto (see chapter III-C).

Photons are emitted by the excited states of the fluor (PPO). While propagating in the scintillator, photons interact with PPO and PC molecules. For wavelengths shorter than 370 nm the interaction with PPO dominates, while for longer wavelengths the interaction with PC dominates.

In the interaction with PPO, photons are absorbed and re-emitted with high probability (quantum efficiency of 0.8). Being the PPO absorption higher for the shorter wavelengths, this process shifts the effective emission spectrum of PPO to longer wavelengths.

The interaction with PC is mainly due to elastic scattering, which gives rise only to a change of the direction of the photons.

The decay time of the main component of the scintillator, as measured in a small scale sample, is 3.5 ns. In presence of absorption and reemission, a longer effective decay time of 4.5–5.0 ns is observed.

A complete review of the studies on the decay mechanism of the scintillator and on light propagation in CTF can be found in reference [A⁺98a].

V-E ^{14}C contamination

Since organic liquid scintillators are predominantly composed of carbon, the intrinsic concentration of the radioisotope ^{14}C can constitute the main background at low energies. ^{14}C decays emitting a β^- -ray, with a 156 KeV maximum kinetic energy and a 8266 years meanlife.

Liquid scintillator solutions contain aromatic solvents and these are in turn synthesized from petroleum. While modern carbon of biological origin has an isotopic ratio $^{14}\text{C}/^{12}\text{C}$ of 10^{-12} , it is expected that petroleum derivatives have a ^{14}C abundance that is orders of magnitude lower. Petroleum deposits are found deep underground and are shielded from the cosmic rays flux present at the earth surface responsible for the continuous production of ^{14}C from ^{14}N via the reaction $^{14}\text{N}(n,p)^{14}\text{C}$. Consequently, the cosmogenic production of ^{14}C in underground petroleum is minimized and any ^{14}C originally present in the precursor organic material to the petroleum will have had millions of years to decay away. Thus one would expect the ^{14}C isotopic abundance in an organic liquid scintillator to be extremely low. In fact, the abundance of ^{14}C in petroleum has never been determined.

Though the maximum energy for the ^{14}C decay product is 156 KeV, finite energy resolution and pile-up can create a tail in the ^{14}C energy spectrum that extends to higher energy. Thus, the intrinsic level of ^{14}C in the liquid scintillator becomes an important consideration in setting the low-energy threshold for neutrino events in BX. At the contamination level for the ratio $^{14}\text{C}/^{12}\text{C}$ of 10^{-18} , the counting rate due to ^{14}C in the neutrino window amounts to 0.1 counts/day (see section II-C.2). From these considerations, it is desirable in BX that the ratio $^{14}\text{C}/^{12}\text{C}$ does not substantially exceed 10^{-18} .

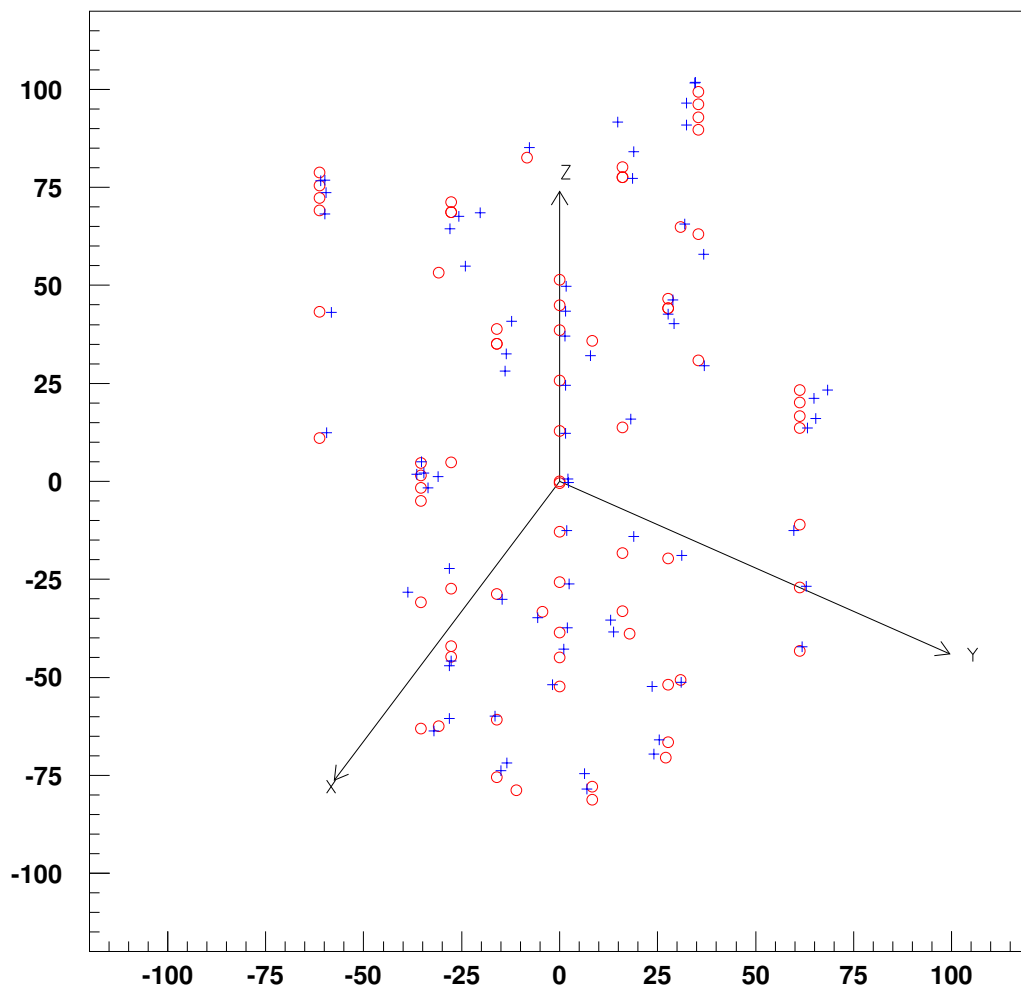


Figure V.5: Phase Rubatto.

Comparison between the nominal positions of the ^{222}Rn source (empty circles) and the reconstructed positions (small crosses).

The ^{222}Rn source was situated in about 30 different positions in the frame of the ^{222}Rn source tests described in section V-D.

The differences between the nominal and reconstructed positions were minimized for the value $n_{\text{eff}} = 1.9$ and they were found to be zero within the error of 5 cm.

The ^{14}C abundance is measured by means of a fit of the ^{14}C β spectrum on the energy spectrum detected by CTF (for a full description of the analysis see reference [A⁺98c]). The theoretical β spectrum used to fit the data has the following form:

$$N(W_e)dW_e = P_e W_e (W_0 - W_e)^2 F(Z, W_e) C(W_e) dW_e \quad (\text{V.5})$$

where P_e , W_e are the momentum and total energy of the emitted electron, W_0 is the endpoint, $F(Z, W_e)$ is the Fermi function which accounts for the influence of the nuclear Coulomb field on the β spectrum, and $C(W_e) = 1 + aW_e$ is the shape factor for the β decay. The raw data were fit with a function $S(W_e)$ given by:

$$S(W_e) = B(W_e) + \int dW'_e N(W'_e) g(W'_e, W_e) \quad (\text{V.6})$$

where $N(W_e)$ is the theoretical β spectrum, $g(W'_e, W_e)$ is the detector response function and $B(W_e)$ is a polynomial which accounts for the background contribution. From calibration measurements it is known that $g(W'_e, W_e)$ has a gaussian shape.

A χ^2 analysis was performed in an energy interval between 60 KeV and 250 KeV (see figure V.6). During the minimization, the β endpoint was fixed to 156 KeV while the following four parameters were allowed to vary:

- the overall normalization factor corresponding to the ^{14}C activity;
- the shape factor $C(W_e)$ describing the deviation of the ^{14}C β spectrum from the allowed statistical shape;
- the energy scale factor relating the measured PMTs charge signal to the energy deposition;
- the proportionality constant determining the relation $\sigma(E) \propto \sqrt{E}$, where E is the energy deposition.

The latter two parameters were left free in the fit as they were not determined with the necessary accuracy at these low energies.

The $^{14}\text{C}/^{12}\text{C}$ ratio R is given by:

$$R = \frac{A\tau M}{9N_A m} \quad (\text{V.7})$$

where A is the ^{14}C activity, τ is the ^{14}C meanlife, M is the molecular weight of PC (120 g/mol), N_A is the Avogadro constant, m is the scintillator mass and the 9 in the denominator comes from the 9 carbon atoms in C_9H_{12} .

The best estimate for R is:

$$(1.94 \pm 0.01_{\text{stat}} \pm 0.09_{\text{syst}}) \times 10^{-18} \quad (\text{V.8})$$

the largest uncertainty in the absolute determination of the isotopic abundance of ^{14}C arises from the detector mass determination, which was known within an accuracy of 5 %.

The $^{14}\text{C}/^{12}\text{C}$ ratio measured in CTF is the lowest ^{14}C abundance ever measured.

V-F The results of the NAA measurements

At the Munich University the local BX group developed a facility exploiting the NAA technique to measure material contaminations at the ultra-trace (see reference [G⁺98]). The facility allows to measure the CTF scintillator at the BX radiopurity level, providing informations complementary to those obtained by the CTF.

In fact, NAA technique allows to probe directly the presence of the fathers of the natural radioactive chains (^{238}U and ^{232}Th) while CTF probes directly the rate of the mass 212 and 214 sequences. Therefore in the case the secular equilibrium of the natural radioactive chains were broken (the chains are shown in figures IV.15 and IV.17) the activity of the daughter nuclides can be almost all reconstructed by means of these two complementary and independent measurements.

Moreover, the Munich detector allows to measure the $^{\text{nat}}\text{K}$ contamination.

The following records were achieved by measuring samples of the CTF scintillator:

- $< 2 \times 10^{-15}$ g/g for ^{232}Th contamination
- $< 2 \times 10^{-16}$ g/g for ^{238}U contamination
- $< 4 \times 10^{-12}$ g/g for $^{\text{nat}}\text{K}$ contamination

no evidence for ^{232}Th , ^{238}U and $^{\text{nat}}\text{K}$ were found within the sensitivity of the facility. Therefore the results are quoted in terms of upper limits on the contaminations.

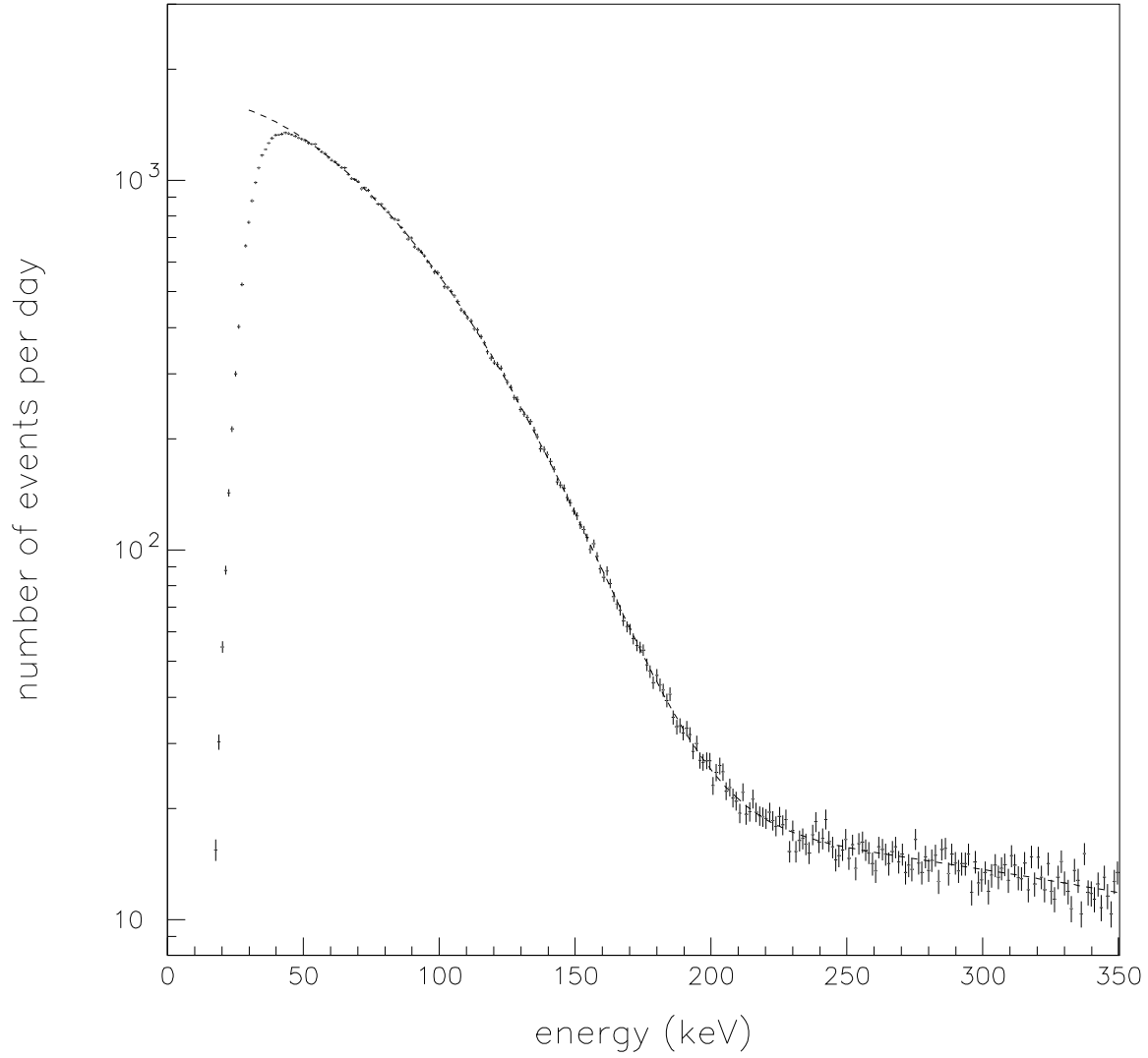


Figure V.6: Phase Oscar.

Energy spectrum of CTF in the energy interval below 350 KeV.

The spectrum is fitted with the β spectrum of ^{14}C plus a slowly varying background to derive the ^{14}C contamination.

V-G The total counting rate

V-G.1 The sources

In CTF the total counting rate in the neutrino window has been object of a long study in view of BX. BX was designed to measure the ν_e -e scattering from solar neutrinos ${}^7\text{Be}$. The only signatures for ${}^7\text{Be}$ neutrinos are the spectral signature and the seasonal variations of the neutrino flux. There is no event by event signature, therefore it is very important to reach the lowest background level in the neutrino energy window (250–800 KeV) centered around the expected shoulder of ${}^7\text{Be}$ neutrino spectrum.

The total counting rate in CTF is due to the following sources of background:

Internal background is contaminants present in the scintillator. We can distinguish between intrinsic contaminants of the scintillator components surviving after the synthesis processes, and contaminants introduced during the scintillator liquid handling (transport, storage vessels and plumbing). Some of the internal contaminants have already been tagged and measured:

- the intrinsic contaminants have been measured by evaluating ${}^{14}\text{C}$ and the presence of ${}^{232}\text{Th}$ and ${}^{238}\text{U}$ daughters.

From the measurement in CTF of the ${}^{14}\text{C}$ content in the scintillator (see section V-E), the contribution of ${}^{14}\text{C}$ to the rate over 250 KeV is negligible.

The measurements of ${}^{238}\text{U}$ and ${}^{232}\text{Th}$ equivalent contamination performed directly in CTF by probing the rate of mass 212 and 214 sequences (see sections IV-B and IV-C) showed that the activity in the neutrino window of the lower parts of the two chains, accounting for all the nuclides whose decay is surely in temporal equilibrium with the probed sequences, is of about 10 counts/day.

The activity of the father of the two radioactive chains has been measured in laboratory on a small sample of scintillator by means of the NAA technique. Upper limits of 2×10^{-16} g/g for the ${}^{238}\text{U}$ and 2×10^{-15} g/g for ${}^{232}\text{Th}$ were obtained (see section V-F). On the basis of this estimate we can guess that the activity of the upper parts of the two chains does not exceed 5 counts/day;

- ${}^{85}\text{Kr}$ is a contaminant introduced during the handling of the scintillator. ${}^{85}\text{Kr}$ activity in the scintillator was measured directly in CTF as discussed in section IV-D. The ${}^{85}\text{Kr}$ activity during phase Foxtrot, before any purification of the scintillator, was of about 390 events/day. A relevant fraction of this activity (about 40 %) is recorded in the neutrino window. During phase Lima, after the scintillator water extraction, and during phase Oscar, after the scintillator distillation, there was no evidence for ${}^{85}\text{Kr}$ activity in the scintillator. ${}^{85}\text{Kr}$ was successfully removed by the scintillator water extraction.

The best estimate for the ${}^{85}\text{Kr}$ activity after purification is zero. The best upper limit is obtained in phase Oscar, owing to higher statistics: it amounts to 35 counts/day for the total activity and of 15 counts/day for the activity in the neutrino window.

Surface background is contaminants implanted on the internal walls of the Inner Vessel. In particular, ${}^{222}\text{Rn}$ exposure of the inner vessel during the phase of nylon extrusion may have given rise to implantation of ${}^{210}\text{Po}$ nuclides on the nylon surface. ${}^{222}\text{Rn}$ emanating from the inner vessel (see section IV-C.2) is also a source of surface background, but its activity is negligible as far as the total background is concerned.

External background is γ -rays and neutrons from the rocks of the cave, the construction materials of the CTF and the shielding water.

Rn measurements of the shielding water by means of a charcoal trap concentrator followed by a counting in miniaturized proportional counters revealed that Rn was by far the major source of external background. The measurements performed directly in CTF (see below in this section) showed as well that the external background is strongly dominating the total counting rate. ${}^{222}\text{Rn}$ in water is emanated by several construction materials, like the permatex (an epoxy resin) coating the internal walls of the water tank and PMTs and the cables. Another source of Rn may be due to small leaks at the top of the water tank. Excess of ${}^{226}\text{Ra}$ in water, though unlikely, is not ruled out.

In order to disentangle the contributions of the three classes of background to the total counting rate in the neutrino window, we studied the distribution of the reconstructed position of the events belonging to the three classes. Owing to the spherical geometry of the IV, the only radial distribution characterizes completely the three dimensional distribution of the events.

Table V.1: Results of the radial analysis disentangling the contribution of the various classes of background to the total counting rate in the neutrino window.

	Phase Foxtrot (before purification)	Phase Oscar (after purification)
χ^2 per degree of freedom	1.02	0.90
mean value of the surface distribution [m]	1.04 ± 0.03	1.07 ± 0.02
σ of the surface distribution [m]	0.12 ± 0.03	0.11 ± 0.03
external background [counts/day]	1700 ± 270	2050 ± 100
surface background [counts/day]	350 ± 190	170 ± 60
internal background [counts/day]	470 ± 90	21 ± 47
expected internal background from internal ^{222}Rn		30 ± 7

The ^{214}Po events selected together with ^{214}Bi events by means of the delayed coincidence method during phase Foxtrot are expected to be uniformly distributed in the inner vessel. Furthermore ^{214}Po events are point-like scintillation events unlike the ^{214}Bi events that are constituted by an electron-gamma shower. Therefore the ^{214}Po events were chosen as representatives of the internal background. Their radial distribution in the innermost region is expected to be proportional to the differential volume element ($\propto \text{radius}^2$) and at the inner vessel edge it is expected to show the characteristic gaussian tail due to the finite resolution. The reconstructed radial distribution for the ^{214}Po events is shown in figure V.7. As expected, it is in agreement with the theoretically predicted radial distribution which is also shown in figure V.7.

The events detected during phase Quebec in the radon-in-water test are due to ^{222}Rn and daughters dissolved in the shielding water, which at that time were dominating the total counting rate as it is shown in section IV-C.2. These events are taken as representative of external background. The radial distribution of the external ^{222}Rn shown in figure V.7 proves that the gammas emitted by the ^{222}Rn daughters (^{214}Bi and ^{214}Pb are $\beta+\gamma$ emitters) penetrate deeply into the Inner Vessel, producing showers which can be totally or partially contained within the scintillator.

As expected the mean value of the reconstructed radius for external contaminations is higher than for internal contaminations. The marked difference between the two distributions shown in figure V.7 allows to disentangle the two contributions to the total counting rate by means of a fit on the radial distribution of the events detected.

Two similar but independent analysis were developed.

The first analysis was developed by myself and it consisted in studying the class of the events surviving the scintillation cuts (see section V-B). The Čerenkov events produced by cosmic rays in the water are removed by the scintillation cuts. The radial distribution of the surviving events was fitted by a linear combination of three functions: the external background radial distribution, the internal background radial distribution and a gaussian representing a possible surface contamination. The normalization factors of the three functions, the mean value and the σ of the gaussian representing the surface background are the free parameters of the fit.

The second method was developed by S. Malvezzi and it consisted in studying the class of all the events detected. The radial distribution of all the events was fitted by a linear combination of four functions: it was added the radial distribution of the Čerenkov events, that was measured in phase Bravo (see section III-C). The normalization factor of the Čerenkov radial distribution was also added to the free parameters of the fit.

Three different phases were analyzed:

- phase Foxtrot, before any purification of the scintillator;
- phase Lima, after scintillator water extraction;
- phase Oscar, after scintillator distillation.

The results obtained in phase Lima are not quoted because they are consistent with the values obtained in phase Oscar but in the meanwhile they are less significative owing to much lower statistics.

Figures V.8 and V.9 show the radial distributions for phase Foxtrot and phase Oscar fitted with the two different analysis methods. The results obtained with the two analysis described above are consistent: the common results on the contribution of each class of background to the total counting rate in the neutrino window are quoted in table V.1.

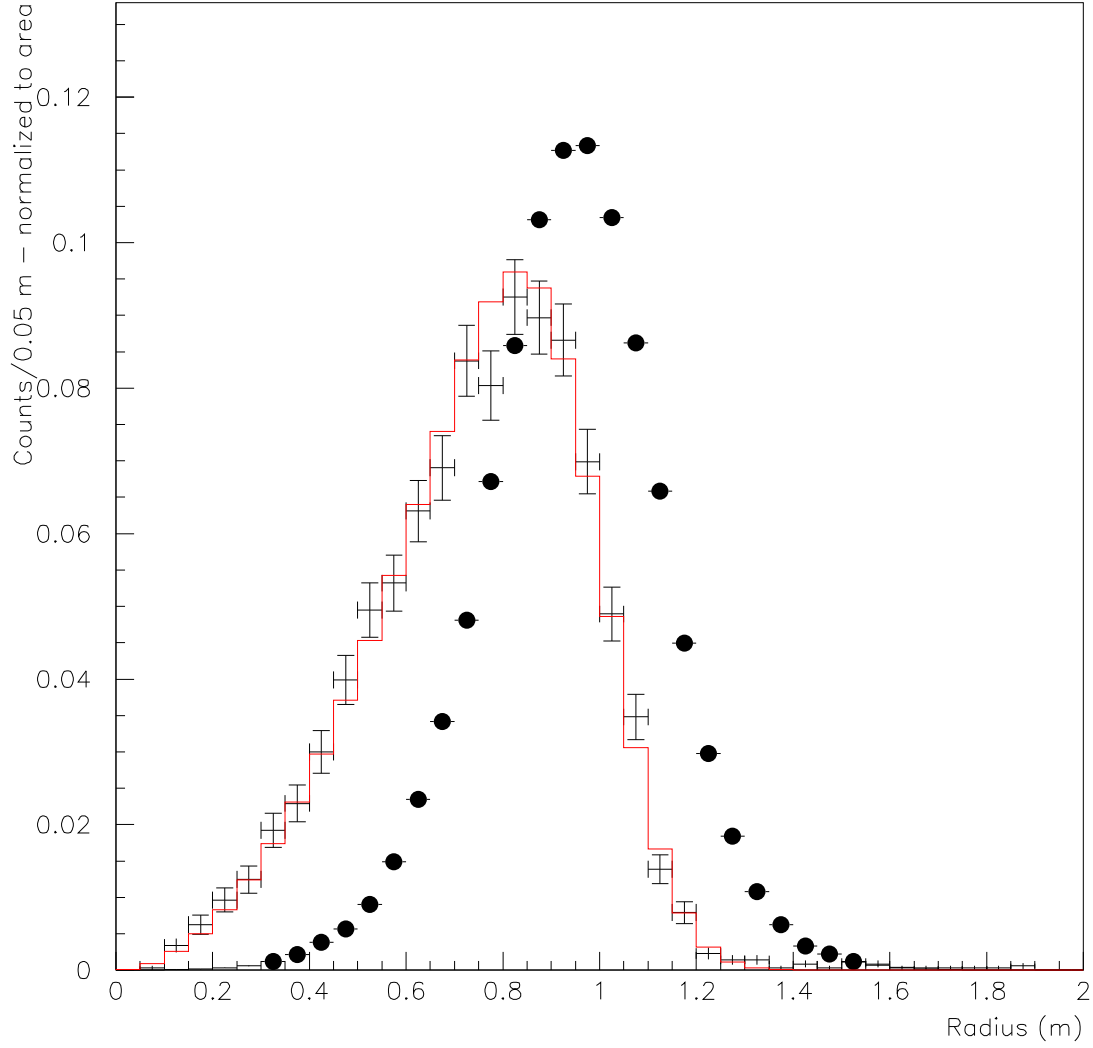


Figure V.7: Radial distributions of internal and external contaminations.

The distribution of ^{214}Po decays (red crosses) identified by means of the delayed coincidence method in phase Foxtrot is taken as representative of internal background distributions. It is in agreement with the theoretically predicted radial distribution (histogram).

The distribution of events detected during phase Quebec in the radon-in-water test (black circles), which are due to ^{222}Rn and daughters dissolved in the shielding water, is taken as representative of external background.

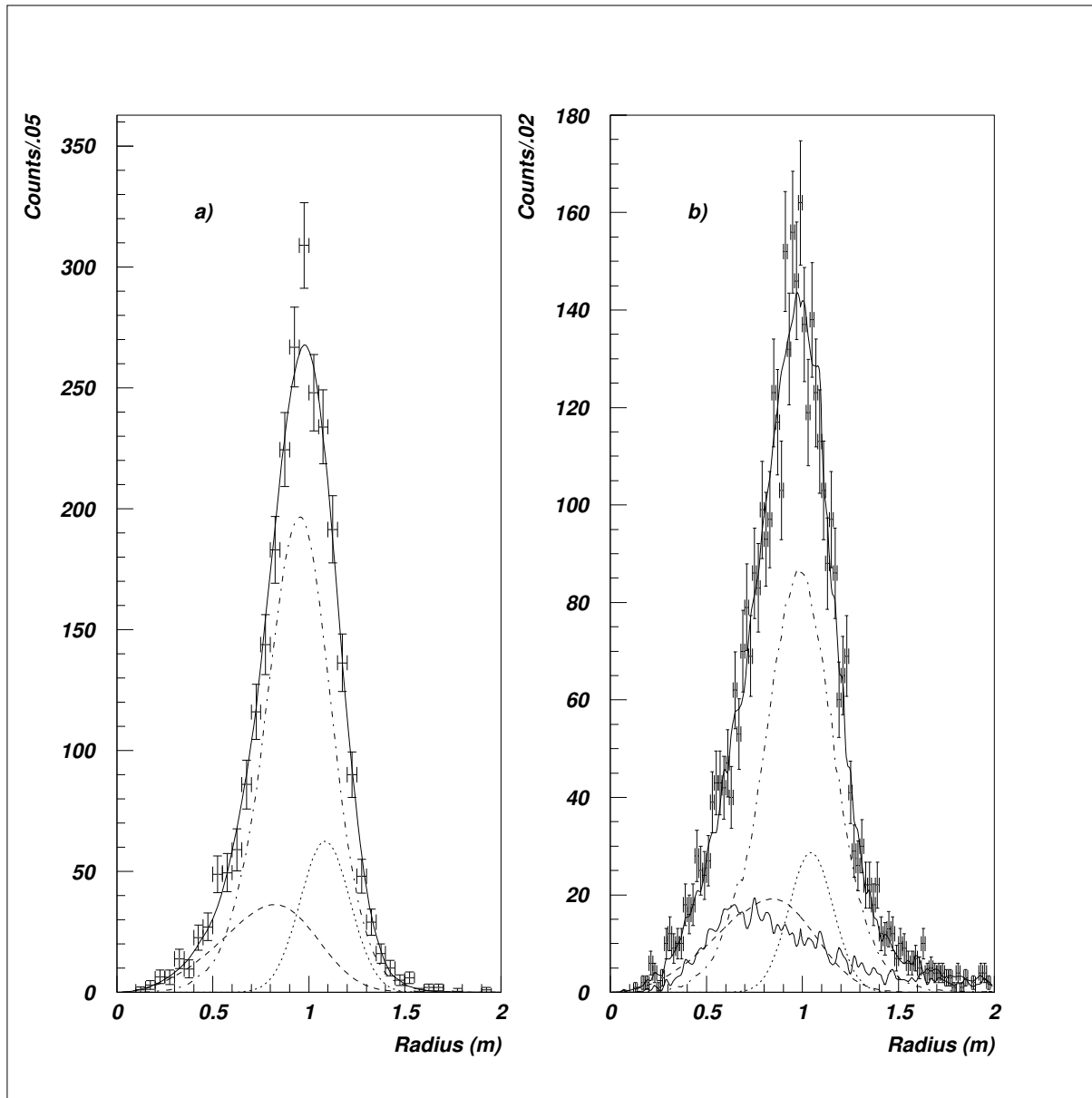


Figure V.8: Phase Foxtrot.

Fit of the radial distribution before any purification.

Plot a) refers to the first method, plot b) refers to the second method.

The crosses are the experimental data, the continuous line is the fit function, the dotted-dashed line is the external background contribution, the dotted line is the surface contribution and the dashed line is the internal contribution. The lower continuous line in plot b) is the muon contribution.

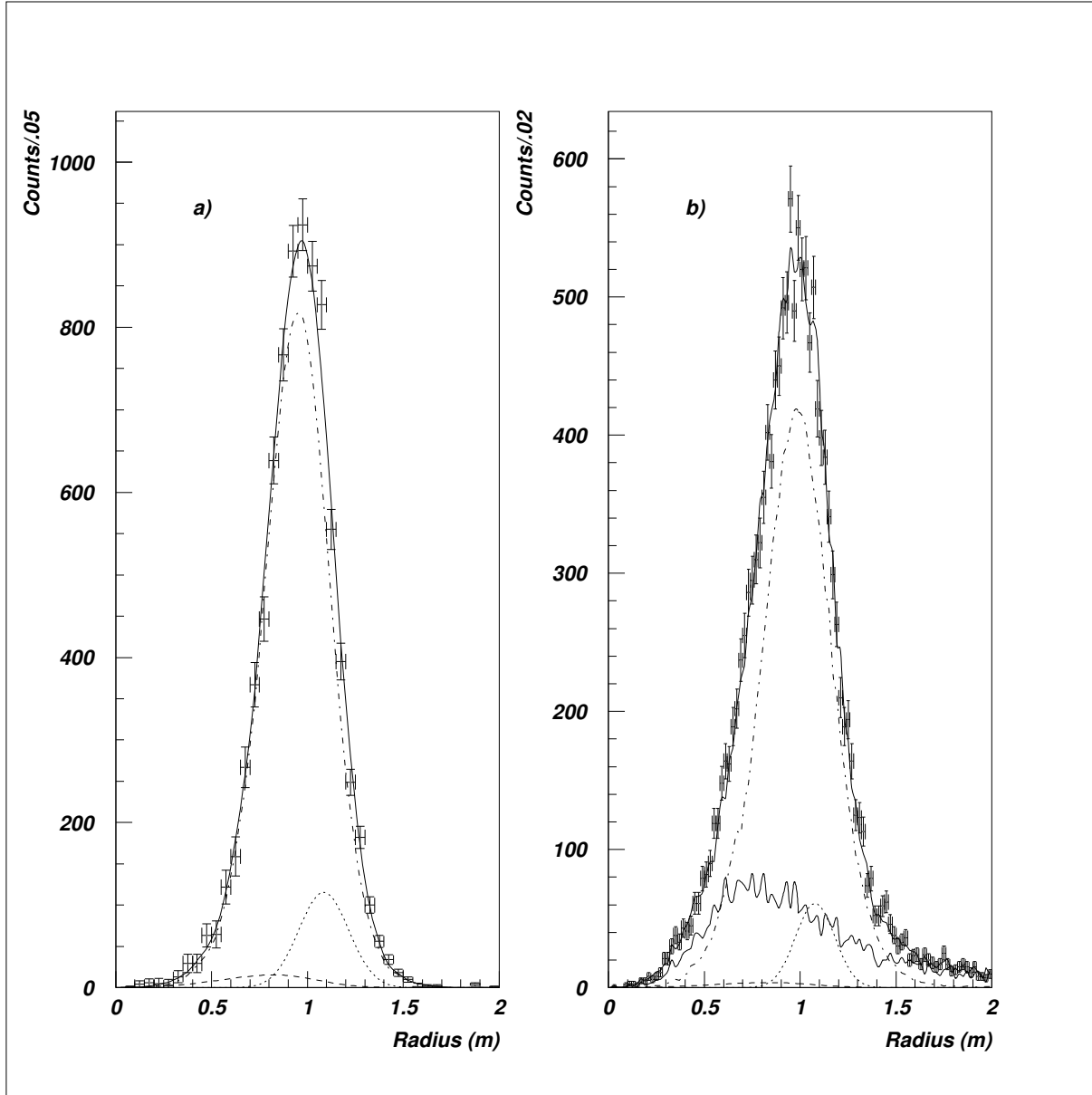


Figure V.9: Phase Oscar.

Fit of the radial distribution before any purification.

Plot a) refers to the first method, plot b) refers to the second method.

The crosses are the experimental data, the continuous line is the fit function, the dotted-dashed line is the external background contribution, the dotted line is the surface contribution and the dashed line is the internal contribution. The lower continuous line in plot b) is the muon contribution.

Before discussing the results we remind that a further source of background is the internal background due to the transient ^{222}Rn which was brought in during the scintillator processing operations. The activity of the transient ^{222}Rn can be evaluated by means of the detected counting rate for mass 214 sequences: it was negligible during phase Foxtrot and it was of (30 ± 7) counts/day during phase Oscar. The activity due to transient ^{222}Rn is internal to the scintillator, but it is not intrinsic of the scintillator. It would have decayed away if it had been possible to extend the length of the data taking in phase Oscar. In order to quote the intrinsic contamination during phase Oscar the contamination from transient ^{222}Rn will be subtracted from the total internal activity.

The results of the fits quoted in table V.1 show that:

- the activity of the external background before and after the purification goes from (1700 ± 270) counts/day to (2050 ± 100) counts/day and it is constant within the errors.

The activity of the external background corresponds to a ^{222}Rn contamination in the water buffer at the level of 30 mBq/m^3 . This estimate is confirmed also by the results of laboratory measurements with charcoal traps and by the analysis of the energy spectra. Figure V.10 shows the energy spectrum of the sample of events selected by means of the scintillation cuts, in the energy region above the lower limit of the neutrino window. The spectrum is well fitted by a function obtained by assuming as the only background source a ^{222}Rn contamination at the level of 30 mBq/m^3 in the water buffer surrounding the inner vessel.

The external background is dominating the total counting rate in the neutrino window during both phase Foxtrot and Oscar;

- a surface background due to radioactivity situated on the inner vessel is present. The fits result in very reasonable value both for the σ (as compared with the expected spatial resolution) and for the mean value of the radius (as compared with the inner vessel radius) of the gaussian representing the surface background. The surface background activity is estimated to be (350 ± 190) counts/day before the purification and (170 ± 60) counts/day after it. These two numbers should be consistent within the errors;
- the activity of the internal background goes from (470 ± 90) counts/day before the purification to (21 ± 47) counts/day after the purification. The best estimate of the internal intrinsic activity after the purification is obtained by subtracting the activity due to the transient ^{222}Rn and it is (-9 ± 48) counts/day.

A preliminary estimate of the possible systematic effects due to the uncertainties in modeling the surface distribution and in parametrizing the muon Čerenkov events can be accounted for about 30 counts/day in the evaluation of the internal background.

The results on the internal contamination of the radial study are confirmed by the analysis of the energy spectra. By comparing the energy spectra before and after the purification we obtain in the neutrino window an excess of (600 ± 100) counts/day in phase Foxtrot with respect to phase Oscar (see figure V.11), which is in agreement with the reduction of the internal backgrounds between the two phases resulting from the radial analysis.

Figure V.11 shows also that a peak centered around 400 KeV is present in the energy spectrum recorded before the scintillator purification. The α/β discrimination showed that the peak is due to an α activity of about 250 counts/day. The most likely origin of this α activity is the ^{222}Rn daughter ^{210}Po that would have been left in the scintillator from the decay of ^{222}Rn contaminating the inner vessel or the scintillator. The presence of ^{210}Po invokes also the activity of the father ^{210}Bi at the level of 170 counts/day in the neutrino window (or more if the ^{210}Po activity is not already at the equilibrium with the ^{210}Bi activity).

^{210}Po and ^{210}Bi are the expected major contributors to the internal background recorded in phase Foxtrot together with ^{85}Kr . The activity of ^{85}Kr in the neutrino window during phase Foxtrot has been measured by means of the delayed coincidence method and is of about 150 counts/day.

We conclude that the internal background which was present before purification and subsequently removed by the purification plants, was probably due to contaminants (^{210}Bi , ^{210}Po and ^{85}Kr) introduced into the scintillator either during its handling, transport and change of vessels, or by the contact of the scintillator and of the inner vessel with air. The level of activity of ^{210}Po recorded in phase Foxtrot invokes a former ^{222}Rn contamination of about 2 Bq that might have been produced either during the inner vessel construction in a non radon-free environment or during a long contact of scintillator with air.

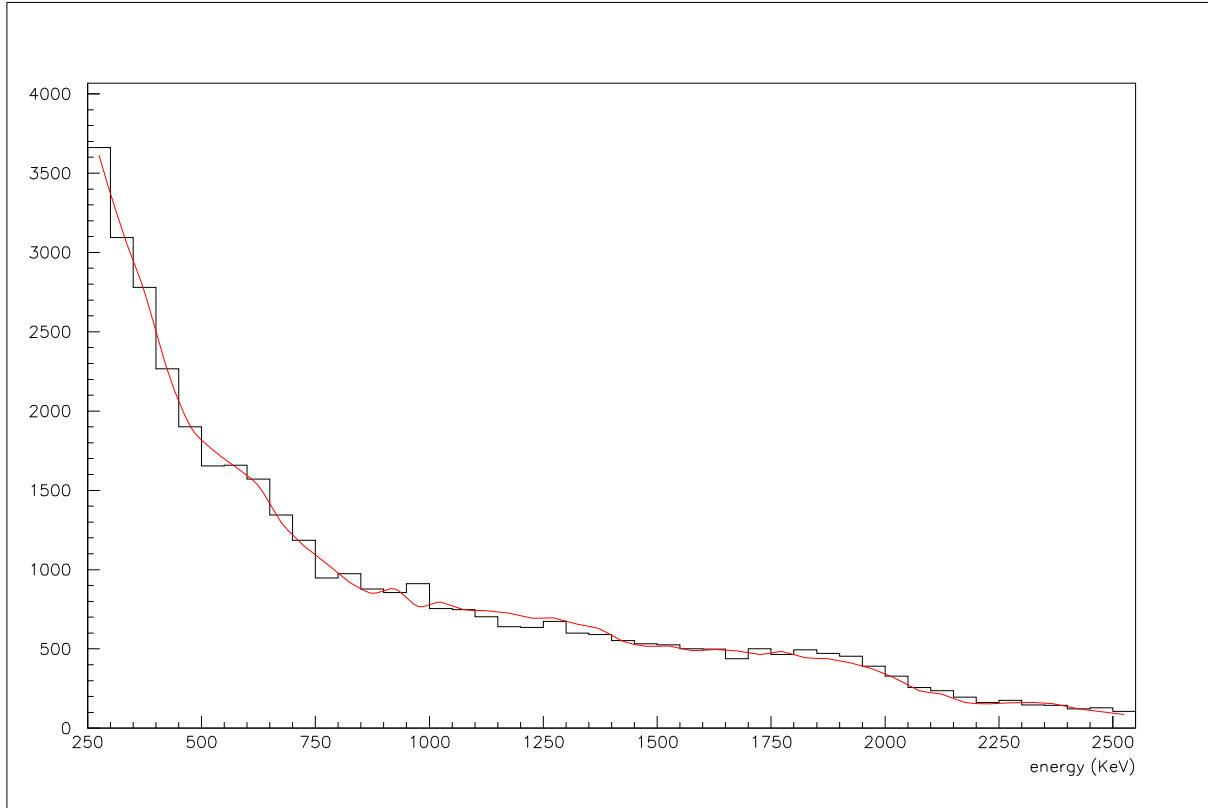


Figure V.10: Phase Oscar.

Energy spectrum of the sample of events selected by means of the scintillation cuts, in the energy region above the lower limit of the neutrino window.

The spectrum is well fitted by a function obtained by assuming as the only background source a ^{222}Rn contamination at the level of 30 mBq/m^3 in the water buffer surrounding the inner vessel.

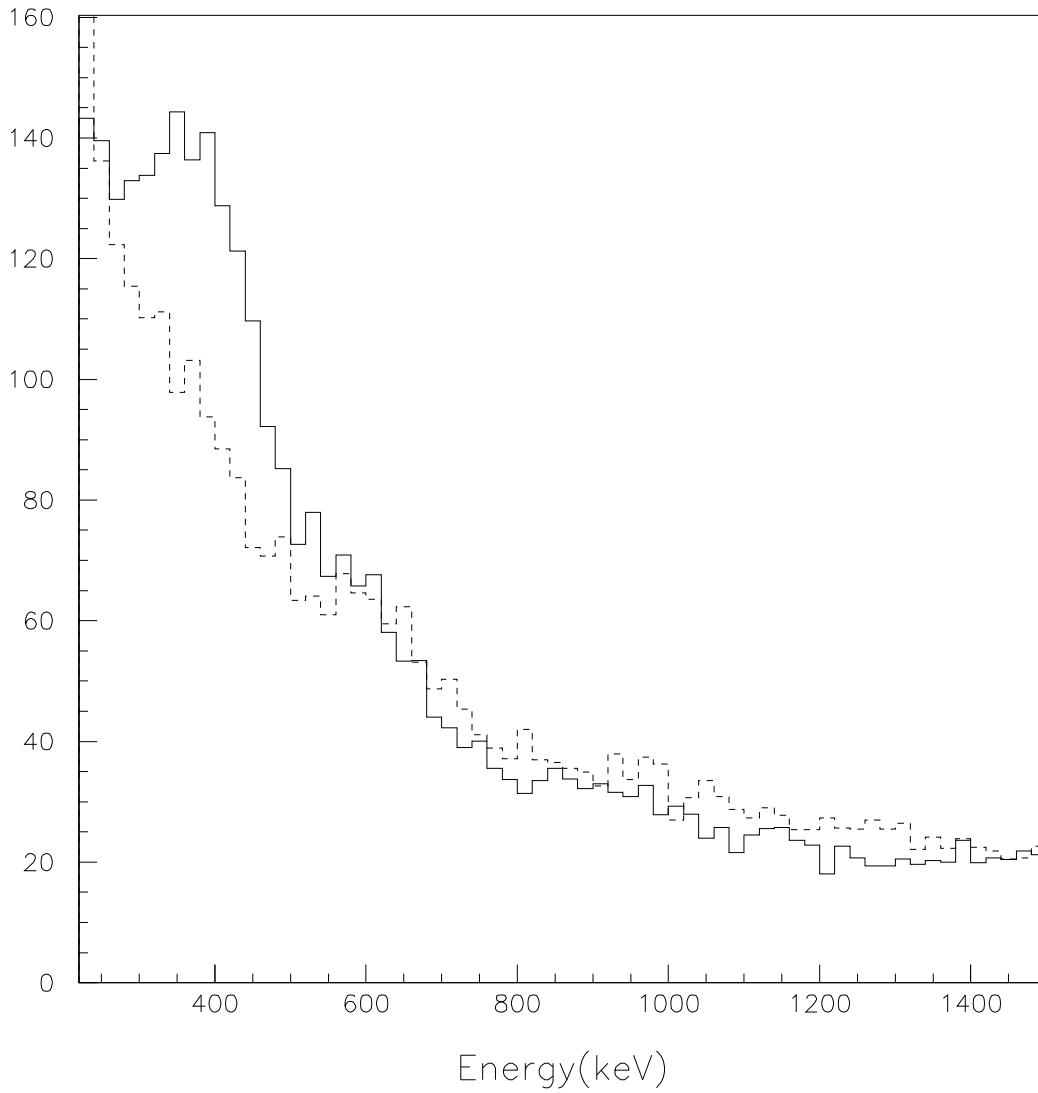


Figure V.11: Energy spectra in CTF before and after the scintillator purification.
The dotted line is the energy spectrum in phase Foxtrot, before any purification.
The continuous line is the energy spectrum in phase Oscar, after the scintillator purification.

Chapter VI

Conclusions

The CTF is an important facility to study the design of experiments based on large mass of liquid scintillator and requiring very low background. It is also an important tool to test purification methods of several materials like liquid scintillator solvents, scintillation fluors and water.

The CTF was operating in LNGS since December 1994 up to July 1997. It is a liquid scintillator based detector, whose active mass of 4.5 tons is shielded by about 4.5 m of ultrapure water and is observed by 100 PMTs. The detector is equipped with two electronic chains to measure delayed coincidences at delay times as low as 100 ns.

The sensitivity of the detector reached levels unobtainable by classic methods of measurement. Limits of 10^{-18} ($^{14}\text{C}/^{12}\text{C}$) and few times 10^{-16} g/g (^{238}U , ^{232}Th) were obtained for specific contaminants. The sensitivity of CTF for the total counting rate in the neutrino window amounts to about 10 counts/day/ton which is equivalent to 20 times the interaction rate of ^7Be neutrinos at the SSM predicted flux.

The CTF cannot establish the feasibility of BX because the detector scale does not allow to study the total counting rate at the level of the ^7Be neutrinos interaction rate. The rate of the target signal corresponds to an intrinsic contamination of the scintillator which is already extremely low and is equivalent to a radiopurity level of 10^{-16} g/g in the natural radioactive chains. In order to reduce the external background below the above value for the internal background, it is necessary to define a fiducial mass of scintillator surrounded by an “active buffer” as the ultimate shield: to say a thick enough mass of the same liquid scintillator already at the radiopurity level of 10^{-16} g/g in ^{238}U and ^{232}Th . On the other hand, as far as the detector geometry is concerned, the CTF scintillator volume can be compared to the BX crust: the distance between the water buffer and the innermost scintillator of 1 m and the ^{222}Rn contamination in the buffer at the level of 30 mBq/m³ do not allow to define a fiducial volume. Therefore in CTF the sensitivity to the total counting rate is limited by external background owing to the limited scale of the detector.

The final answer to the feasibility of BX can be given only by BX itself. However CTF could perform several “kill the background or die” tests. The research of the candidate consisted in the analysis of these tests, whose results are summarized in the following paragraphs.

The results of all the “kill or die” tests were negative: impediments to the feasibility of BX were not noticed in CTF. On the basis of these results, it was decided to build the BX detector in order to measure the flux of the solar ^7Be neutrinos.

VI-A ^{14}C contamination

Organic liquid scintillators are predominantly composed by carbon, and the intrinsic contamination in ^{14}C (it decays emitting a β particles with maximum kinetic energy of 156 KeV) can constitute the main source of background at low energies. In fact, the software energy threshold for neutrino observation in BX is fixed at 250 KeV owing to the ^{14}C signal.

The sensitivity of CTF to ^{14}C contamination expressed in terms of the $^{14}\text{C}/^{12}\text{C}$ ratio is of about 10^{-19} .

In CTF the $^{14}\text{C}/^{12}\text{C}$ ratio has been measured at the lowest level ever reached:

$$(1.94 \pm 0.01_{\text{stat}} \pm 0.09_{\text{syst}}) \times 10^{-18} \quad (\text{VI.1})$$

at this level of contamination the expected counting rate from ^{14}C in the neutrino window amounts to 0.2 counts/day and is negligible.

Indeed CTF has shown that the ^{14}C contamination is not a worry for BX.

VI-B Natural radioactive chains contamination

In BX the ultimate source of background is expected to be internal background, which may consist of cosmogenic radioactivity, artificial and natural radioactivity.

The cosmogenic radioactivity is estimated to be negligible on the basis of the discussion in section II-C.3

The artificial radioactivity is mainly due to gaseous fall-out products, that are discussed in the forthcoming section VI-C.

The natural radioactivity is due to the very long living carriers ($10^9 \text{ y} < \tau$): ^{232}Th , ^{238}U and ^{40}K . The most worrying sources are ^{232}Th and ^{238}U because they are the fathers of the natural radioactive chains: for each decay of the fathers, several (up to ten) decays of the daughter nuclides are expected at the secular equilibrium. However an organic liquid scintillator is likely to have very low levels of natural radioactivity, because the long living carriers typically exist as ions and are hence insoluble in non-polar organic solvents. Moreover, if they are present in form of non-organic complexes, it may be possible to purify them.

The sensitivity of CTF to ^{232}Th contaminations probed by the rate of mass 212 sequences is ultimately limited by statistics. Nevertheless, owing to the presence of the daughter mass 214 sequence, the transient ^{222}Rn contaminations brought in by the scintillator processing operations may constitute a relevant source of background if the data taking is not long enough to let the ^{222}Rn decay.

The following contaminations were determined for ^{232}Th :

- $4.4_{-1.2}^{+1.5} \times 10^{-16} \text{ g/g}$ in phase Foxtrot, before the scintillator purification
- $< 4.1 \times 10^{-16} \text{ g/g}$ at 90 % C.L. in phase Lima, after the scintillator water extraction
- $8.0_{-2.1-0.8}^{+2.6+0.0} \times 10^{-16} \text{ g/g}$ in phase Oscar, after the scintillator distillation

the three measurements are compatible with the assumption of a constant contamination at the 25 % C.L.. However the present data cannot rule out a reduction of the contamination due to the scintillator water extraction. Likewise, an increase of the contamination due to the scintillator distillation cannot be ruled out.

The CTF has shown that the scintillator coming from the factory has already a ^{232}Th contamination level of a few 10^{-16} g/g . The results was confirmed also by the independent measurement performed by means of the NAA technique (see section V-G) that provided an upper limit of $2 \times 10^{-15} \text{ g/g}$ by probing directly the ^{232}Th content. On the other hand the effectiveness of the purification processes on ^{232}Th removal are not unambiguously determined and it is urged a new test of the processes in the second phase of CTF (CTF II) that will start in 1999.

The sensitivity of CTF to the ^{238}U contamination probed by the mass 214 sequences is limited by the ^{222}Rn background. ^{222}Rn density in the nylon and in the water buffer is much higher than in the scintillator because the ^{238}U and ^{226}Ra contaminations in nylon, water and in the construction materials are orders of magnitude higher than the corresponding values in the scintillator. ^{222}Rn emanates from the nylon into the scintillator and permeates from the water through the nylon into the scintillator. Emanation and permeation are favoured by the changes in the mechanical characteristics of nylon provoked by a long term immersion in water. The diffusion coefficient for Rn in wet nylon after one year of immersion in water, was measured directly in CTF and it is a factor 100 bigger than for dry nylon, whereas the partition coefficient for ^{222}Rn between water and nylon does not change appreciably. The cumulative background from emanation and permeation one year after the start of CTF was of about 10^{-15} g/g .

The only measurement of the ^{238}U intrinsic contamination was performed six months after the start of CTF. At that time the background from emanation and permeation was not precisely determined but we can guess that it was of a few 10^{-16} g/g . The contamination measured is quoted as an upper limit because the undetermined background due to emanation and permeation must be still subtracted from:

- $< (3.5 \pm 1.3) \times 10^{-16} \text{ g/g}$ in phase Foxtrot, before scintillator purification

the result is very promising in view of BX because it could indicate a very low background from ^{238}U which is the most relevant among the expected sources of internal background (see table II.7).

The study on the background from emanation and permeation added some important constraint to the design of BX and CTF II. The high level of ^{222}Rn in the water buffer, 30 mBq/m^3 , was somewhat unexpected. The target value for the ^{222}Rn background was of 1 mBq/m^3 . The most likely source of ^{222}Rn in water are contaminations in the construction materials (a contribution from ^{226}Ra in water is not likely but is not ruled out). In order to reduce the external background in CTF II a nylon shroud will be installed close to the PMTs as a barrier for Rn coming from the construction materials. The shroud will isolate that portion of the water buffer close to the IV from the remainder of the buffer.

In BX ^{222}Rn coming from the constructing materials can still be a source of external background and therefore also in BX it is foreseen the installation of a Rn nylon barrier close to the PMTs. On the other hand the possible presence of ^{226}Ra in the water is not worrying for BX, since the buffer liquid will be the solvent of the scintillator, Pseudocumene.

As far as ^{40}K is concerned, the best limit comes from NAA measurements and it amounts to an equivalent contamination of 4×10^{-12} g/g for $^{\text{nat}}\text{K}$, while the requirement for BX is 10^{-14} g/g.

VI-C Gaseous fall-out products contamination

The sources of artificial radioactivity that may contribute to the internal background in BX are gaseous fall-out products like the nuclide ^{85}Kr . The radioactive gaseous nuclides may enter the scintillator if it gets in contact with air during the scintillator handling and processing operations.

The CTF can disentangle ^{85}Kr from the other backgrounds by using the sequence which is present in the minor branching ratio for the ^{85}Kr decay (see section IV-D). The CTF sensitivity to ^{85}Kr is ultimately limited by the random background and amounts to 35 events/day for the total ^{85}Kr activity. The following results were achieved for the total ^{85}Kr activity:

- (389 ± 70) counts/day during phase Foxtrot, before scintillator purification
- <50 counts/day at 90 % C.L. during phase Lima, after scintillator water extraction
- <35 counts/day at 90 % C.L. during phase Oscar, after scintillator distillation

no evidence for ^{85}Kr contamination was observed after the scintillator purification: the best estimates for the ^{85}Kr activity in phases Lima and Oscar is zero, and the results of the measurements are quoted as upper limits.

^{85}Kr is removed very efficiently by scintillator water extraction: the purification factor exceeds 10. Therefore the CTF showed that ^{85}Kr is not a worry for BX.

VI-D Total counting rate

A detailed study of the total counting rate in the neutrino window was performed.

The marked difference between the radial distributions of the external and internal background allowed to disentangle the two contributions to the total counting rate by means of a fit on the radial distribution of the events detected (see section V-G). The ultimate resolution on the internal contribution to the total counting rate was of 50 counts/day in the 4.5 tons of scintillator, to say about 20 times the ^7Be neutrinos interaction rate. The following results were obtained for the total counting rate in the neutrino window due to internal contamination:

- (470 ± 90) counts/day at 90 % C.L. during phase Foxtrot, before scintillator purification
- (-9 ± 48) counts/day at 90 % C.L. during phase Oscar, after scintillator purification

During phase Foxtrot, before the scintillator purification, a relevant source of background due to internal contaminations was present. The total activity due to internal contamination was measured at the level of (470 ± 90) counts/day by the radial analysis and at the level of (600 ± 100) counts/day by the spectral analysis. Part of the activity is due to ^{85}Kr (150 counts/day), tagged by the coincidence method. Another part is likely due to ^{210}Po (250 counts/day) which is identified by spectral analysis and α/β discrimination (see section V-G) and to its father ^{210}Bi (170 counts/day or more).

The internal background which was present before purification was probably due to contaminants introduced into the scintillator either during its handling, transport and change of vessels, or by contact of the scintillator and of the inner vessel with air. The internal background sources were successfully removed by the scintillator purification. The background remaining after the purification is compatible with zero within the experimental uncertainty.

Bibliography

- [A⁺89] M. Aglietta et al., *Nuovo Cim. C* **12**, 467 (1989).
- [A⁺98a] G. Alimonti et al., *Astropart. Phys.* **8**, 141 (1998).
- [A⁺98b] G. Alimonti et al., *Nucl. Instrum. Methods A* **406**, 411 (1998).
- [A⁺98c] G. Alimonti et al., *Phys. Lett. B* **422**, 349 (1998).
- [B⁺89] P. Belli et al., *Nuovo Cim. A* **101**, 959 (1989).
- [B⁺93] S. Bonetti et al., *Nucl. Instrum. Methods A* **329**, 314 (1993).
- [B⁺96] M. Balata et al., *Nucl. Instrum. Methods A* **370**, 605 (1996).
- [Bah89] J. Bahcall, *Neutrino Astrophysics*, Cambridge University Press, 1989.
- [BBP98] J. Bahcall, S. Basu, and M. Pinsonneault, *Phys. Lett. B* **433**, 1 (1998).
- [BC⁺93] J. Benziger et al., editors, *N.S.F. Borexino Proposal*, Princeton University, 1993.
- [BC⁺96] J. Benziger et al., editors, *A Proposal for Participation in the Borexino Solar Neutrino Experiment*, Princeton University, 1996.
- [Bir74] J. Birks, *The theory and practice of scintillation counting*, Pergamon Press, 1974.
- [BKS98] J. Bahcall, P. Krastev, and A. Smirnov, hep-ph/9807216 (1998).
- [Bor95] Borexino Collaboration, editor, *Memo on: Borexino Project*, Univ. degli Studi di Milano, 1995.
- [Bor96] Borexino Collaboration, editor, *Addendum to the Borexino Proposals*, Univ. degli Studi di Milano, 1996.
- [Bor97] Borexino Collaboration, editor, *Borexino Design Specification Document*, Univ. degli Studi di Milano, 1997.
- [BR⁺92] G. Bellini et al., editors, *I.N.F.N. Borexino Proposal*, volume 1–2, Univ. degli Studi di Milano, 1992.
- [BV87] F. Boehm and P. Vogel, *Physics of massive neutrinos*, Cambridge University Press, 1987.
- [CDD⁺98] B. Cleveland et al., *Astrophys. J.* **496**, 505 (1998).
- [CFFL95] E. Calabresu, N. Ferrari, G. Fiorentini, and M. Lissia, *Astropart. Phys.* **4**, 159 (1995).
- [Deu96] M. Deutsch, editor, *Proposal for a Cosmic Ray Detection System for the Borexino Solar Neutrino Experiment*, Massachusetts Institute of Technology, 1996.
- [F⁺98] Y. Fukuda et al., *Phys. Rev. Lett.* **81**, 4279 (1998).
- [Fer49] E. Fermi, *Nuclear Physics*, the University of Chicago Press, 1949.
- [FLM97] G. Fogli, E. Lisi, and D. Montanino, *Phys. Rev. D* **56**, 4374 (1997).
- [G⁺97] T. Goldbrunner et al., *J. Rad. Nucl. Chem.* **216**, 293 (1997).
- [G⁺98] T. Goldbrunner et al., *Nucl. phys. B (Proc. Suppl.)* **61**, 176 (1998).

- [GcH⁺96] W. GALLEX collaboration: Hampel et al., Phys. Lett. B **388**, 364 (1996).
- [GMB⁺] S. GONG + MDI: Basu et al., astro-ph/9712733 .
- [GTC⁺97] S. GOLF: Turck Chieze et al., Solar Phys. **175**, 247 (1997).
- [HBL94] N. Hata, S. Bludman, and P. Langacker, Phys. Rev. D **49**, 3622 (1994).
- [KcF⁺96] Y. KamiokaNDE collaboration: Fukuda et al., Phys. Rev. Lett. **77**, 1683 (1996).
- [Kno79] G. Knoll, *Radiation and detection measurement*, J. Wiley and sons, 1979.
- [L⁺83] P. Langacker et al., Phys. Rev. D **27**, 1228 (1983).
- [Lau93] M. Laubenstein, *Proceedings of the seventh Pisa meeting on advanced detectors, La Biodola, Isola d'Elba, Italy*, Elsevier Science, 1993.
- [LBB⁺97] S. LOWL1 + BISON: Basu et al., Mon. Not. R. Astron. Soc. **292**, 234 (1997).
- [Man97] I. Manno, Pulse shape discrimination in borexino, Technical report, BX coll. internal report, 1997.
- [MS85] S. Mikeyev and A. Smirnov, Yad. Fiz. **42**, 1441 (1985).
- [Nef96] M. Neff, 1996, internal note on the laboratory measurements of quenching factors.
- [Pau30] W. Pauli, 1930, Letter to the Physical Society of Tubingen.
- [RC53] F. Reines and C. Cowan, Phys. Rev. **90**, 492 (1953).
- [RGL98] G. Ranucci, A. Goretti, and P. Lombardi, Nucl. Instrum. Methods A **412**, 374 (1998).
- [ScG⁺98] V. SAGE collaboration: Gavrin et al., (1998).
- [tH71] G. 't Hooft, Phys. Lett. B **37**, 195 (1971).
- [V⁺96] R. Vogelaar et al., Nucl. Instrum. Methods A **372**, 59 (1996).
- [vF⁺98] F. von Feilitzsch et al., The borexino muon identification system, Technical report, TU-Muenchen Muon and NA54 group report, 1998.
- [W⁺91] M. Wojcik et al., Nucl. Instrum. Methods B **61**, 8 (1991).
- [Woj97] M. Wojcik, 1997, private communication.
- [Wol78] L. Wolfenstein, Phys. Rev. D **17**, 2369 (1978).
- [WW89] R. Winston and W. Welford, *High collection nonimaging optics*, page 132, Academic Press, New York, 1989.